

BEN-GURION UNIVERSITY OF THE NEGEV
THE FACULTY OF NATURAL SCIENCES
DEPARTMENT OF GEOLOGICAL AND ENVIRONMENTAL SCIENCES

**The Effects of Normal Stress on the Roughness Evolution of Experimental
Faults through Shear**

Thesis Submitted in Partial Fulfillment of the Requirements for the M.Sc. Degree

by

Nir Badt

Under the Supervision of Prof. Yossef Hodara Hatzor & Dr. Amir Sagy

February 2015

BEN-GURION UNIVERSITY OF THE NEGEV
THE FACULTY OF NATURAL SCIENCES
DEPARTMENT OF GEOLOGICAL AND ENVIRONMENTAL SCIENCES

The Effects of Normal Stress on the Roughness Evolution of Experimental Faults through Shear


Thesis Submitted in Partial Fulfillment of the Requirements for the M.Sc. Degree

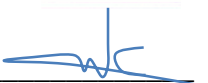
by

Nir Badt

Under the Supervision of Prof. Yossef Hodara Hatzor & Dr. Amir Sagy

Signature of student: _____ Date: _____

Signature of supervisor:  _____ Date: _____

Signature of supervisor:  _____ Date: _____

Signature of chairperson of the committee for graduate studies: _____ Date: _____

February 2015

Abstract

The topography of fault surfaces plays an integral role in the dynamics of earthquakes. The roughness profile of slip-surfaces relates strongly to the stress distribution across fault planes, their shear resistance and the critical slip distance.

The evolution of fault surface roughness was studied here in direct shear laboratory experiments. Mating surfaces, produced by tensile fractures induced in prismatic limestone beams by means of the four-point bending methodology, were sheared under imposed normal stresses of 5 to 15 MPa where at each test constant normal stress was maintained to a preset displacement distance of 10 mm under a constant displacement rate of 0.05 mm/s using a hydraulic closed-loop servo controlled system. Experimental results displayed slip hardening behavior of the rough surfaces before ultimate shear resistance has been attained. The surfaces also experienced dilation during the initial stages of slip which was then typically followed by contraction. The dilation-contraction behavior of the sliding interfaces suggested that two mechanisms for asperity interactions were dominant during slip, riding-up and interlocking. The latter mechanism was attributed to the peak friction, calculated during the experiments, and subsequently, to the failure of the asperities. The calculated peak friction for each experiment revealed that peak friction did not coincide with maximum imposed normal stress. In fact, the peak and residual friction results showed variability and did not scale with normal stress for every experiment. It is argued here that the variability in the peak and residual friction results with normal stress are more related to the surface roughness.

The roughness evolution was measured and analyzed using optical profilometer scans of the surface geometry before and after slip using power spectral density (PSD) and root mean square (RMS) methods. The roughness results indicated that the surface roughness increased with normal stress through shear displacement when the normal stress levels were greater than 5 MPa, in contrast to results obtained by *Davidenko et al. (2014)* when testing the same kind of interfaces but under a constant normal stress of 2 MPa only. This difference of results between this study and the *Davidenko et al. (2014)* study was attributed to the higher values of normal stresses tested in this study. Most of the damage sustained by the rock surfaces was localized in damage zones. Through examination of the damage and wear products it was concluded that the increase in roughness was due to penetrative damage to the host rock, which included fracturing and asperity plucking.

Roughness evolution is correlated here with the stress-drop measured during shear displacement as both reflect the release of the stored elastic energy during the transition from peak shear stress to residual shear stress. The damage sustained by the rock exceeded the scale of the roughness itself, breaking partially or completely the asperities that made up the original surface topography. Instead of decapitating

the asperities, as often suggested in past studies, the strain energy accumulated during the initial stages of slip was channeled to break the asperities and create new surfaces in different orientations from the mean sliding plane. An analytical model was further used to support the observed damage in the experiments. Model results suggested that the roughness of the sliding interface affects the near-interface stress field, which includes stress concentrations, amplifications of the principal stress difference and deviation of the near-field stress trajectories from the far-field stress orientation. It is also implied that the maximum resistance to shear is strongly dependent upon the near-fault stress field as further reflected by the correlation between its value and wear volume accumulation.

The geometrical analysis also revealed that the experimental faults did not exhibit self-affine, fractal pattern. The deviation from fractal geometry was attributed to the size of the grains that make up the limestone surfaces. PSD results suggest that the PSD-wavelength curves deviate from self-affine behavior around wavelengths corresponding with the mean grain diameter of the tested limestone material. However, the post-shear surfaces did exhibit self-affine, fractal geometry with a Hurst exponent value of ~ 0.8 , parallel to slip direction. The change in geometry was related to the roughness evolution of the experimental faults. The damage sustained by the host rock during shear affected roughness in different scales including that of the grains themselves. Thus, by breaking the asperities, the post-shear surfaces evolved to fractal geometry through shear.

As in natural faults, the experimental faults studied here all developed a damage zones. Furthermore, the roughness of the experimental faults resembled natural faults in a sense that the amplitude to wavelength (or the topography) exceeded or was of equal magnitude to the amount of slip for a single event. Therefore, the study of the effects of stress and roughness in experimental faults is a valid and important basis for the study of the mechanical evolution of natural faults. The implications of this study suggest that roughness is significant not only in terms of resistance to shear, but also to the stress distribution across faults and the development of damage zones around them.

Acknowledgments

I was privileged to work and study under the guidance of Professor Yossef Hodara Hatzor. His teaching, knowledge and support helped me develop both professionally and personally, from my first steps of my academic education and throughout this research.

I would like to express my sincere gratitude to Dr. Amir Sagy. His continuous motivation, knowledge and advice helped me throughout this study by pushing me further and further, opening my mind to new horizons and helping me grow and develop.

Besides my advisors, I would like to thank Professor Jay Fineberg and Dr. Liran Goren for reviewing my thesis and for their insightful remarks.

I would like to thank Mr. David Koseshvilli for the help in the preparation of the rock samples for this study and Mrs. Ester Shani for all the logistic help. I would also like to thank Dr. Vyacheslav Palchik for the help in retrieving data of past research. A special thanks goes to Mrs. Rivka Eyni and Mrs. Zahala Sharabi for their commitment in helping with any administrative problem, at any time.

I thank my friends and fellow graduate students: Omri Shitrit, Ravit Zelig, Maayan Shviro, Guy Tzur and Neta Ginsburg for the support and fruitful discussions.

I thank my parents and my sisters for their support and love from the beginning.

Finally, I thank my wife Tal for her understanding, care, support and encouragement throughout the years.

Table of Contents

1	Introduction.....	13
1.1	Faults and Fractures in Rock	13
1.2	Frictional Sliding of Rock Surfaces.....	13
1.3	Research Goals	14
2	Scientific Background.....	16
2.1	Surface Roughness.....	16
2.2	Roughness of Natural Fault Surfaces	17
2.3	Frictional Sliding of Surfaces and Wear Processes	20
2.4	Effects of Normal Stress on Frictional Sliding of Joints and Faults.....	22
2.5	Roughness Evolution of Fault Surfaces.....	25
3	Methods.....	26
3.1	Creation of Initial Experimental Fault Surface.....	26
3.2	Direct Shear Experiments	27
3.3	Surface Geometry Measurements.....	32
3.4	Data Analysis.....	35
3.5	Mechanical properties of the tested limestone.....	41
4	Results.....	42
4.1	Direct Shear Tests.....	42
4.2	Roughness evolution results	51
4.3	Wear Analysis.....	77
5	Analysis of Experimental Results	79
5.1	Mechanical Interactions.....	79
5.2	Analytical Model	83
6	Discussion	92
6.1	Statistical Self-Affinity of Experimental Fault Surfaces	92
6.2	The Relationship between Stress, Friction, Roughness and Wear	93
6.3	Relations between the Experimental Results and Field Observations.....	97

7	Conclusions.....	99
8	References.....	101
9	Appendix I.....	108
9.1	Experiment LN1 ($\sigma_n=5$ MPa).....	108
9.2	Experiment LN10 ($\sigma_n=7.5$ MPa).....	109
9.3	Experiment LN6 ($\sigma_n=10$ MPa).....	110
9.4	Experiment LN11 ($\sigma_n=12.5$ MPa).....	111
9.5	Experiment LN5 ($\sigma_n=15$ MPa).....	112
9.6	Experiment LN7 ($\sigma_n=15$ MPa).....	113
10	Appendix II.....	114
10.1	Model Results for Run B ($\sigma_n=7.5$ MPa).....	114
10.2	Model Results for Run C ($\sigma_n=10$ MPa).....	115
10.3	Model Results for Run E ($\sigma_n=15$ MPa).....	116
10.4	Model Results for Run F ($\sigma_n=15$ MPa).....	117
10.5	Reference Model.....	118

List of Figures

Figure 2.1	17
Figure 2.2	17
Figure 2.3	19
Figure 2.4	21
Figure 2.5	22
Figure 2.6	23
Figure 3.1	27
Figure 3.2	28
Figure 3.3	29
Figure 3.4	32
Figure 3.5	33
Figure 3.6	34
Figure 3.7	36
Figure 3.8	36
Figure 3.9	38
Figure 3.10	38
Figure 3.11	39
Figure 3.12	40
Figure 3.13	41
Figure 4.1	43
Figure 4.2	44
Figure 4.3	44
Figure 4.4	45
Figure 4.5	45
Figure 4.6	46
Figure 4.7	47
Figure 4.8	48
Figure 4.9	49
Figure 4.10	49
Figure 4.11	51
Figure 4.12	53
Figure 4.13	54
Figure 4.14	56

Figure 4.15	56
Figure 4.16	57
Figure 4.17	58
Figure 4.18	59
Figure 4.19	60
Figure 4.20	60
Figure 4.21	61
Figure 4.22	61
Figure 4.23	62
Figure 4.24	64
Figure 4.25	64
Figure 4.26	65
Figure 4.27	65
Figure 4.28	66
Figure 4.29	66
Figure 4.30	67
Figure 4.31	68
Figure 4.32	68
Figure 4.33	69
Figure 4.34	70
Figure 4.35	71
Figure 4.36	71
Figure 4.37	72
Figure 4.38	72
Figure 4.39	73
Figure 4.40	74
Figure 4.41	75
Figure 4.42	76
Figure 4.43	78
Figure 4.44	78
Figure 5.1	80
Figure 5.2	81
Figure 5.3	82
Figure 5.4	84
Figure 5.5	85

Figure 5.6	87
Figure 5.7	87
Figure 5.8.	88
Figure 5.9	88
Figure 5.10	91
Figure 6.1	93
Figure 6.2.	94
Figure 6.3.	98
Figure 9.1	108
Figure 9.2.	109
Figure 9.3.	110
Figure 9.4	111
Figure 9.5.	112
Figure 9.6	113
Figure 10.1	114
Figure 10.2	114
Figure 10.3	115
Figure 10.4	115
Figure 10.5	116
Figure 10.6	116
Figure 10.7	117
Figure 10.8	117
Figure 10.9	118

1 Introduction

1.1 Faults and Fractures in Rock

Geological faults and fractures are natural occurrences in rocks of the upper crust. These phenomena divide the rock mass into a discontinuous medium that affects its mechanical and hydraulic behavior, heat transfer capabilities, strength and other physical attributes. The mechanics of the rock discontinuities are of particular interest in the fields of geological and civil engineering, geophysics and reservoir engineering. In civil engineering, the rock discontinuities play a major role in rock mass stability problems like rock slope stability, mining excavations and support, hydraulic fracturing, earthquake stability and structural foundations. Fault friction and mechanics is at the heart of the study of earthquakes in the field of geophysics, as most earthquakes are a direct result of slip on existing discontinuities (*Brace & Byerlee, 1966; Stein & Wysession, 2003*). Moreover, discontinuities in the rock mass are also important aspects in reservoir engineering and hydrocarbon production. Fractures and faults are important in both sealing and draining reservoir rocks, rock mass strength and heat transfer capabilities (*Haneberg et al., 1999*).

1.2 Frictional Sliding of Rock Surfaces

Friction and contact mechanics have long been of interest to science. Leonardo da Vinci conducted one of the earliest studies of friction during the Renaissance; his work was later lost only to be rediscovered by Guillaume Amontons in 1699 when he published his three laws of friction, which were later verified by *Coulomb (1781)*. It was not until the mid-twentieth century that a more modern approach was introduced when *Bowden & Tabor (1950)* published their theory of adhesion. Their theory concluded that surfaces of any material are rough to a certain extent. Leading to the understanding that the surfaces contact each other through the geometric irregularities, known also as asperities, and hence the real area of contact between the surfaces is much smaller than the nominal area of each surface (*Bowden & Tabor, 1950; Archard, 1953*). Further research in metals further demonstrated that wear production, surface roughness, sliding distance and normal stress are all interrelated during frictional sliding (*Queener et al., 1965*).

These more modern theories of friction were later tested and examined in rock discontinuities. *Patton (1966)* showed that the initial surface roughness controls the frictional behavior of rock interfaces at low normal stresses. Patton's work is later echoed in Byerlee's law (*Byerlee, 1978*) who confirmed that under high normal stresses the contribution of surface roughness to friction is negligible, arguing that under high normal stresses friction is solely

dependent upon the material properties and the level of normal stress. These pioneering works are important cornerstones of rock mechanics but they do not portray surface roughness realistically enough, as they study ground rock surfaces and are typically expressed by some kind of a fixed roughness (or dilation) angle. In fact, modern studies reveal that natural faults are more complex and are associated with damage zones, branching and segmentation (Sibson, 1977; Chester *et al.*, 1993). Field measurements of natural fault surfaces display roughness at all measurable scales, ranging from millimeters to kilometers (Brown & Scholz, 1985; Power *et al.*, 1988; Wesnousky, 1988; Renard *et al.*, 2006; Sagy *et al.*, 2007; Candela *et al.* 2009). Unlike many experimental configurations, the amount of displacement in one faulting event or earthquake is small in comparison to the average fault's roughness (Scholz, 2002). In addition, the fault geometry and roughness play a central role in the state of stress around faults (Chester & Chester, 2000; Sagy & Brodsky, 2009) and in the dynamic-kinematic characteristics of faulting (Kanamori & Brodsky, 2004; Dunham *et al.*, 2011).

The modern approach to fault surface geometry requires additional experimental study of frictional sliding of rough rock surfaces which exhibit a more realistic geometry. Nonetheless, experimental investigations in this regard are strenuous because of the geometric variability of the surfaces, which in turn affects frictional behavior and vice versa (Santner *et al.*, 2006, Chen *et al.*, 2013). Yet, while the resistance to shear due to friction and wear of rock surfaces during sliding were investigated extensively at the laboratory experiments level (e.g., Byerlee, 1978; Dieterich, 1979; Biegel *et al.*, 1992; Wang & Scholz, 1994; Reches & Lockner, 2010; Hirose *et al.*, 2012; Boneh *et al.* 2014), the characteristic of roughness evolution during sliding remains enigmatic.

1.3 Research Goals

Quantifying roughness evolution on the basis of field observations is laborious because of the inherent variability in lithology and tectonic setting of the studied outcrops which affect wear. Post faulting exhumation and erosion processes also affect exposed fault surface morphology (Brodsky *et al.*, 2011).

The present work is therefore adopting an experimental approach for studying fundamental processes of roughness evolution in rocks during frictional sliding. Slip surface morphology is evolved by wear and therefore assumed to be affected by slip amount and by normal stress. Previous experiments on rough rock surfaces indicated that under low normal stresses (2 MPa) the surface topography becomes smooth at all measurable scales as a function of slip (Davidesko *et al.*, 2014). The main goal of the present experimental work is

to study the effects of normal stress on the evolution of mating rough surfaces during shear. Furthermore, because roughness, stress, slip and friction are all interrelated, this study also focuses on the relation between the roughness evolution and the mechanics of frictional sliding.

2 Scientific Background

2.1 Surface Roughness

It is well known that surfaces of any material are not nominally flat (*Bowden & Tabor, 1950*), some surface topography which deviates from a planar surface exists even in seemingly flat surfaces. This topography is referred to as the surface roughness or surface topography, similar to large scale topography, and is comprised of peaks and valleys.

When two surfaces come in contact, they connect only via the tips of the surface topography maximums - known as ‘asperities’, leading to the realization that the real area of contact between two surfaces is smaller than the nominal area of each surface (*Bowden & Tabor, 1950; Archard, 1953*). When applying a normal load on these surfaces the real area of contact between them grows, due to: (1) increase in number of contacting asperities (asperity junctions) ; and (2) increase in the contact area between existing asperity junctions (*Archard, 1953; Wang & Scholz, 1994; Persson, 2006*).

Roughness measurement techniques for surfaces are widely used in engineering science. One of the most commonly used is the Root Mean Square (RMS) roughness defined as:

$$RMS = \left[\frac{1}{L} \int_0^L y^2(x) dx \right]^{0.5} \quad (2.1)$$

Where L is the profile length, y is the height of a point on the profile, and x is the distance along the profile. Higher values of RMS correspond with a rougher surface and vice versa. Looking at equation (2.1), the RMS roughness is defined for a specific length (L). The same surface can exhibit different values of roughness depending on the measured scale, for a seemingly flat surface the RMS values will be higher for small scales (short profile lengths) opposed to lower RMS values when measuring the entire length of the surface (Figure 2.1; Figure 2.2). This leads to the understanding that surface roughness is scale dependent (*Mandelbrot, 1983; Brown & Scholz, 1985; Power et al., 1988*). That is, it should be noted that not all surfaces are scale invariant.

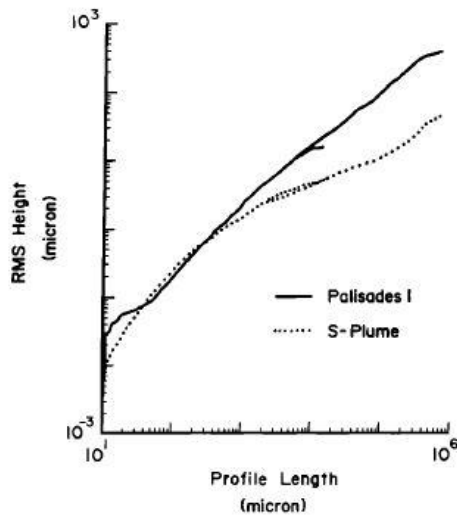


Figure 2.1. RMS height vs. Profile length (which corresponds with wavelength) plot for two surfaces; natural joints in Palisades Diabase and siltstone (Brown & Scholz, 1985).

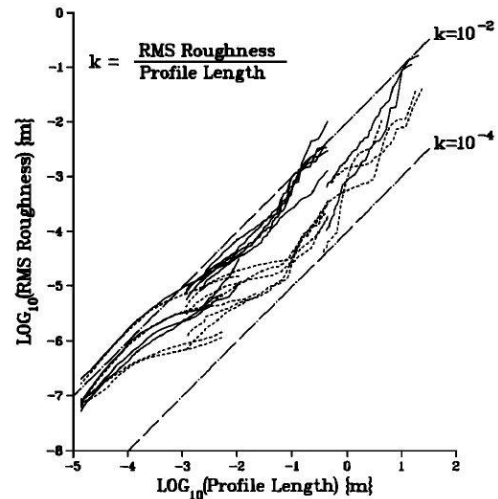


Figure 2.2. RMS roughness vs. profile length (which corresponds to the wavelength) plot for various profiles of natural fault surfaces. The dashed lines refer to profiles in direction of slip and the solid lines refer to profiles in direction perpendicular to slip. k represents the relation between the logarithm of the RMS roughness and the logarithm of the profile length, suggesting a power law (Power et al., 1988).

2.2 Roughness of Natural Fault Surfaces

Geometry and roughness of fault surfaces play a central role in the state of stress around faults and the dynamic-kinematics characteristics of faulting (Chester & Chester, 2000; Brodsky et al., 2011). The presence of wear material, known as gouge or breccia, in natural fault zones indicates that the fault surface itself evolves through slip (Sibson, 1977; Scholz, 2002). Although faults have a complex structure they usually contain principal slip surfaces (Chester et al., 1993) which, like in other materials, exhibit surface topography or roughness. Power et al. (1988) suggested that natural fault surface roughness can be described as a statistical self-similar fractal pattern, meaning that a small portion of the fault surface, when magnified, looks statistically the same as a larger portion of the surface (Mandelbrot, 1983). More recent field works, which use advanced measuring tools, demonstrate the anisotropy of natural fault surfaces with typical self-affine fractal geometry. Moreover, these studies suggest that a universal power-law characterizes fault surface roughness across a wide range of scales, from sub-millimeters to tens of meters (Renard et al., 2006; Candela et al., 2009). Self-affine fractals differ from self-similar fractals by scaling differences of the pieces that make up the fractals. Meaning that a portion of a fractal, defined in the x and y directions, will be self-similar if the x dimension of the fractal scales with the y dimension of the fractal, or self-affine if the x dimension does not scale with the y dimension (Mandelbrot, 1983). Statistical scale invariance is demonstrated in eq. (2.2):

$$\Delta x \rightarrow \lambda \Delta x \quad \Delta y \rightarrow \lambda^H \Delta y \quad (2.2)$$

Where, y corresponds to the height difference between two points separated by a distance x . The exponent H is the roughness or Hurst exponent which is a constant parameter that characterizes the invariance. The value of the Hurst exponent ranges between $0 \leq H \leq 1$ for self-affine fractals, where $H=1$ corresponds to statistical self-similarity (*Simonsen et al., 1998; Simonsen et al., 2002*).

Spectral methods are extremely useful for describing and measuring surface roughness because they consider the distribution of roughness between different wavelengths (*Hansen & Schmittbuhl, 2003*). Surfaces are measured directly in the field or the laboratory using laser or contact profilometers, although the latter is labor intensive and provides a much smaller database than the former. The profilometer data consist of height measurements along a line at a predetermined frequency, the data is analyzed using a Power Spectral Density (PSD) function : (1) the data undergoes decomposition into the frequencies (or wavelengths) that make up the profile using the Fourier transform; (2) the PSD function computes the power of the Fourier components that compose the profile for each frequency (or wavelength); (3) the PSD values are plotted against the wavelengths, equation (2.3). Higher PSD values for a given wavelength correspond with greater roughness at this scale. Moreover, indirect measurements of RMS can be calculated for a given profile, using Parseval's theorem which relates the RMS to the PSD function (chapter 3). The PSD function is given as:

$$p(k) = C k^{-\beta} = C \lambda^{\beta} \quad (2.3)$$

Where C is a constant, β is the power and its value ranges between 1-3 in self-affine profiles (and exactly 3 for self-similar profiles), k is the frequency, accordingly λ is the wavelength ($1/k=\lambda$). The PSD as a function of wavelengths is preferred in this study.

When plotted in arithmetic space (Figure 2.3), PSD functions of self-similar surfaces exhibit a constant characteristic slope in the range of 2-3 (*Scholz , 2002*). This behavior is related to the mathematics behind fractals.

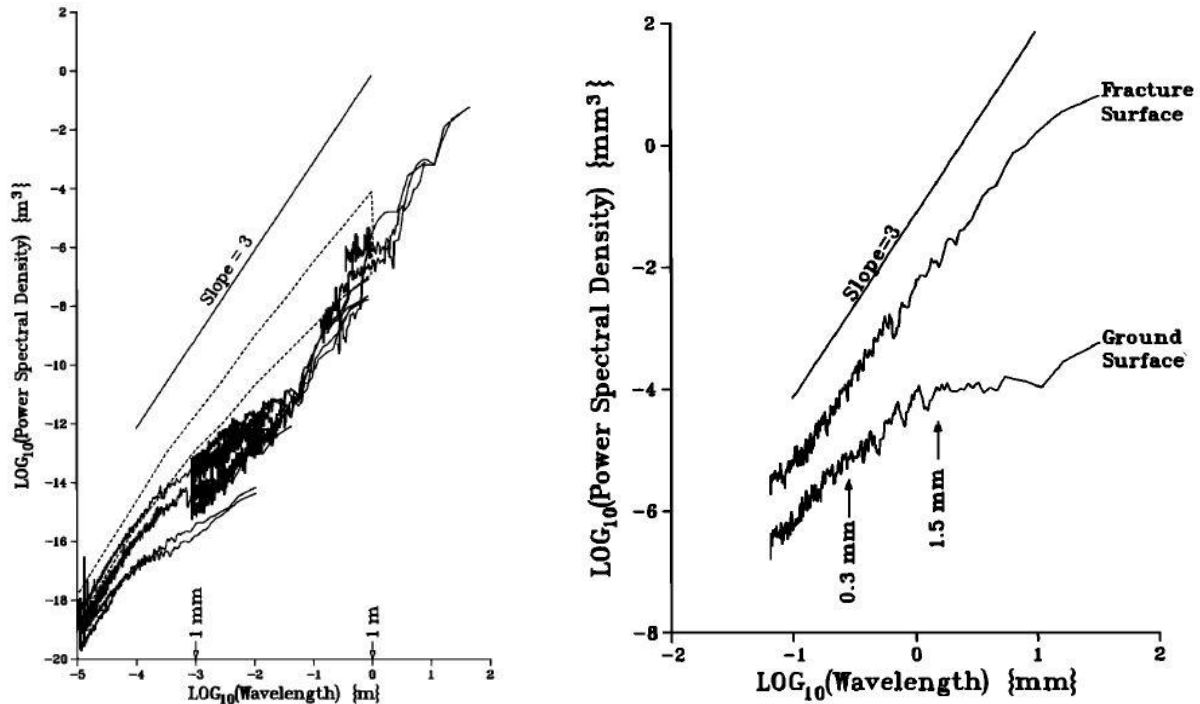


Figure 2.3. Typical Power Spectral Density vs. wavelength curves for rock surfaces. Left - natural rock surface spectra including fault surfaces, bedding planes and glacial wear surfaces measured parallel to slip. Right - artificial laboratory made surfaces of Westerly Granite, the fracture surface is a dynamic tension fracture. Note the change in the PSD curve slope at 0.3 mm wavelength and the corner frequency at 1.5 mm wavelength. A line of slope 3 is plotted on both plots for comparison with a self-similar fractal surface behavior (Power *et al.*, 1988).

The power of the PSD function (β) is related to the Hurst exponent (or the roughness exponent) through brownian field theory (Simonsen *et al.*, 1998):

$$H = \frac{\beta - 1}{2} \quad (2.4)$$

Where H is the Hurst exponent and β is the power of the PSD function. Hurst exponent values range from 0 to 1 for self-affine fractals, which relate to the correlation between two neighboring points on a profile. Higher values ($H \rightarrow 1$) relate to a fast increasing correlation function between the measured length and its amplitudes, lower values ($H \rightarrow 0$) relate to slow increasing correlation function. It should be noted that the roughness exponent is not a direct indication of the surface morphology (Simonsen *et al.*, 1998; Simonsen *et al.*, 2002; Tatone & Grasselli, 2013). Furthermore, the H can also be of negative value, which corresponds with anticorrelations between the measured lengths and their amplitudes and weak persistence. No correlation is depicted by $H = -0.5$ (known as “white noise”), which looks, in real space, like a flat surface ($H = 0$) (Malamud & Turcotte, 1999).

Several works suggest that tensional fractures, as well as faults in direction perpendicular to slip display high values of the Hurst exponent, 0.8 (Amitrano & Schmittbuhl, 2002; Renard *et al.*, 2006; Candel *et al.*, 2009). Lower values of the Hurst exponent (0.6-0.7)

are measured in faults in direction parallel to slip (*Candela et al., 2009; Candela et al., 2011*).

Experimental rough surfaces which demonstrate the self-affine geometry can be produced for laboratory use. *Power et al. (1988)* showed that surfaces of a dynamic tension fracture in Westerly Granite exhibit a self-affine roughness pattern. *Davidenko et al. (2014)* produced similar surfaces in limestone and reached a similar conclusion. These self-affine surfaces produced in the laboratory by means of tensile rupture are intrinsically different from ground flat surfaces that are in common use in rock friction experiments. The ground surfaces display small scale roughness much like self-affine surfaces due to cutting method (saw-tooth) or due to artificial smoothing using grit. But at larger scales the surfaces are smooth and vary from self-affine behavior. This difference is clearly visible from the PSD plots (Figure 2.3), the spectra for the ground surface has a corner frequency at wavelength 1.5 mm and a change in slope at a wavelength of 0.3 mm.

2.3 Frictional Sliding of Surfaces and Wear Processes

Frictional sliding and wear production are interrelated processes. Field work on natural faults indicates this elegantly from thickness measurements of fault zone gouge and breccia which increase with fault displacement (*Otsuki, 1978; Robertson, 1983; Scholz, 1987*).

Scholz & Engelder (1976) suggested that rock friction could be explained by the adhesion theory of friction first proposed by *Bowden & Tabor (1950)*. Adhesion theory suggests that when two surfaces are in contact with each other the real area of contact is smaller than the nominal area of the surfaces, as discussed before. The surfaces contact each other via asperity junctions, hence the normal stress at these junctions will be very high and ultimately exceed the yield strength or the penetration hardness of the material. The contacts would become welded together, thus requiring a significant tangential force across the surfaces to cause sliding, the threshold of which would be the yield strength of the welded elements. While this theory works well for metals, as they deform plastically both in shear and compression, it is only partially valid for rocks, as they typically fail by brittle fracture (*Byerlee, 1967; Byerlee, 1978; Scholz, 2002*).

During frictional sliding of one surface against another, asperities from the two opposing surfaces interact with each other and with the opposing surface itself through several mechanisms (Figure 2.4): ploughing, riding-up and interlocking (*Wang & Scholz, 1994*). Ploughing is usually common between two different materials (with hardness difference) contacting each other. Riding-up (known also as "gliding") is the elastic deformation of the

asperities, causing one to climb over the other. During shear displacement, the asperity summits grind one another and create new wear particles. The interlocking mechanism prohibits the asperities to climb over each-other, thus causing the asperities to yield plastically or more commonly to fail by brittle fracture (Scholz, 2002). It is assumed, in the interlocking mechanism, that the asperities decapitate each other's summits thus producing wear particles and modifying the initial surface geometry (Scholz, 2002).

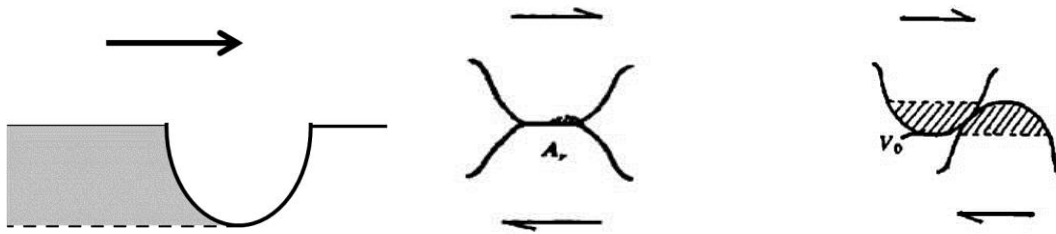


Figure 2.4. Asperity interactions during frictional sliding of rock surfaces. Left - ploughing, the asperity ploughs the opposite surface creating a groove (shaded area). Center - riding up, the asperities from both surfaces climb over each other and connect via their tips. Right - interlocking asperities, the asperities lock thus causing them to shear-off during shear displacement (Scholz, 2002).

Wear formation was studied intensely in mechanical and materiel engineering disciplines in the past, providing an important wear model introduced by *Queener et al. (1965)* in their formula for wear of machine parts:

$$W = \beta(1 - e^{-nL}) + KL \quad (2.5)$$

Where W is the total weight loss due to wear (from a sample undergone sliding), n is a constant, L is the total sliding distance, β and K are the proportionality constants for the transient wear rate and the steady state wear rate, respectively.

Queener et al. (1965) showed that at the onset of frictional sliding the wear production rate is controlled by a "transient wear rate" stage, during which the initial roughness of the sliding surfaces is sheared off to produce new wear particles. Most of the surface topography changes at this stage. At long sliding distances the wear rate reduces and enters a "steady state rate" stage where wear continues to form but at a constant rate proportional to $W \approx \beta + KL$. The authors also conclude that the β coefficient depends on the initial surface roughness, a rougher surface will need to slide a longer distance to reach the steady state stage opposed to a smoother surface and will produce more wear material during both stages (Figure 2.5). Moreover, n is a constant that scales the load, higher loads relate to higher wear rates at the transient stage.

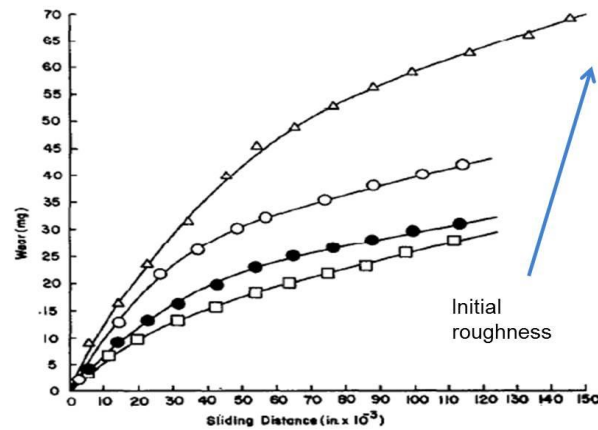


Figure 2.5. Wear-sliding distance curves for different steel surfaces with different initial roughness. For smoother surfaces the transient wear stage is short (open squares curve), whereas for rougher surfaces the transient wear stage is longer and more wear is produced during sliding (Queener *et al.*, 1965).

Wang & Scholz (1994) showed that wear formation in ground rock surfaces was similar to that in metal surfaces because the surfaces interact with one another through the same mechanism of contacting asperities. Their experiments showed that when the applied normal stress acting on rough surface contact increased, larger volumes of wear were produced. They suggested that at higher normal stresses the contact between the two surfaces was tighter and consequently the asperities from the two opposing surfaces interlocked more tightly. This led to more asperities being sheared off rather than deforming elastically and climbing over each other. Wang & Scholz (1994) also validated equation (2.5) in rocks, suggesting that rock surfaces undergo two stages of wear formation, the transient and steady state stages. While this mechanism is acceptable in ground surfaces it has not been studied thoroughly in self-affine rough surfaces. Power *et al.* (1988) inferred that because natural faults are rough at all scales and exhibit a self-affine geometry, they may never reach the steady state stage and that all wear production must take place during an ongoing transient stage. This understanding leads to the conclusion that according to eq. (2.5) wear production is dependent on slip distance, load and surface roughness, all of which may change after every slip event.

2.4 Effects of Normal Stress on Frictional Sliding of Joints and Faults

The occurrence of earthquakes and faults extends from shallow depths of several kilometers, down to the upper mantle at depths up to 700 km in the Wadati-Benioff zones (Stein & Wysession, 2003). All of these faults are subjected to varying levels of stress, whether of lithospheric, tectonic or fluid pressure origin, and all these stresses may act simultaneously.

Amontons's second law of friction concludes that friction is proportional to the normal force (Scholz, 2002). This observation was validated by the works of Bowden and Tabor

(1950) and Archard (1953). As discussed before, surfaces contact each other via asperities, when normal load is applied the number of contacts and their size grows. When the contacting area increases the frictional strength of the interface between the surfaces increases as well, this concept is echoed in Coulomb's strength criterion for rock joints where an increase in normal stress leads to an increase in shear strength of the joint (Jaeger *et al.*, 2007) :

$$\tau = s_j + \sigma_n \tan \phi_j \quad (2.6)$$

Where τ is the shear strength of the joint, S_j is the cohesion of the joint, σ_n is the applied normal stress and ϕ_j is the joint friction angle in degrees. According to Coulomb, the shear strength of the joint is related linearly to the applied normal stress. Patton (1966) modified Coulomb's classic strength criterion by adding the effect of surface roughness. Patton showed that for a saw-tooth surface geometry the empirical strength criterion is bi-linear comprising of two regions: (1) low normal stress region and; (2) high normal stress region (Patton, 1966):

$$\begin{aligned} \tau &= \sigma_n \tan(\phi_b + i) && \text{at low } \sigma_n \\ \tau &= C + \sigma_n \tan \phi && \text{at high } \sigma_n \end{aligned} \quad (2.7)$$

Where τ is the shear strength, σ_n is the normal stress, C is the cohesion of the rock, ϕ_b is the basic friction angle of the surface (smooth surface), i is the roughness angle (Figure 2.6) and ϕ is the internal friction angle of the rock.

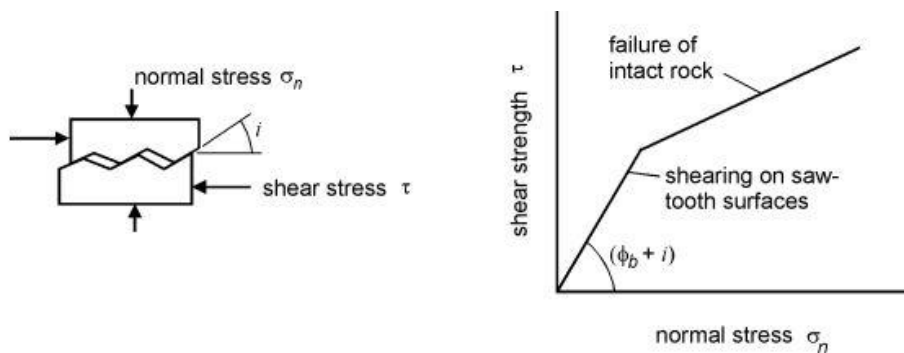


Figure 2.6. Patton's model: the saw-tooth surface geometry showing the angle of the saw-tooth face, i (left), and the bi-linear strength criterion showing two distinct regions of low normal stress and high normal stress (right). The low normal stress region depends on both the basic friction angle of the surface (ϕ_b) and the roughness angle (i), whereas the high normal stress region depends solely on the friction angle of the intact rock and its cohesion (Goodman, 1989).

Patton determined, through shear tests on rough saw-tooth specimens that under low normal stresses the rough surfaces climbed over the inclined teeth, causing the dilation of the specimens. Under high normal stress, however, the saw-teeth interlocked, causing the asperities to break off, resulting in a shear strength behavior that is more closely related to the intact material strength rather than to the frictional characteristics of the surface (Goodman, 1989; Hoek, 2014).

While Patton's approach provides a good framework, it is oversimplified. This is primarily because representation of an entire roughness profiles in terms of a single dilation angle (or uniform wavelength) is overly simplistic and unrealistic. Moreover, shear strength response to changes in normal stress is a smooth function and not bi-linear as originally suggested. *Barton (1976)* and *Barton & Choubey (1977)* studied natural rock joints and suggested that equation (2.7) could be rewritten as follows, for low normal stress regime:

$$\tau = \sigma_n \tan \left[\phi_b + JRC \log_{10} \left(\frac{JCS}{\sigma_n} \right) \right] \quad (2.8)$$

Barton defined two coefficients: (1) *JRC* - joint roughness coefficient, which is attainable through comparing the appearance of the discontinuity surface to standard profiles published by Barton and others; (2) *JCS* - joint wall compressive strength, which scales the unconfined compressive strength of the joint wall material (for suggested method for determination see *ISRM (1978)*).

Barton's shear strength criterion considers surface roughness, asperity material strength, and normal stress as key parameters in determining the mechanical behavior of discontinuities. Another advantage over Patton's law (or Byerlee's for that matter – see below) is that the shear stress function is non-linear as typically obtained in laboratory shear tests.

Byerlee (1978) summarized hundreds of shear experiments on ground surfaces of various rock types to conclude his law, known as Byerlee's law:

$$\begin{aligned} \tau &= 50 + 0.6\sigma_n && \text{for } \sigma_n > 200 \text{ MPa} \\ \tau &= 0.85\sigma_n && \text{at lower normal stress} \end{aligned} \quad (2.9)$$

Where τ and σ_n are the shear strength of the surface and the applied normal stress respectively, the law is in MPa. Note that again, as in the case of Patton's law, the obtained shear strength failure envelope is bi-linear over a wide range of normal stresses.

Byerlee's law is a first order law, it is independent of roughness, sliding velocity, lithology and temperature (for silicates up to a temperature of 350°C) and it is widely used in seismology and geophysics. Byerlee concluded that at low stresses, encountered in most civil engineering problems, rock friction varies between wide limits, this variation is mainly because at these low stresses friction is strongly dependent on surface roughness. However, at intermediate to high stresses, such as encountered in deep mining engineering problems and deep crustal faults, the initial surface roughness has little or no effect on friction (*Byerlee, 1978*).

2.5 Roughness Evolution of Fault Surfaces

As mentioned before, frictional sliding of rock surfaces generates wear. The production of wear particles causes the surface geometry to change and each slip event changes the geometry. Consequently, the surface geometry evolves through slip.

Field measurement results of natural faults suggest that faults smooth with slip, as faults mature they evolve geometrically to simpler shapes (*Sagy et al., 2007; Brodsky et al., 2011*). Utilizing spectral methods for roughness measurements of fault surfaces, *Sagy et al. (2007)* and *Brodsky et al. (2011)* showed that small slip faults are rougher in direction of slip while large slip faults are smoother (but still maintaining a non-planar geometry). This observation encompassed faults from different geological and tectonic settings and in various lithologies. *Wesnousky (1988)* observed strike-slip fault traces at map scales and discovered that the number of steps along the trace reduces with increased offset on the faults. Surface smoothing induced by slip was also validated by experimental data. *Davidenko et al. (2014)* studied the roughness evolution of self-affine dynamic tensile fractures in limestone. Using RMS and PSD roughness measurements, they concluded that surface geometry smooth with displacement, the change in roughness intensified with growing displacements. This behavior was observed for small-scale roughness of millimeters to centimeters.

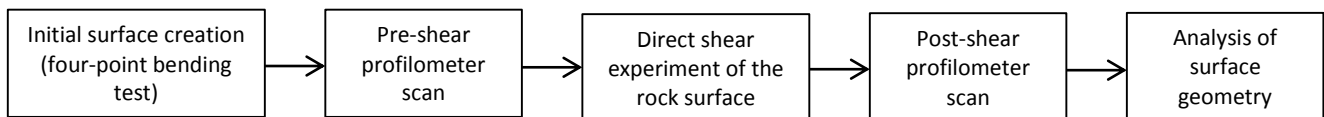
More experimental research was conducted in recent years regarding roughness evolution. *Renard et al. (2012)* slid halite on a coarse sandpaper substrate under constant normal stress and characterized the developed roughness using white light interferometry. They observed slip-parallel linear striations as well as deformation products and gouge formation. Some of the striations were bounded by brittle, triangular fractures that fragmented the surface of the halite slider and generated breccia or gouge (*Renard et al., 2012*). *Boneh et al. (2014)* used a rotary shear apparatus for a fault evolution study on flat rock surfaces made of different rock types including Tonalite, Dolomite and Sandstone at various slip velocities and distances (recognizing short and long slip distances), under varying low normal stress (up to 6.9 MPa). They concluded three stages of roughness evolution and wear production, depending on slip distance: (1) an initial stage of slip distance < 50 mm, where the surfaces exhibited roughening, including morphological features as deep pits associated with plucking of the surface material; (2) a 'running-in' stage of slip distances of 1-3 m, where the surface smooth and the wear-rate intensifies; (3) steady-state stage which is initiated once the fault surface is covered by a gouge layer that acts as a lubricant and reduces wear production, roughness change and friction.

3 Methods

The research methods were obtained in four different stages:

1. Creation of initial tensile fracture surface by four-point bending tests performed on limestone beams.
2. Direct shear experiments of tensile fracture surfaces created in (1) using hydraulic servo-controlled direct shear system.
3. Surface geometry measurements (before and after the direct shear tests) using a laser profilometer.
4. Data reduction and analysis using Matlab software.

Each sample undergoes the following sequence:



3.1 Creation of Initial Experimental Fault Surface

Experimental fault surfaces were created by dynamic tensile fracture, as proposed by *Power et al. (1988)*. Prismatic limestone beams were set in four-point bending configuration in the direct shear system at Ben-Gurion University (Figure 3.1). Before loading begun, an initial artificial notch (~5 cm long) was created on the lower fiber of the beam using a rock saw. The notch predetermines the start and direction of the tension fracture.

The four-point bending configuration is comprised of the prismatic beam which rests upon two bases (Figure 3.1); the force from the bases is transmitted to the beam via two steel rods which sit in shallow grooves carved in the beam. The normal piston applies the vertical force to the upper fiber of the beam via two steel rods (which also sit in pre-made shallow grooves in the beam). During the test, tensile forces are induced and stress concentration begins to build up at the singularity of the crack tip on the lower fiber of the beam. At failure, the beam breaks in two as a continuation of the initial crack, thus creating two mating surfaces with a random surface geometry.

The beam dimensions are as follows:

Length = 50 cm

Height = 19 cm

Width = 8 cm

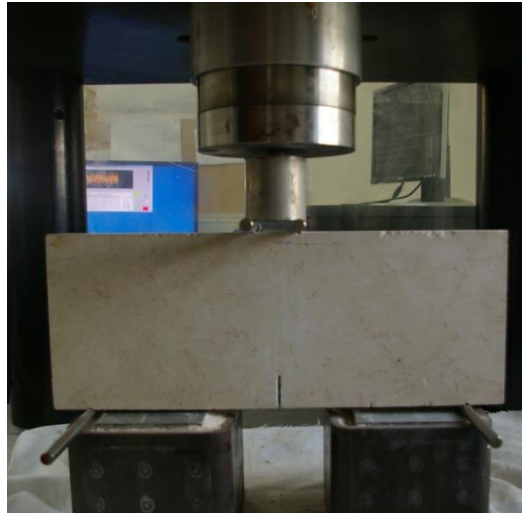


Figure 3.1. Limestone beam in four-point bending configuration prior to loading. The normal piston of the direct shear system (top of figure) presses the top fiber of the beam, the load is gradually increased until the beam fails, thus creating the tensile fracture. Note the initial notch at the lower fiber of the beam, the loads are transferred to the beam via the steel rods. The length of the beam is 50 cm.

3.2 Direct Shear Experiments

3.2.1 Direct Shear System

The direct shear system allows simultaneous application of horizontal (shear) and vertical (normal) forces on two rock surfaces (in this study, experimental fault surfaces) using hydraulic pistons. Through direct shear tests, the shear strength of intact and fractured rock can be determined. The direct shear system at the Rock Mechanics Laboratory of the Negev at Ben-Gurion University (Figure 3.2) is a single plane shear system designed and manufactured by TerraTek System Inc. USA (model DS-4250), the normal and shear pistons can apply a maximum force of 1000 kN and 300 kN, respectively. The system is composed of four main components:

1. Hydraulic pump which provides oil pressure for hydraulic pistons.
2. Hydraulic pistons in perpendicular directions (normal and shear).
3. Real time closed-loop servo controlled system that monitors the displacements, forces and stresses that the pistons apply on the sample.
4. Real time dynamic data acquisition from all channels and storage.

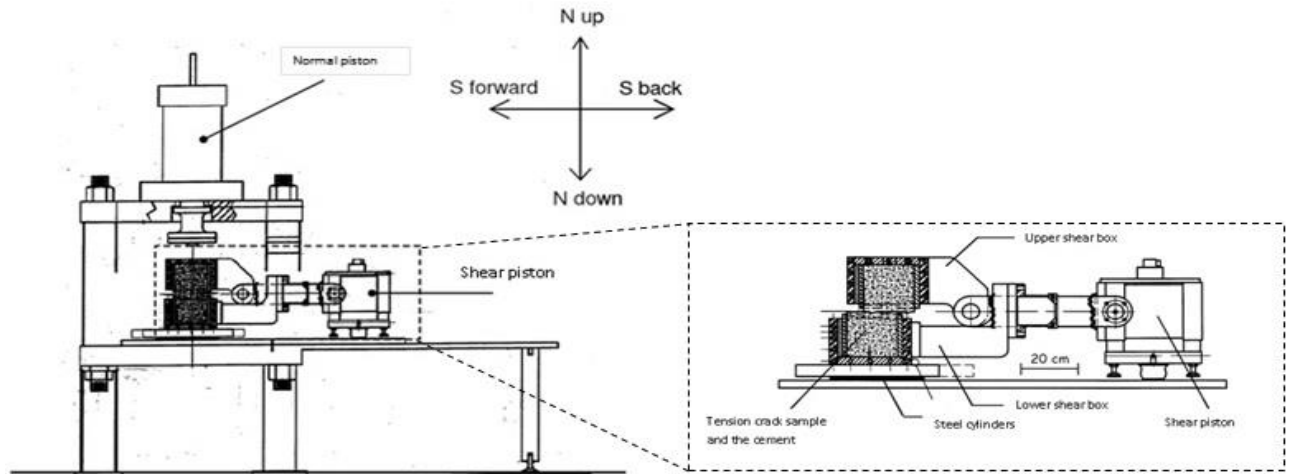


Figure 3.2. Schematic illustration of the TerraTek DS-4250 direct shear system. Inlet: a close up of the shear piston and shear boxes. Note that the upper shear box remains stationary throughout the experiment while the lower shear box which is connected to the shear piston is capable of linear motion.

The tested samples are fixed to steel frames (refer to section 3.2.2) that are loaded into the upper and lower shear boxes of the direct shear system (Figure 3.2). The shear boxes link the experimental surfaces to the normal and shear pistons of the system. During testing, the upper shear box remains stationary while the lower shear box moves as it is attached directly to the shear piston and can move forwards and backwards over frictionless rollers positioned between the base platen and the lower shear box.

Displacement and force measurements are done by the direct shear system throughout a test. Forces are measured directly using built-in load cells on the normal and shear pistons, stresses (normal and shear) are calculated automatically during testing according to the nominal surface area (upper shear box) which is a required input parameter before starting a test, using the terms for shear and normal stress respectively:

$$\tau = \frac{F_{shear}}{A} \quad (3.1)$$

$$\sigma = \frac{F_{normal}}{A} \quad (3.2)$$

Where, F_{shear} and F_{normal} are the shear and normal forces respectively, and A is the nominal surface area. When dividing equation (3.1) by equation (3.2) the coefficient of friction (μ) can be calculated:

$$\mu = \frac{\tau}{\sigma} \quad (3.3)$$

Displacements are measured by displacement gauges in the pistons and by electric transducers. Two fiber optic displacement transducers monitor the position of each piston

separately, meaning each piston can be controlled by its load cell or displacement transducer. Therefore, two control modes are always available for each piston: Load and Displacement. Metal plates are connected to the outer edges (in relation to the direction of shearing) of each steel frame (Figure 3.3). Then, six linear variable displacement transducers (LVDTs) are mounted onto the plates, four vertical LVDTs (labeled Xa-Xd) next to the corners of the frame and two horizontal LVDTs (labeled Ya-Yb) - one on each side of the frame (Figure 3.3). The vertical LVDTs monitor the vertical displacements between the upper and lower frames, whereas the horizontal LVDTs monitor the relative horizontal displacement of the frames using the average displacement of both transducers.

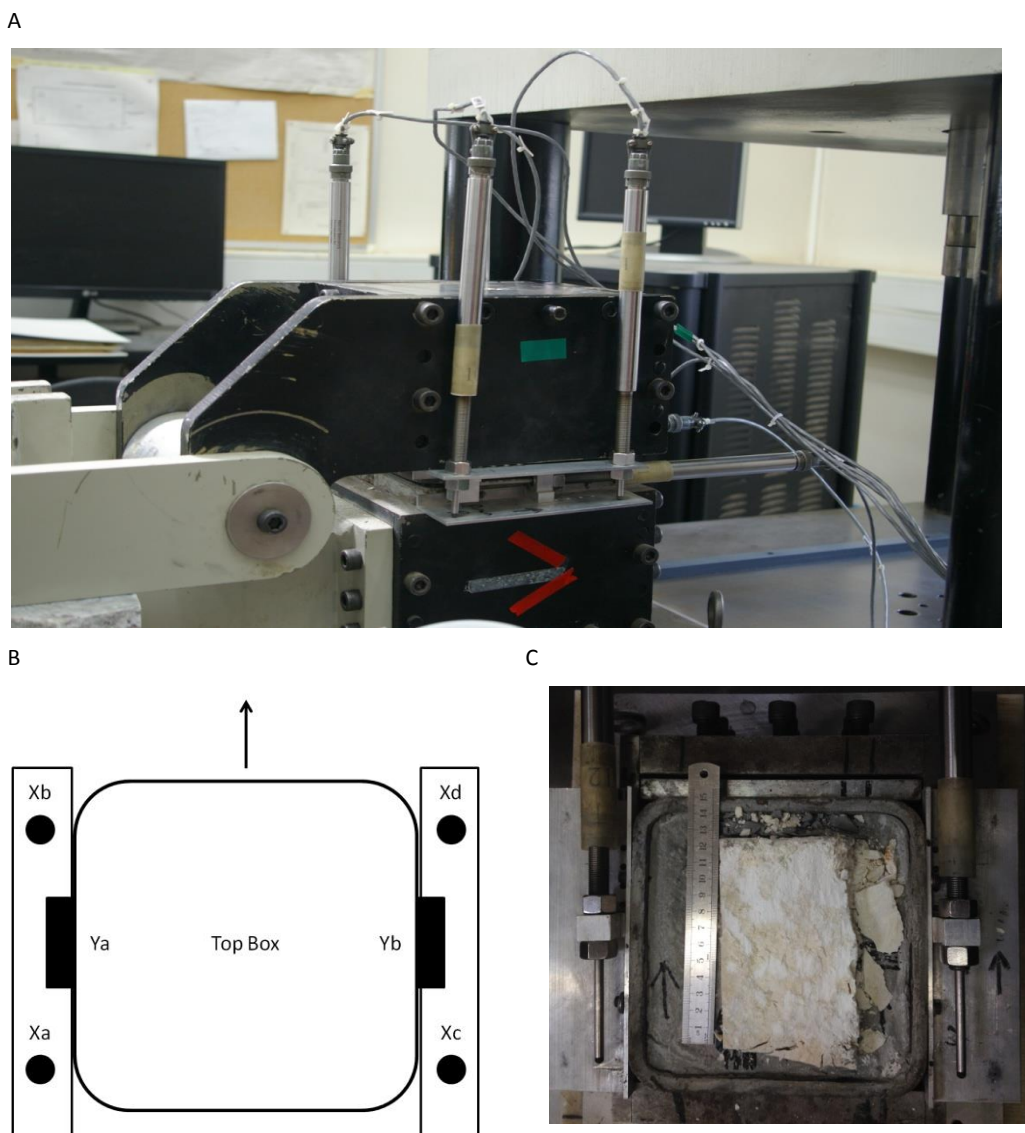


Figure 3.3. LVDT configuration on the direct shear system: (A) Direct shear system configuration including: top and bottom shear boxes and LVDTs (normal and horizontal) in place before a shear test. The red arrow taped to the lower shear box indicates the direction of shear. (B) Schematic illustration, looking down at the top shear box, four vertical LVDTs, labeled Xa-Xd, measure dilatation while two horizontal LVDTs, labeled Ya-Yb, measure the relative displacement between the two shear boxes, or the shear displacement. The arrow indicates the direction of shear. (C) Photograph of the lower shear box (the top box is raised and not seen in the picture) with the attached horizontal LVDTs, notice the proximity of the LVDTs to the sample (length of sample is ~12cm). Note the dry cement filling the space between the rock and the outer profile of the steel frame.

All direct measurements are connected through separate channels to the real time closed-loop servo control system. The pistons can be controlled by: (1) the applied load - using the load cells; or (2) through displacements - using the displacement transducers on the pistons, or more precisely using the LVDTs which are mounted very close to the tested interface (Figure 3.3), the preferred method in this study.

The servo-control system is comprised of two interconnected computers: the TerraTeK real time (TTRT) computer and the user interface computer (UIC). The TTRT computer monitors, collects and processes input signals from the direct shear system. The second component, the UIC, allows the user to control the entire system. The UIC unit is supplied by custom-made software provided by TerraTek to work directly with the specific direct shear system. All test parameters, algorithms and controls are input into the UIC by the user when conducting a test. Moreover, all of the acquired data is accessible to the user via the UIC.

It should be pointed out that in a system of this configuration the normal stress is applied from one direction and this can be a source of uneven normal stress distribution across the tested interface (fracture surface). The influence of this test artifact on the resulting shear behavior is considered negligible for the purpose of this study.

3.2.2 Setting up a Test

The two rock blocks with mating surfaces created before in four-point bending methodology are cut with a circular rock saw in order to dispose of the unused ends of the original beam structure. One surface must be smaller than the other to ensure that all of the surface area will be sheared the same distance. Hence, one of the blocks is cut again thus reducing the nominal size of the surface. Afterwards, the rock blocks with the mating surfaces are placed into two steel frames with the surfaces facing upwards, lab-made cement is cast in order to fix the samples to the frames (Figure 3.3C), and the frames are loaded into the shear boxes of the shear system (Figure 3.3A). As a rule, the smaller surface was loaded into the upper shear box whereas the larger surface was loaded into the lower shear box. This ensures that during displacement, the entire upper surface will be sheared on the lower rock surface and not on the surrounding cement infilling.

3.2.3 Test Procedure

At the start of each test, the experiment properties and boundary conditions are digitally set into the interface computer of the direct shear system controls, including, nominal surface area (of the upper surface), sample name, normal piston velocity and shear piston velocity and the PID parameters. The test itself is divided into two segments: the loading segment and the

shearing segment. First, the normal piston is lowered until it is in contact with the upper shear box; this stage is controlled with the displacement transducer of the piston. Afterwards, the loading segment begins when the normal piston starts to press the boxes to a set load predetermined before the start of the test. Constant load rate of 0.01-0.05 MPa/second is applied via the load cell of the piston. Upon reaching the target normal stress the shear segment begins. The shear piston is activated according to the test parameters of shearing distance and rate. All the tests in this study are conducted at a constant shearing rate of 0.05 mm/second to a target distance of 10 mm. The shear segment is controlled via the average displacement of both horizontal LVDTs. During each test the normal piston is set to hold the normal stress constant throughout the test procedure while allowing the sample to dilate.

A test ends when the target shear displacement is achieved. At this stage the shear piston maintains its position to stop the grinding of the sample while the normal piston is raised to decrease the normal stress acting on the shear boxes. Then, the shear piston is retracted and the shear boxes are open manually and the steel frames with the fixed surfaces are removed from the direct shear system.

3.2.4 Controls and Measurements

During a test, the displacements are measured by the LVDTs attached to the shear boxes. The four normal LVDTs placed at the corners of the boxes (Figure 3.3) provide measurement of the vertical displacements. These measurements provide the dilation/contraction data for each experiment (Figure 3.4). Moreover, the normal LVDTs measurements were used to calculate the normal stiffness (k_n) of each sample during the loading segment using the relation:

$$k_n = \frac{\Delta\sigma_n}{\Delta v} \quad (3.4)$$

Where $\Delta\sigma_n$ is the change in normal stress and Δv is the dilation/contraction.

The shear displacement was measured by the two horizontal LVDTs (Figure 3.3C), the total shear displacement was controlled using the average reading from the two horizontal transducers. In addition, the shear stress measurements were used to calculate the shear stiffness (k_s) of the sample using the relation:

$$k_s = \frac{\Delta\tau}{\Delta u} \quad (3.5)$$

Where $\Delta\tau$ is the change in shear stress and Δu is the shear displacement. This calculation is valid for the linear part of the shear stress vs. displacement curve before peak stress is achieved (τ_p).

All six LVDTs are connected to the servo-controller via six different channels. The proximity of the LVDTs to the sample (Figure 3.3) together with the servo-controller capabilities, provide precise measurements throughout the test.

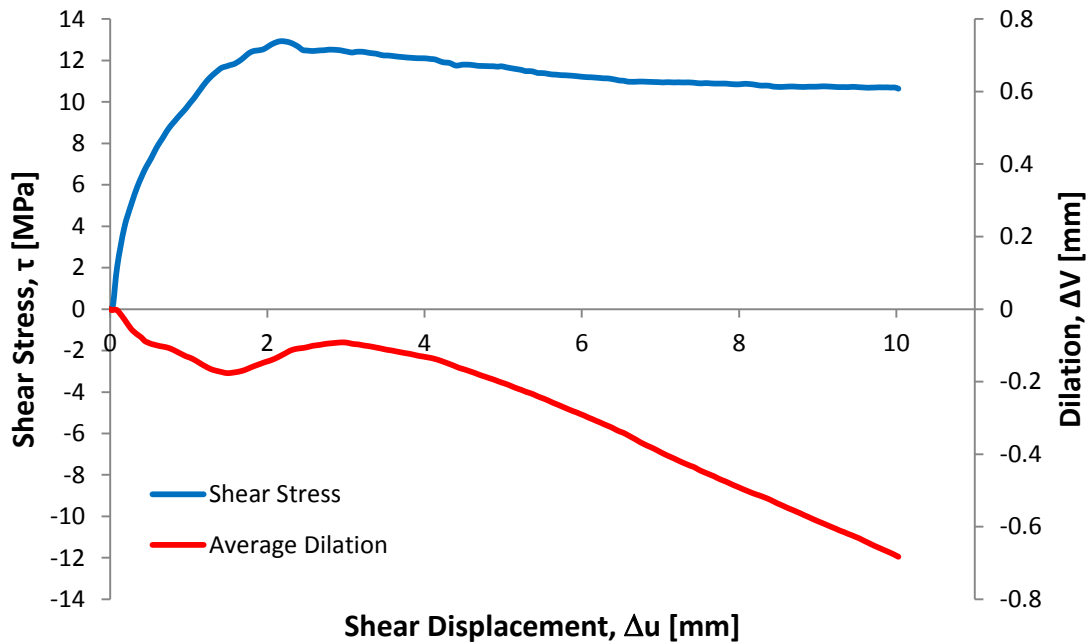


Figure 3.4. Shear stress and dilation vs. displacement in an example of a direct shear test under normal stress of 15 MPa. The blue curve represents the change of the shear stress up to 10 mm displacement, the red curve represents the average vertical dilation of the sample (contraction is negative). The average dilation is the mean displacement of all four vertical LVDTs. The blue curve demonstrates classic behavior of direct shear experiments of rock joints, with the onset of displacement the shear stress climbs to reach a peak stress (at ~ 2.2 mm), afterwards the shear stress drops moderately to reach residual stress. The slope of the shear data (blue curve) prior to peak stress is the shear stiffness (k_s) of the sample. The red curve indicates contraction of the sample from the onset of displacement until reaching peak stress, thereafter dilation until ~ 3 mm and further contraction from then on until the end of displacement at 10 mm.

3.3 Surface Geometry Measurements

Along with the shear tests, the geometrical measurements of the surfaces are at the heart of this study. These measurements are carried out using a laser profilometer (Figure 3.5) that measures the height of a point relative to a reference point. The sampling frequency is set for both horizontal directions thus producing a topographic map of the scanned strip, which provides the geometry of the surface.

3.3.1 The Profilometer

The instrument used in this work is the ConoScan 2000 laser profilometer (Figure 3.5) manufactured by Optimet, Optical metrology Ltd. The profilometer is equipped with three different lenses with focal lengths of: 75, 50 and 25 mm, but only the 75 and 50 mm lenses were in actual use. The profilometer can scan a strip with a length of up to 130 mm and a constant width of 18.636 mm by the 75 mm lens and 12.273 mm by the 50 mm lens. The

measuring frequency is predetermined by the operator for the longitudinal direction (scan direction) but not for the transverse direction (perpendicular to the scan direction) which is fixed for each lens (Table 3.1).

Table 3.1. Scanning properties in transverse direction

Lens	Scan Width [mm]	Transverse Sampling Frequency [mm ⁻¹]	Transverse Spacing Between Points [μm]
50 mm	12.273	52.147	19.2
75 mm	18.636	34.342	29.1



Figure 3.5. The laser profilometer at Geological Survey of Israel during a surface scan. Note that the surface is scanned while still in the steel frame which helps adjust the pre and post-shear scans in the same scanning orientation.

The laser profilometer measures the height of the surface using a laser beam; each point measured with the profilometer has a certain signal to noise ratio (Snr). Higher Snr values mean a higher quality measurement signals. A Snr threshold value is set by the user, this threshold determines if a point is saved to the data file or not. Points of Snr values beneath the threshold value were characterized as "not a number" (NaN) in the collected data (Figure 3.7). Scans in this work were done at typical Snr values of 70% and higher with a Snr threshold of 40%. The overall quality of a measurement depends on the surface-to-lens distance and the surface material itself.

Two types of measurement errors were encountered: (1) "Spikes"; and (2) NaNs (not a number). Spikes are exaggerated measure points in terms of height which do not correlate with the neighboring points. This type of error usually occurs as a measuring artifact at the edges of a scan (Figure 3.8) or because of over reflectivity of minerals on the surface. NaNs are immeasurable points on the surface – points with low values of Snr which appear as holes

in the surface matrices (Figure 3.7). Although the rock material was mostly fine-grained, almost every tested surface had a few areas of mineralization.

The mineralization zone problem was resolved by applying a crack detection surface spray (Flawfinder Developer Spray 63135, manufactured by Rocol). The spray applied a micro-scale fine film on the surface which allowed better data acquisition by the profilometer.

3.3.2 Scanning

Two types of scans were performed; "medium-resolution" surface scans using the 75 mm lens and "high-resolution" scans using both the 75 and 50 mm lens. All of the surfaces were scanned parallel to the shear direction (longitudinal direction). The resolutions are characterized by the different spacing between the measured points. Medium-resolution scans consist of longitudinal (in direction of scan) spacing of 100 μm between the points. High-resolution scans consist of longitudinal spacing of 10 μm between the points for both the 75 and 50 mm lenses.

Medium-resolution scans were done on the whole surface in four different scanning strips (Figure 3.6) -width: according to the focal length of the 75 mm lens- 18.636 mm, length: according to the nominal length of the surface- ~ 110 mm. The typical output data from one medium resolution scan (one strip) is an array of 704,640 points, each with its own x,y coordinate and a height value (z) measured by the profilometer. This array will later on be rearranged, using a Matlab code, as a 640×1101 surface matrix.

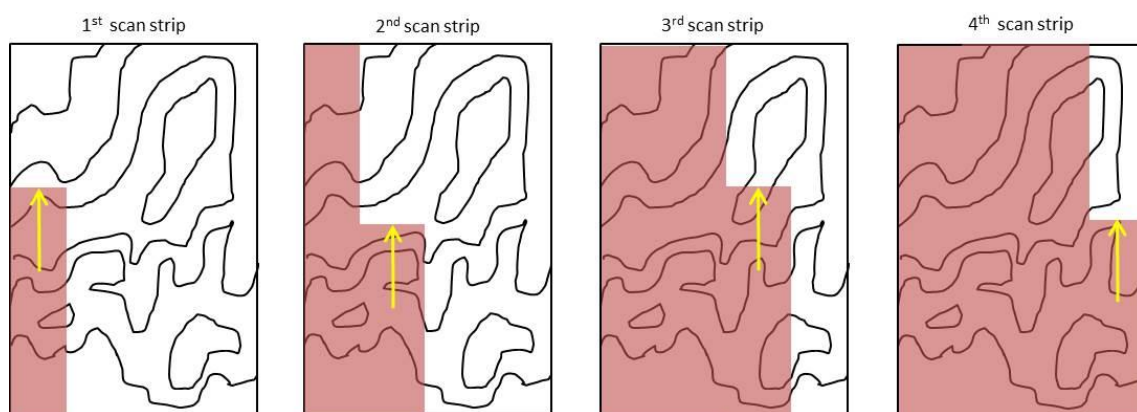


Figure 3.6. Schematic illustration of the whole surface scan using the 75 mm lens. The surface is divided into four scanning strips, the continuous lines denote the surface geometry, the shaded area is the scanned surface area, the arrow shows the direction of the scan (in direction of the shear- longitudinal direction of the sample). Scans begin at the bottom left corner of the sample (left frame) and end at the top right corner of the surface (right frame), thus scanning the entire surface. Each frame represents the same surface of a size of 110×80 mm².

High resolution scans are performed on a much smaller area (12.273 mm wide, ~ 20 mm long), usually two scans at the central area of the surface as to avoid sampling edge effects. The typical output data from one high resolution scan (one strip) is an array of 1,280,640

points, each with its own x,y coordinate and a height value (z) measured by the profilometer. This array will later on be rearranged, using a Matlab code, as a 640×2001 surface matrix.

Because of the surface roughness, it is hard to predict which areas will experience damage and which areas would not even come in contact with the opposing surface after a few millimeters of displacement. Thus it is necessary to scan the entire surface. Four medium-resolution scans of the surface allow full coverage of the entire surface, also making it easier to scan the same strips before and after shearing. Two high-resolution scans from each surface ensure that at least one of them will include shear induced damage. However, some post-shear high-resolution scans are of poor quality or only partially good, due to great damage and wear material presence, and are not included in the analyzed data.

3.4 Data Analysis

The data gathered by the profilometer scans are processed and analyzed by Matlab codes written by Dr. Amir Sagy and Nir Badt.

1. The output data arrays from the profilometer are inputted into Matlab as matrices. The size of each matrix depends on the scanning resolution.
2. The surface matrices are cleaned from NaN points using data filters, the modifications account for less than 5% error in the data for each surface.
3. The damage zones are recognized and analyzed with power spectral density (PSD) and root mean square (RMS) codes.

3.4.1 Surface Matrix Cleaning and Data Filtering

Scanned surfaces include two types of measurement errors, spikes and NaNs. NaN (Not a Number) errors are points with no measured height data, these are "holes" in the data. The NaN errors in a matrix exist in single points or in clusters. Single point and small clusters are common throughout the matrices, even in good quality scans (with small amount of NaNs). Large clusters (or patches) occur as well; usually these patches overlap large-grained mineralized areas of the surfaces. The NaN errors are fixed by filling the "holes" with extrapolated data according to the average height of the surrounding points (which are not NaNs themselves). This filling method is good for small clusters and single point errors (Figure 3.7), for large clusters and patches the interpolation is unreliable, therefore the surface matrix may be cut into a smaller sub-matrix excluding the NaN patch. For example: looking at Figure 3.7; the matrix includes error patches in rows $0 < y < 100$ and around column $x = 800$, between lines $350 < y < 600$. The preferred sub-matrix will be cut according to the limits of

$100 < y < 640$ and $0 < x < 700$, this sub-matrix will include only single point and small cluster NaN errors, which as a rule would not account for more than 5% of the total points of the sub-matrix.

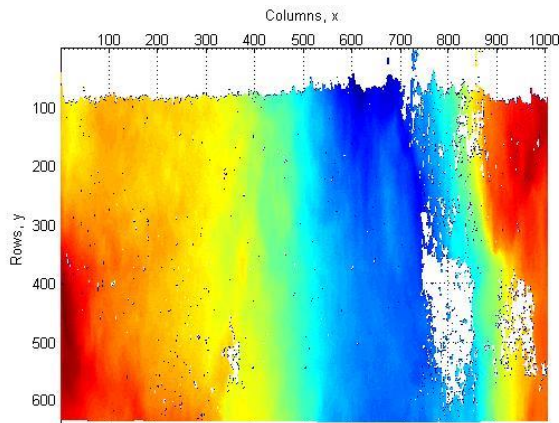


Figure 3.7. Surface matrix in 2D, the color scheme indicates the heights: red – high, blue - low. NaN error point are scattered throughout the surface (white areas), in three localities the patches are large and persistent: $0 < y < 100$, around $x=800$ and $x=950$.

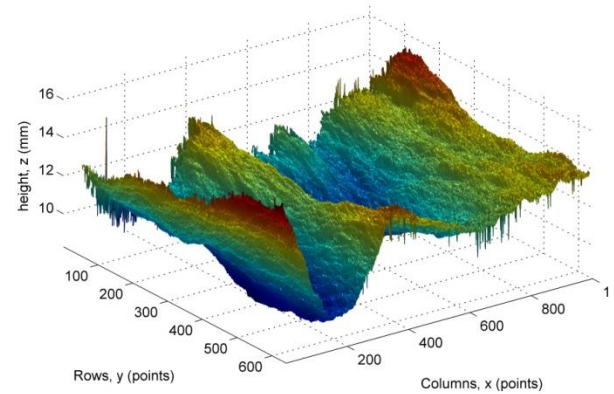


Figure 3.8. Surface matrix with spike errors visible at the edges of the surface matrix. These edges would be later excluded from the data.

Spike errors are points with exaggerated heights (relative to the neighboring points), the occurrence of which is small and limited (Figure 3.8). The spike error has little effect on the roughness of the entire surface because it is localized; however, when analyzing smaller areas in the surface matrix- e.g. damage areas- the spikes can contribute to the local roughness, therefore these errors are eliminated from the data by cutting the raw data matrix into a smaller sub-matrix which excludes the problematic spike zones.

3.4.2 Damage Matrices

Dilation has been shown to occur at confining pressures of up to 800 MPa (Brace et al., 1966). Hence, under the range of normal stress which has been tested in this study, dilation occurs, leading to localized zones of contacts and the observed damage zones. Prior to shear, it is impossible to predict the zones of damage due to shear, therefore each surface must be scanned completely before and after the direct shear experiments. In order to investigate the geometric evolution of the surface roughness it is imperative to examine the damage zones specifically. All the roughness analyses were done on "damage matrices", these are the surface matrices that include only the areas that sustained damage due to shear.

Each surface was scanned entirely by four medium-resolution scanning strips, and partially by two high-resolution scanning strips. Each scanning strip included a pre-shear scan and a post-shear scan for the same area and specific resolution. The damage zones for each

scanning strip matrix were determined by subtracting the post-shear matrix from the pre-shear matrix for the same scanning strip. The undamaged zones provided the reference for the subtraction (Figure 3.13).

$$[\Delta] = [Pre] - [Post] \quad (3.6)$$

Where $[\Delta]$ is the damage matrix, $[Pre]$ and $[Post]$ are the pre and post-shear matrices, respectively.

Zones of damage due to edge effects were cut from the surface matrix and were not included in the analysis. Subsequently, the pre-shear matrix and the post shear matrix were cut into sub-matrices that included only the damage zone solely due to shear. These were termed as "damage matrices" and were used for roughness analysis and wear analysis. Each sample (each experiment) included two surfaces, each with four pre-shear surface matrices and four post-shear matrices (to cover the entire surface area before and after shear), in medium-resolution alone, resulting in an enormous database. Not all scanning strips included damage, therefore it was crucial to find the damage zones from each strip. Roughness evolution analysis was performed on the zones that exhibited greatest damage per surface.

High-resolution scans proved more challenging because these scans covered a much smaller area compared to the medium-resolution scans. Edge effects or undamaged zones rendered the high-resolution scans as useless "garbage" data, therefore only high-resolution scans that included shear damage were examined.

3.4.3 Power Spectral Density Roughness Analysis

Power spectral density (PSD) roughness is the measurement of the strengths of the sinusoidal components of the surface topography as function of the wavelength. Beforehand, the data undergoes a Fourier decomposition (*Brodsky et al., 2011*) which breaks down the surface topography into sines, afterwards the PSD function is invoked. This analysis is one-dimensional, meaning that this process acts in the longitudinal direction or the transverse direction of the scan, hence profiles along the columns or rows of the surface matrix, respectively. The PSD values represented for an entire surface matrix (or surface) are the mean PSD values of all the profiles that compose the surface matrix. These values are retained twice for the same surface: before shearing ("pre-shear") and after shearing ("post-shear"). The pre and post shear values are represented on the same PSD vs. wavelength plot for valuation (Figure 3.9), higher PSD values relate to a rougher surface geometry.

The PSD functions for the laboratory rough surfaces show a distinct form (Figure 3.9):

1. Short wavelength segment: including measurement noise and exhibits a power that differs from self-affine behavior.
2. Medium-long wavelength segment: exhibiting self-affine behavior as a power law.
3. Corner wavelength - dramatic change in the behavior of the PSD function at large wavelengths ($\sim 1 \times 10^1$), this wavelength relates to the length of the whole surface.

The PSD plots in the Results chapter are modified from the plot in Figure 3.9 to exclude the ends of the curves (data at wavelengths greater than 10 mm). PSD results range wavelengths of 0.2 mm to the corner frequency wavelength for the medium-resolution scans, and 0.02-0.2 mm wavelength for the high-resolution scans.

As noted in section 2.2, the PSD roughness is a power-law, which includes the C coefficient and β exponent (eq. (2.3)). These constants are determined by linear fitting to the PSD function in arithmetic scale (by enforcing the logarithm function) using a least squares analysis (Figure 3.10). Therefore, β is the linear slope and $\log(C)$ is the intercept. The Hurst exponent is then calculated as it relates to β in eq. (2.4).

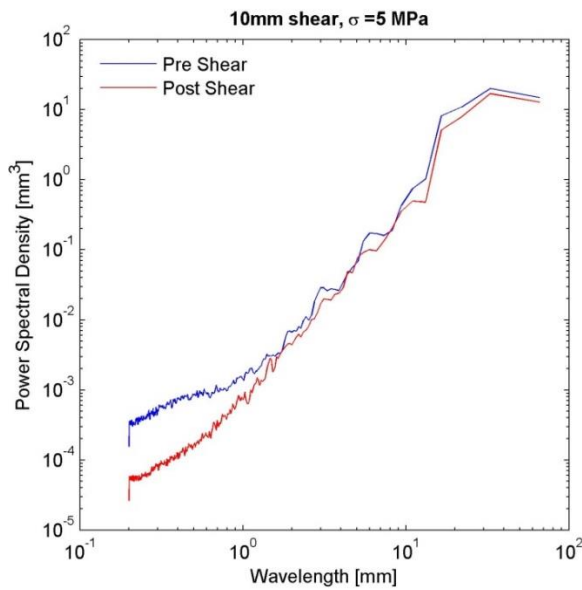


Figure 3.9. Example for a PSD results plot from data scanned by the 75 mm lens. The blue and red lines represents the PSD results for the surface before shearing and after shearing, respectively. The PSD values before and after shearing display minor smoothing at most scales after 10 mm shear under a normal stress of 5 MPa. Note the difference and the data "noise" in the shorter wavelengths ($\sim 3 \times 10^{-1}$ mm) and the corner wavelength at $\sim 2 \times 10^1$ mm.

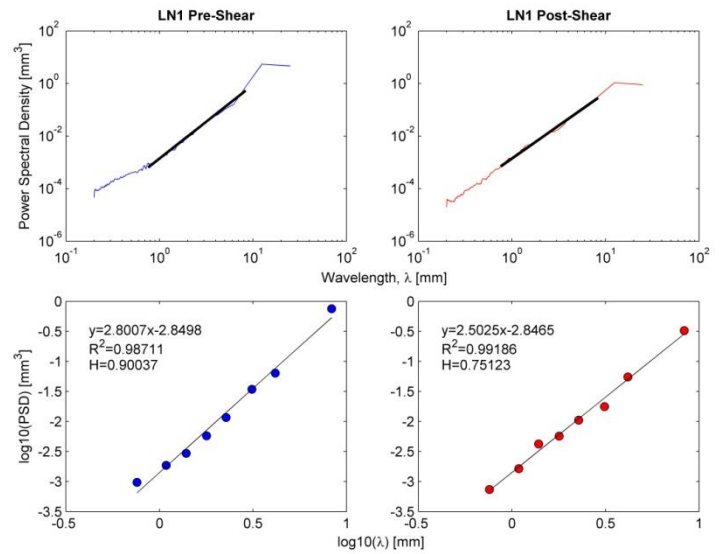


Figure 3.10. Example for a linear fitting plot. The upper plots are the PSD results plot for the pre and post-shear surfaces, the black line represents the data range used for the linear fitting. The bottom plots are the linear fitting plots in arithmetic scale, the red dots are the PSD values, the black solid line is the linear fitting, the linear equation, R-squared value and calculated Hurst exponent are marked in the upper left corner of each plot.

3.4.4 Root Mean Square (RMS) Roughness Analysis

Root mean square (abbreviated RMS) roughness is the measurement of the deviation of a profile (with certain geometry) from a flat, smooth uniform profile. The RMS roughness (h)

of a profile $z(x)$ over a segment of length L is related to the power spectral density (in terms of frequency $k - p(k)$) by Parseval's theorem:

$$h = \left[\frac{1}{L} \int_0^L z^2(x) dx \right]^{\frac{1}{2}} = \left[\int_{1/L}^{\infty} p(k) dk \right]^{\frac{1}{2}} \quad (3.7)$$

Following *Sagy et al. (2007)*, for a profile with self-affine geometry ($1 < \beta < 3$) and length L , substituting equation (2.3) into equation (3.7) and integrating over the wavelength λ , derives the numeric RMS:

$$RMS = [C/(\beta - 1)]^{0.5} L^{(\beta-1)/2} = K \lambda^{\zeta} \quad (3.8)$$

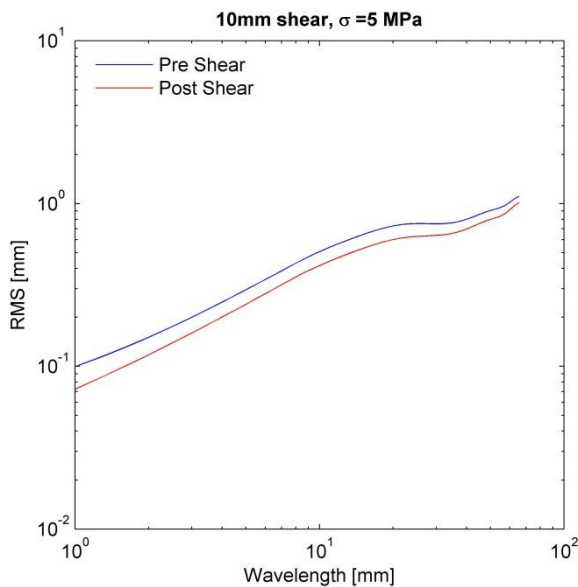


Figure 3.11. Example of the RMS roughness vs. wavelength. The blue and red lines represent the surface data before and after shearing, respectively. The difference of the RMS values before and after shearing is clear, displaying surface smoothing at all scales after 10 mm shear under a normal stress of 5 MPa. Note that at a wavelength of ~20 mm the RMS differs from a power law form.

As with the PSD roughness analysis, the RMS is a one-dimensional analysis of a profile. This analysis is performed on the rows of the input surface matrix. The RMS roughness value for the entire matrix (or surface) is the mean RMS value of all the profiles that compose the surface matrix (or surface). The RMS roughness analyses is conducted on the surface before and after shearing and plotted together for valuation (Figure 3.11). Change in the RMS value before and after shearing is attributed to a change in the surface roughness; higher RMS values relate to a rougher surface (greater deviation from a planar surface for the specific wavelength), whereas lower RMS values relate to a smoother surface.

The RMS curves for the experimental surfaces, display a power-law form at all scales up to wavelengths of a magnitude close (or the same) as the length of the analyzed surface scan - in this study ~10 mm.

3.4.5 Roughness Evolution Analysis

The roughness evolution analysis is done by the roughness data acquired by the PSD and RMS analyses using PSD and RMS ratios according to equations (3.9) and (3.10), respectively:

$$R_{PSD} = \frac{p(\lambda)_{post}}{p(\lambda)_{pre}} \quad (3.9)$$

$$R_{RMS} = \frac{h(\lambda)_{post}}{h(\lambda)_{pre}} \quad (3.10)$$

Where the subscripts “post” and “pre” relate to post shearing and pre shearing, respectively. PSD and RMS data, in terms of wavelength (λ), are referred to as $p(\lambda)$ and $h(\lambda)$, respectively.

The PSD and RMS ratios allow two separate means of measuring the change in roughness due to shearing, the ratios are wavelengths dependent (corresponding with the PSD and RMS) and are calculated per a given wavelength.

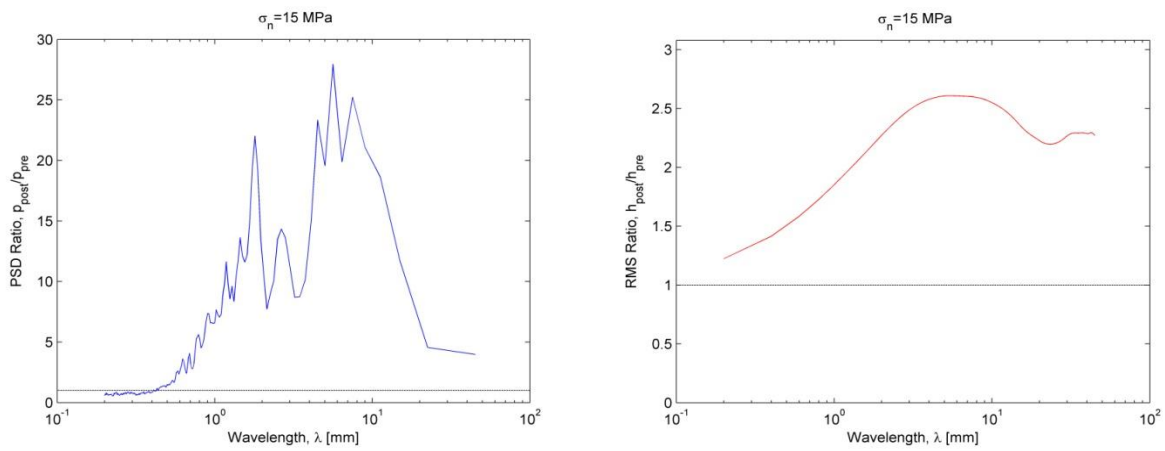


Figure 3.12. Roughness evolution plots: Left – PSD ratio as a function of wavelength. Right – RMS ratio as a function of wavelength. Notice that for wavelengths greater than 1 mm the surface roughness, the drop in the ratios at long wavelengths is attributed to the corner wavelengths and is neglected.

The PSD and RMS ratios data are represented more generally by averaging wavelengths. This generalization averages four wavelength groups: (1) $0.06 < \lambda < 0.4$ mm wavelengths – from the high-resolution scans; (2) $0.4 < \lambda < 1$ mm wavelength; (3) $1 < \lambda < 7$ mm wavelengths; (4) $\lambda > 7$ mm wavelengths. Wavelength groups (2)-(4) are done on data from medium resolution scans.

3.4.6 Wear analysis

Wear analysis was performed by optical means utilizing the scanned data for this measurement. The analysis was done solely on the damage zones, scanned in medium-resolution, by calculating the height difference between each compatible point in the pre-shear and post shear damage matrices. Each point in the damage matrices represents a unit cell area of 0.1×0.0291 mm² (corresponding to the resolution of the scan in both transverse and longitudinal directions), thus for each point the wear volume was calculated by multiplying the unit cell area by the height of the specific point. A threshold height difference was set to 0.5 mm in order to minimize height difference incompatibility of the pre and post shear

matrices. The wear volume was normalized by the area of the whole damage matrix (or damage zone):

$$h_{wear} = \frac{\sum V_{ij}}{nA} \quad (3.11)$$

Where $\sum V_{ij}$ is the sum of wear volume from all the cells in matrix (above threshold value), n is the number of cells in the entire matrix and A is the unit cell area.

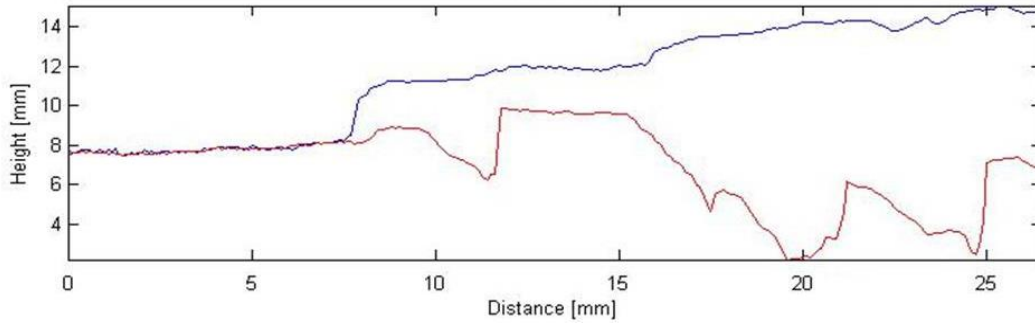


Figure 3.13. Height difference between a profile in the pre-shear matrix (blue line) and the same profile in the post shear matrix (red line). The heights of the matrices is adjusted according to the non-damage zone (at a distance of 0-7 mm) which acts as a reference. The damage zone is clearly visible at a distance of >7 mm from the start of the profile. The wear volume is calculated for each increment along the profile with a height difference of 0.5 mm or more (according to the threshold).

3.5 Mechanical properties of the tested limestone

The rock material used to produce the tested surfaces was a fine-grained limestone from the top Judea Group of central Israel, known by its commercial name “Hebron Marble”. Rough surfaces from this rock type were tested before by *Davidenko (2013)* who characterized the mechanical and physical properties of this limestone at the rock mechanics laboratory at Ben-Gurion University. These properties are summarized in the following table:

Table 3.2. Physical and mechanical properties of tested limestone

	Property Name	Value	Test Type
Physical Properties	Average Grain Diameter	0.4 mm	thin section
	Dry Bulk Density	2565 kg/m ³	-
	Porosity	5.04%	-
Dynamic Mechanical Properties	Young's Modulus	69.089 GPa	
	Bulk Modulus	52.454 GPa	ultra-sonic
	Shear Modulus	27.696 GPa	velocity tests
	Poisson's Ratio	0.28	
Static Mechanical Properties	Young's Modulus	56.983 GPa	uniaxial
	Poisson's Ratio	0.29	compression
	Tensile Strength	5.685 MPa	Brazillian

4 Results

4.1 Direct Shear Tests

The results of six direct shear tests are presented in this section. The tests were performed on rough limestone surfaces that sheared to a constant distance of 10 mm at a velocity of 0.05 mm/s under various normal loads. All of the test parameters are summarized in Table 4.1:

Table 4.1. Direct shear test parameters

Sample	Normal Stress, σ_n [MPa]	Sliding Distance [mm]	Nominal Area [mm ²]	Sliding Velocity [mm/s]
LN1	5	10	117×82	0.05
LN10	7.5	10	109×79	0.05
LN6	10	10	107×80	0.05
LN11	12.5	10	114×77	0.05
LN5	15	10	107×80	0.05
LN7	15	10	103×81	0.05

The direct shear tests yielded three types of results: (1) shear stress; (2) coefficient of friction; and (3) shear and normal stiffness.

4.1.1 Shear Stress-Displacement Results

The following plots (Figure 4.1-Figure 4.6) display shear stress (τ) in blue and dilation (Δv) in red vs. shear displacement (Δu). Note that here dilation is defined as positive while contraction is negative.

Before testing, the surfaces are set in a mating configuration. Thereafter, the normal loading segment ends when the target normal stress is achieved and then the shear segment begins. Once shear displacement starts, shear stress builds up across the surface, causing the interface to contract and shear displacement to initiate. The shear stress continues to increase until it reaches a peak value (τ_{peak}) after a few millimeters of displacement (2-6 mm). This stage is characterized by an initial linear shear stress-displacement curve behavior in the first millimeter of displacement, which afterwards changes to non-linear behavior with small jumps in the stress, which might relate to failure of minor asperities. Upon reaching peak value, the shear stress begins to drop with increasing displacement and stabilizes at a near-constant value, referred to as the residual stress (τ_{res}). The shear stress drop ($\Delta\tau$), referred also

as stress drop, is defined as the difference between the peak shear stress and the residual shear stress as follows:

$$\Delta\tau = \tau_{peak} - \tau_{res} \tag{4.1}$$

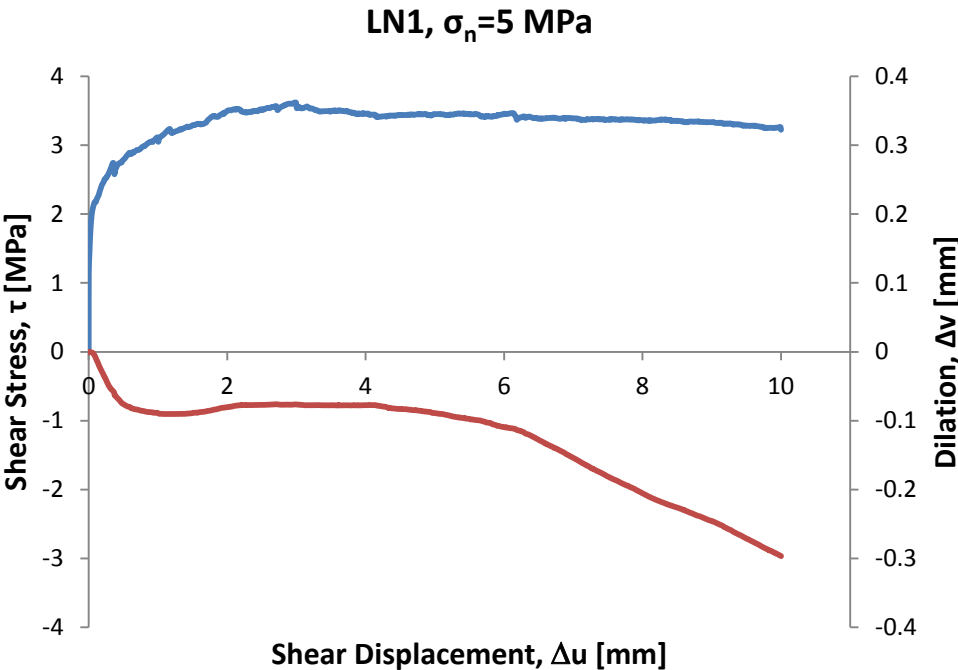


Figure 4.1. Variations of shear stress (blue) and dilation (red) with shear displacement of mating limestone surfaces sheared to a distance of 10 mm under a normal stress of 5 MPa.

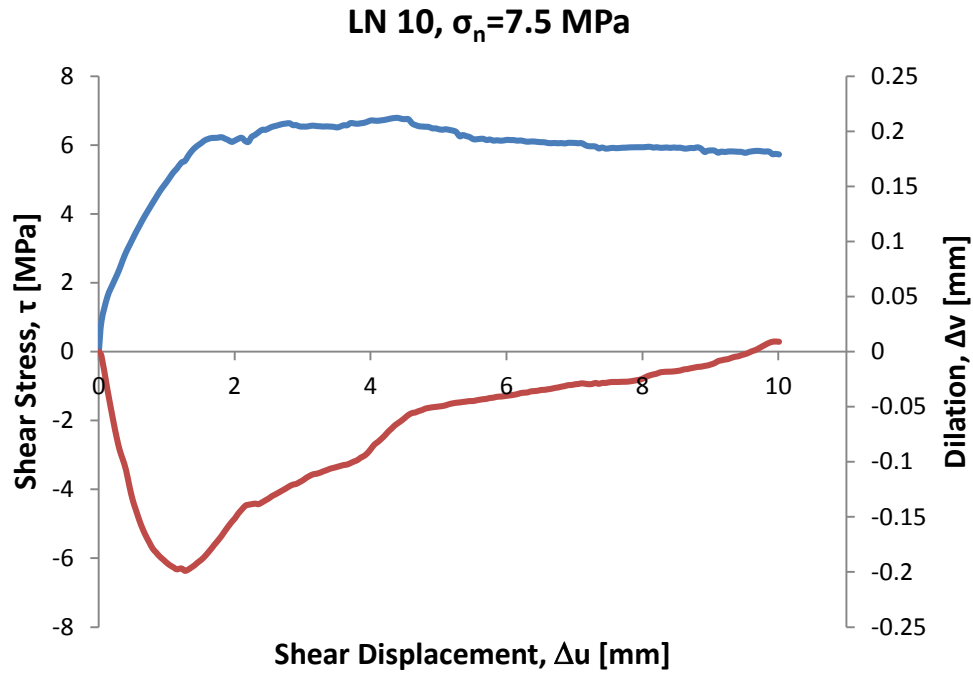


Figure 4.2. Variations of shear stress (blue) and dilation (red) with shear displacement of mating limestone surfaces sheared to a distance of 10 mm under a normal stress of 7.5 MPa.

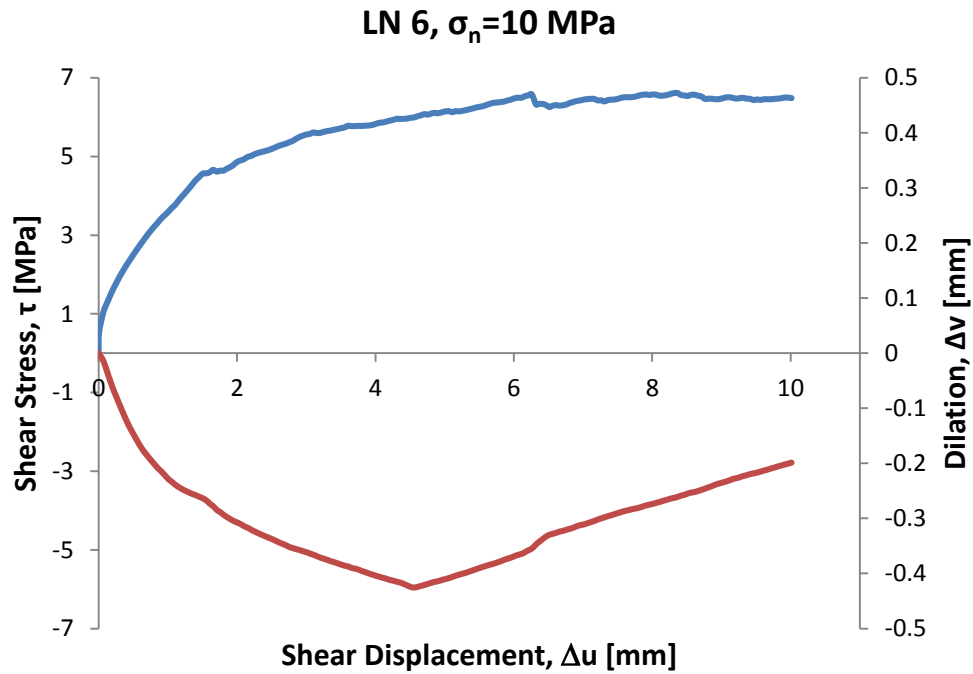


Figure 4.3. Variations of shear stress (blue) and dilation (red) with shear displacement of mating limestone surfaces sheared to a distance of 10 mm under a normal stress of 10 MPa.

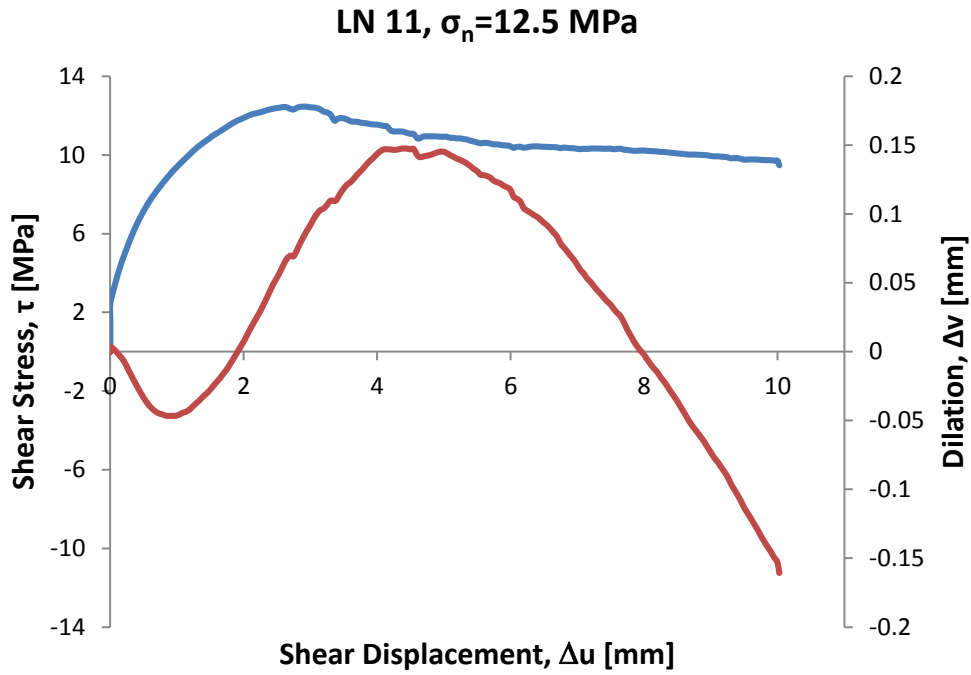


Figure 4.4. Variations of shear stress (blue) and dilation (red) with shear displacement of mating limestone surfaces sheared to a distance of 10 mm under a normal stress of 12.5 MPa.

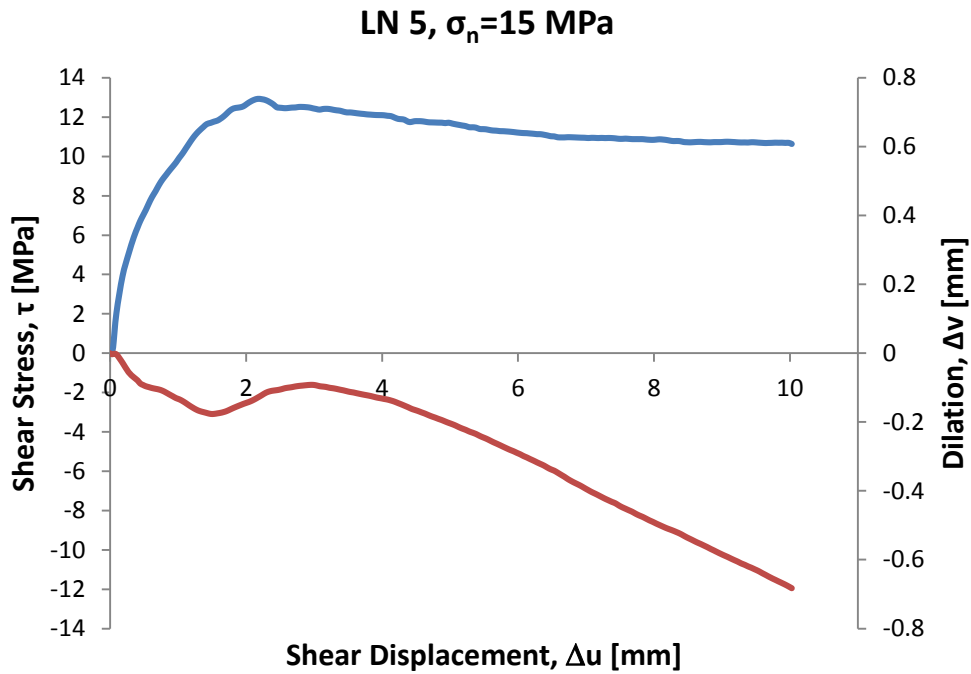


Figure 4.5. Variations of shear stress (blue) and dilation (red) with shear displacement of mating limestone surfaces sheared to a distance of 10 mm under a normal stress of 15 MPa.

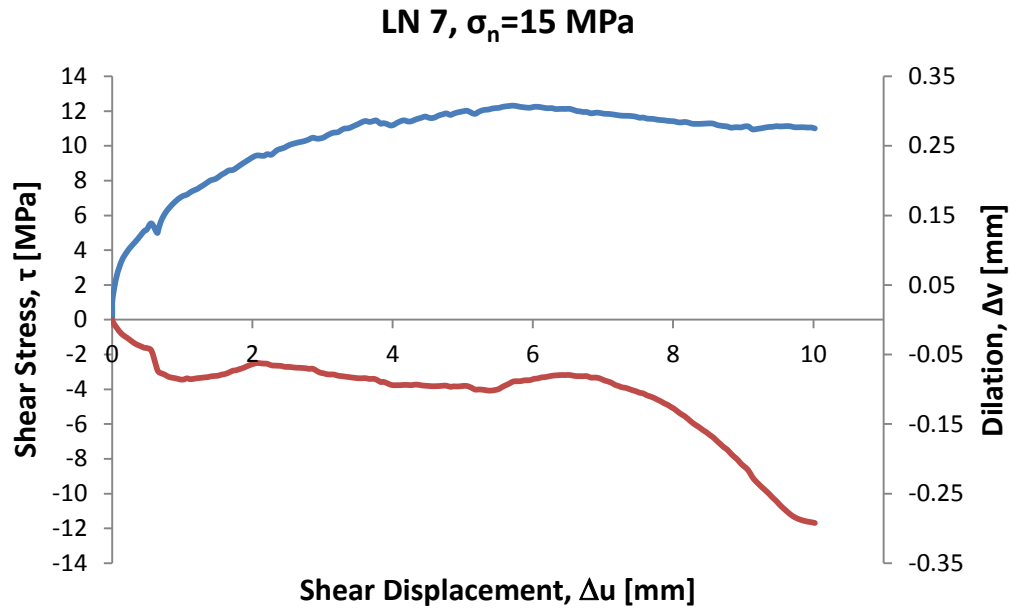


Figure 4.6. Variations of shear stress (blue) and dilation (red) with shear displacement of mating limestone surfaces sheared to a distance of 10 mm under a normal stress of 15 MPa.

The shear stress results from all of the experiments are summarized in Table 4.2:

Table 4.2. Shear stress results

Sample	Normal Stress [MPa]	Peak Shear Stress [MPa]	Residual Shear Stress [MPa]	Stress Drop, $\Delta\tau$ [MPa]
LN1	5	3.622	3.253	0.369
LN10	7.5	6.787	5.798	0.989
LN6	10	6.61	6.468	0.142
LN11	12.5	12.458	9.785	2.673
LN5	15	12.93	10.707	2.223
LN7	15	12.312	11.064	1.248

The highest shear stress was measured for sample LN5, sheared under a normal stress of 15 MPa. The lowest shear stress was measured for sample LN1, sheared under a normal stress of 5 MPa. The peak and residual shear stress results correlate with an increase of normal stress (Table 4.2). The shear stress difference results exhibit fluctuations; the maximum value was measured for sample LN11, sheared under normal stress of 12.5 MPa. The minimum value was measured for sample LN6, sheared under a normal stress of 10 MPa.

The direct shear test results (Figure 4.1-4.6) exhibit a complex dilation-displacement behavior. The dilation-displacement curves of all of the experiments indicate phases of contraction and dilation. Contraction is related to the elastic interlocking of the asperities and

occurs in the initial shear segment of all of the experiments. Another contraction region is measured in all experiments, except LN6 and LN10, when the shear stress drops from peak to residual values. Dilation is related to the riding-up (gliding) mechanism where asperities climb over each other during shear sliding. The dilatational behavior of the dilation-displacement curve occurs at all experiments after initial contraction. The dilation commences before peak shear stress conditions are achieved, suggesting that the asperities undergo some amount of displacement through the riding-up mechanism before failing.

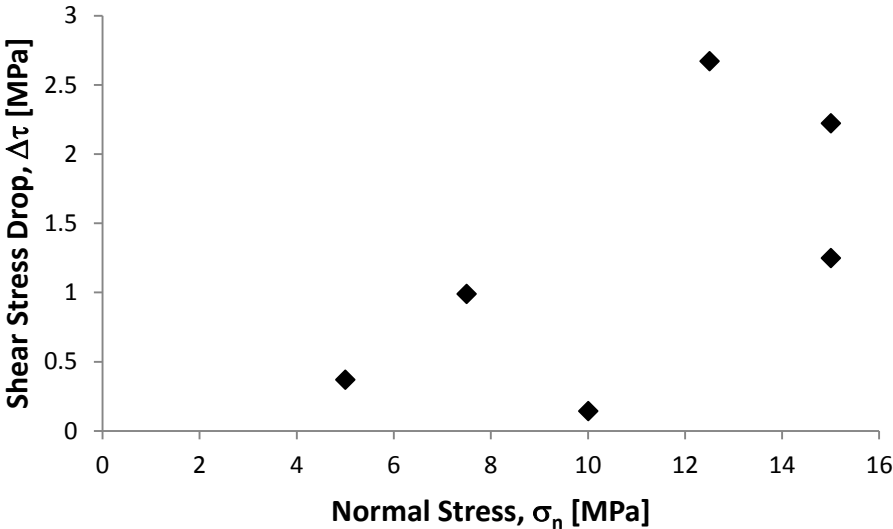


Figure 4.7. Variations of the shear stress drop with the applied normal stress. Note the outlier at (10,0.142) which refers to data from experiment LN6 where anomolous low friction was measured.

4.1.1.1 *Coulomb Strength Criterion for Rough Limestone Surfaces*

The Coulomb strength criterion was calculated for the rough limestone surfaces. The peak and residual shear strength data from each experiment were plotted in shear stress-normal stress space and fitted to a linear curve using least squares analysis in MS Excel tool (Figure 4.8).

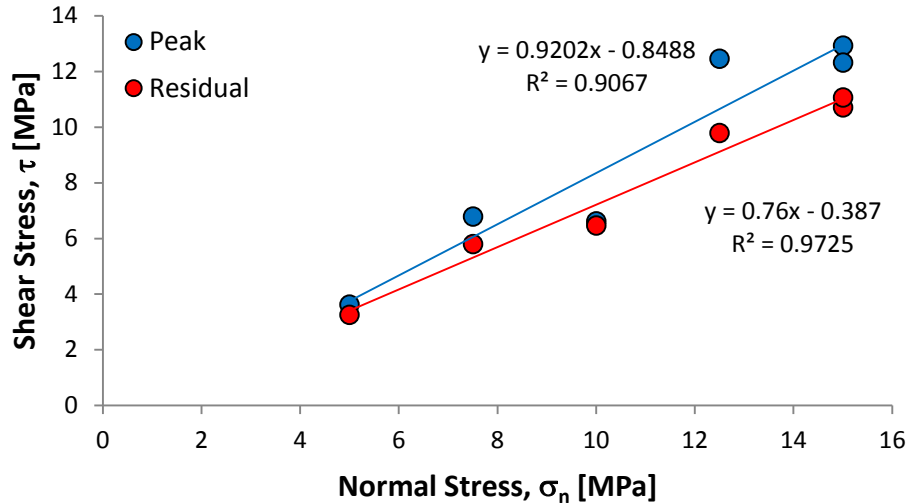


Figure 4.8. Coulomb strength criterion for the rough limestone surfaces. Blue points represent peak shear stress values for each experiment while the red points represent residual stress values of the same experiments. The Blue and red lines are the least squares linear fitting of the blue and red data sets, respectively. The lines correspond to the Coulomb strength criterion.

The results plotted in Figure 4.8 suggest that the Coulomb-Mohr criterion is valid for the tested interfaces, with the following friction angles:

$$\phi_{peak} = 42.62^\circ$$

$$\phi_{residual} = 37.24^\circ$$

4.1.2 Friction Results

The friction was calculated from the shear and normal stresses data for each experiment as the stress ratio, τ/σ_n (Figure 4.9). Direct shear tests exhibit two zones of different frictional behaviors: (1) pre-peak shear stress zone; and (2) post-peak shear stress zone. The displacement is characterized by vertical contraction of the interface and a constant increase in shear stress until it reaches its peak value where maximum friction is measured (μ_{peak}). Upon reaching peak shear stress, the rock interface usually experiences a stress drop, which decreases the shear stress.

The friction was computed for each experiment using the normal and shear stress measurements throughout the displacement and the results are shown in Figure 4.9. The maximum values of the friction were related to the peak stress ratio, thus termed peak friction coefficient. The residual friction coefficient was calculated by averaging the tail of the stress ratio/displacement curve for displacements ranging from 8-10 mm. This was done because the post-peak shear stress continued to gradually decrease with an increase in displacement never

reaching a constant value. The peak and residual friction coefficients are plotted in Figure 4.10 and shown in Table 4.3.

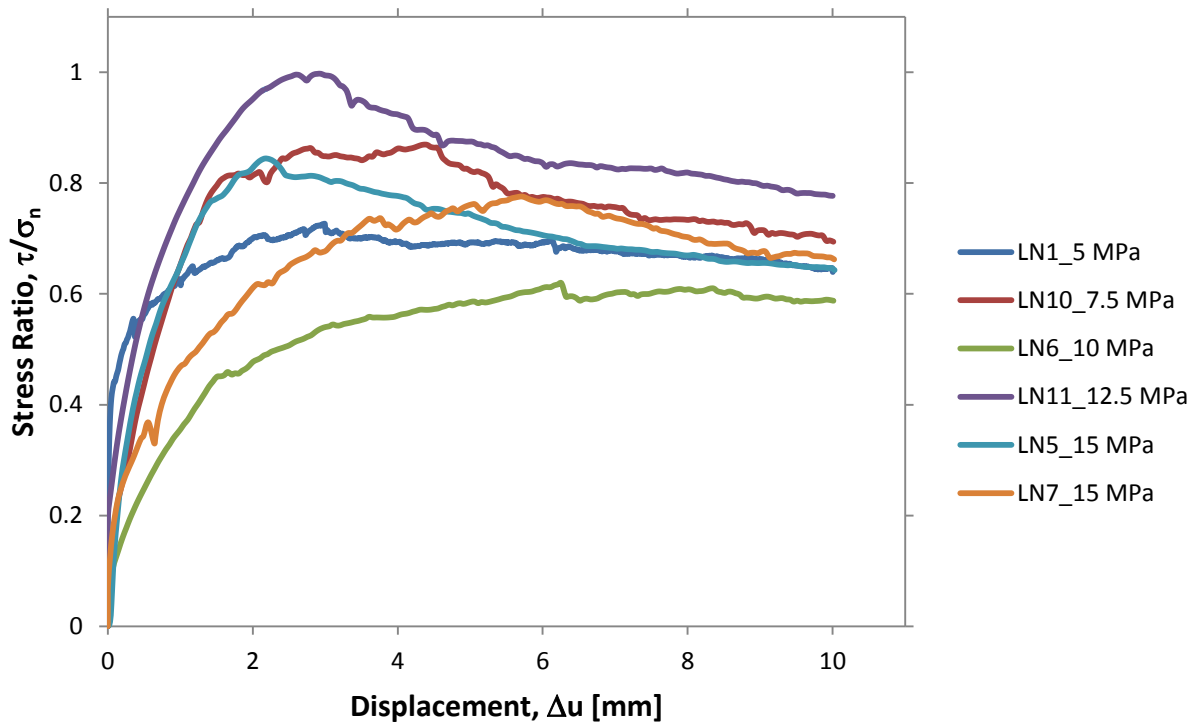


Figure 4.9. Variations of the stress ratio (τ/σ_n) with displacement (Δu) for rough surfaces under different normal stresses.

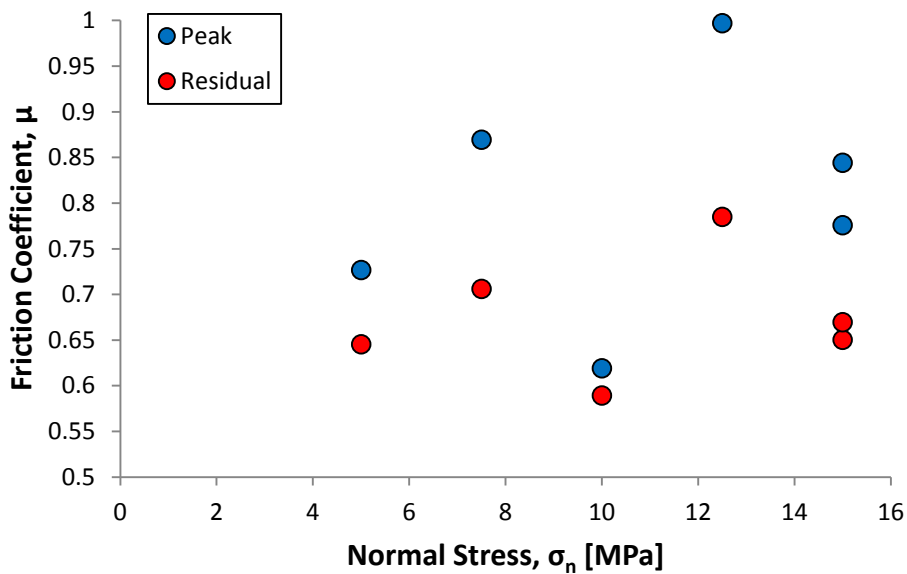


Figure 4.10. Variations of the peak (blue) and residual (red) friction coefficient with normal stress. Each peak and residual pair of points refers to the same experiment.

Table 4.3. Friction results for direct shear experiments.

Sample	Normal Stress [MPa]	Coefficient of Friction	
		μ_{peak}	μ_{res}
LN1	5	0.724	0.651
LN10	7.5	0.905	0.773
LN6	10	0.661	0.647
LN11	12.5	0.997	0.783
LN5	15	0.862	0.714
LN7	15	0.821	0.738

When plotting the variations of the stress ratio (τ/σ_n) with the displacement (Figure 4.9) the differences between the experiments are illustrated more clearly. μ_{peak} does not necessarily rise with normal stress. The highest value of the friction coefficient (both peak and residual) was measured for sample LN11, where the normal load was 12.5 MPa. The lowest value was measured for the LN6 sample, where the normal load was 10 MPa. This inconsistency is clearly visible when plotting the peak and residual friction coefficient against the normal stress (Figure 4.10). All of the experiments displayed a stress drop, which relates to the transition between the peak conditions and residual conditions. However, sample LN6 ($\sigma_n=10$ MPa) experienced the smallest stress drop (Figure 4.7), resulting in minor difference between the peak and the residual friction coefficients.

4.1.3 Shear and Normal Stiffness Results

Two types of stiffness were analyzed; shear stiffness (k_s) and normal stiffness (k_n). The shear stiffness was computed directly from the linear segment of the shear stress-displacement curves (section 4.1.1). This value denotes the rock interfaces' resistance to shearing. The normal stiffness is determined via the dilation-contraction measurements (from the vertical LVDTs) during the normal loading segment of the shear experiment. The normal stiffness scales the rocks surfaces' resistance to contraction whereas the shear stiffness scales the rocks resistance to shearing. Both types of stiffness values are expressed in MPa/mm units and plotted against the normal stress in Figure 4.11.

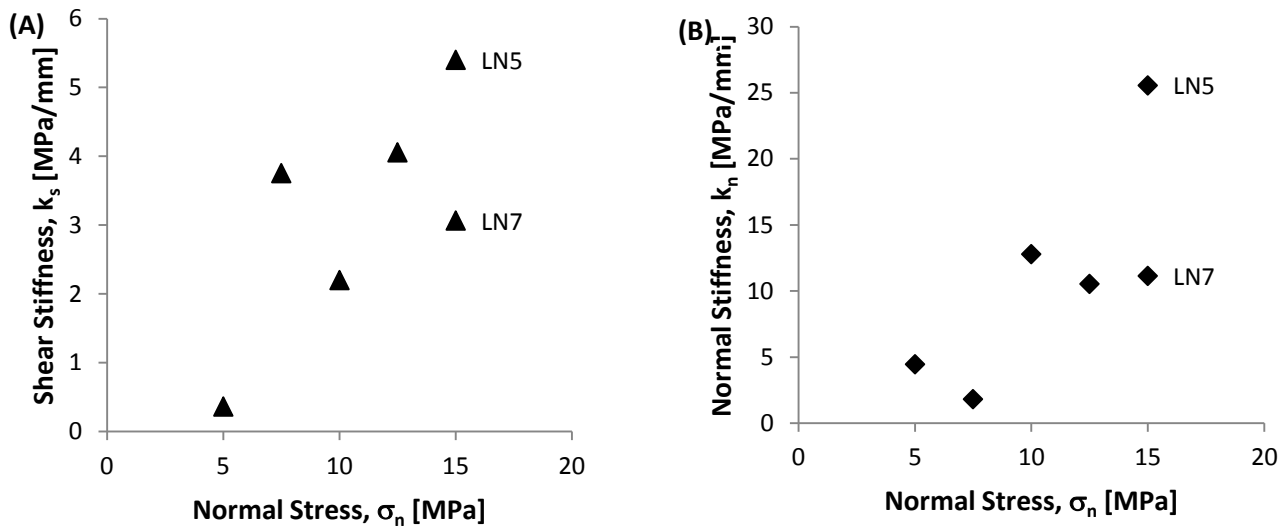


Figure 4.11. (A) Shear stiffness vs. normal stress results. (B) Normal stiffness vs. normal stress results. Labels for each experiment are attached to the two the values at normal stress of 15 MPa.

Both the shear and normal stiffness show an overall trend of an increase with normal stress. Minimal values were measured for the low normal stresses (5-7.5 MPa), where the highest values were measured for the highest normal stresses (15 MPa). Some minor exceptions are evident from the data though. Low values of shear stiffness were measured for the $\sigma_n=10$ and 15 MPa experiments (samples LN6 and LN7, respectively). Low values were also measured for normal stiffness at experiments loaded by 12.5 and 15 MPa, relating to samples LN11 and LN7, respectively.

4.2 Roughness evolution results

During frictional sliding the surface roughness changes constantly, therefore measuring the roughness simultaneously is impossible. Instead, roughness is measured before and after shearing. As described in chapter 3, the roughness evolution is quantified by comparing the pre and post-shear measurements.

Two methods were used to measure surface roughness: power spectral density (PSD) and root mean square (RMS). Both methods were applied to surface profiles parallel to slip orientation (see details in chapter 3). The roughness data from each method were utilized to assess the roughness evolution by PSD and RMS ratios (with respect to each method).

Roughness evolution analysis (sections 4.2.1 and 4.2.2) was performed on selected “damage zones”. These zones were identified as localities that suffered maximum damage during shearing. In section 4.2.4, the RMS ratios were used to compare roughness evolution between mating areas (top surface vs. bottom surface). Because this type of analysis was done on two separate (though mating) surface areas, zones of relative mild to no damage were

included along with damage zones. The top vs. bottom analysis was done using the RMS method exclusively.

4.2.1 Roughness Evolution in Damage Zones

Damage zones were recognized by comparing scanned data of the same surface area before and after shearing. The heights of the data (from the pre and post-shear scans of the same area) had to be adjusted for a meaningful comparison. This was done artificially by calibrating the heights of one surface matrix according to the heights of undamaged zones (in the post-shear matrix), which acted as a reference. The heights of one matrix were adjusted mathematically by adding a factor so that undamaged zones matched precisely. When subtracting the pre-shear matrix from the post-shear matrix, the damage zones become clearly visible in a matrix referred to as the “damage matrix” (section 4.2.2). Zones with expensive damage were selected for the analysis performed in this section.

Table 4.4 summarizes the properties of the damage matrices used for the PSD and RMS roughness analyses. The analyses were performed on the profiles (rows of the matrices) which parallel the slip direction. Each damage matrices covers a nominal surface area.

Table 4.4. Damage zone matrices properties

Sample	Type *	No. of Profiles	Nominal Area [mm ²]
LN1	MR	501	25×14.56
LN10	MR	540	26.5×15.7
LN6	MR	319	53×9.26
	HR	131	3×2.46
LN11	MR	501	69.9×14.56
LN5	MR	387	45.1×11.24
	HR	51	4×0.95
LN7	MR	311	44.9×9.03
	HR	210	23×3.96

* Note: MR refers to medium-resolution scans; HR refers to high-resolution scans.

All the plots include pre-shear roughness data series, colored blue, and post-shear roughness data series, colored red. Where available, the high-resolution data is also included in the plots, always ranging in the shorter wavelengths (0.02-0.2 mm). Because the high-resolution scans cover only a small area of the surface, they do not always include the same scale of damage as the data from the medium-resolution scans (data sets that encompass most of the wavelengths). Moreover, the high-resolution data may be of an area that is not included in the main analyzed damage zones.

4.2.1.1 PSD Roughness Measurements

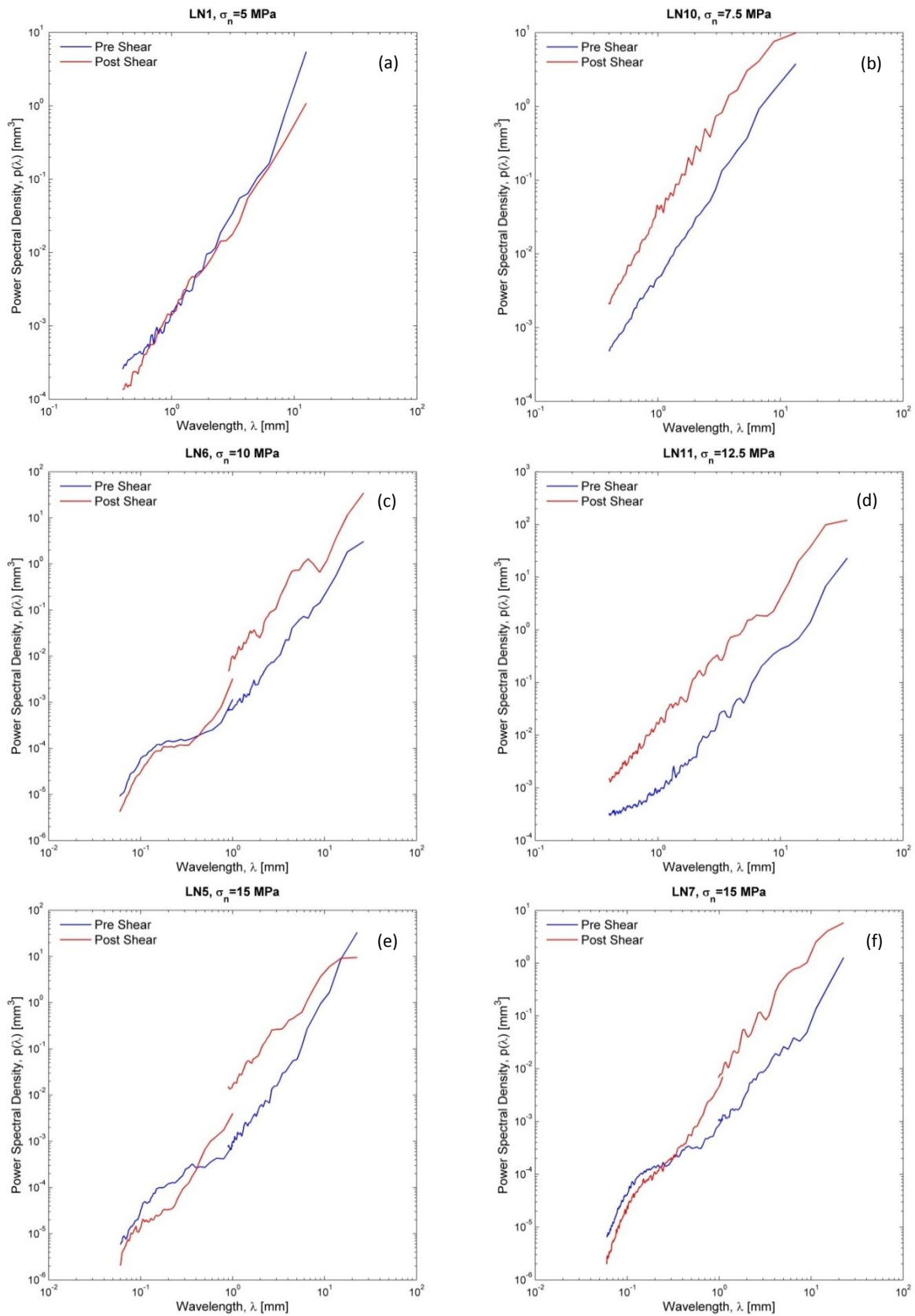


Figure 4.12. Power spectral density vs. wavelength plots for pre-shear (blue) and post-shear (red) roughness. (a) Sample LN1, sheared under a normal stress of 5 MPa. (b) Sample LN10, sheared under a normal stress of 7.5 MPa. (c) Sample LN6, sheared under a normal stress of 10 MPa. (d) Sample LN11, sheared under a normal stress of 12.5 MPa. (e) and (f) Samples LN5 and LN7, respectively, sheared under a normal stress of 15 MPa.

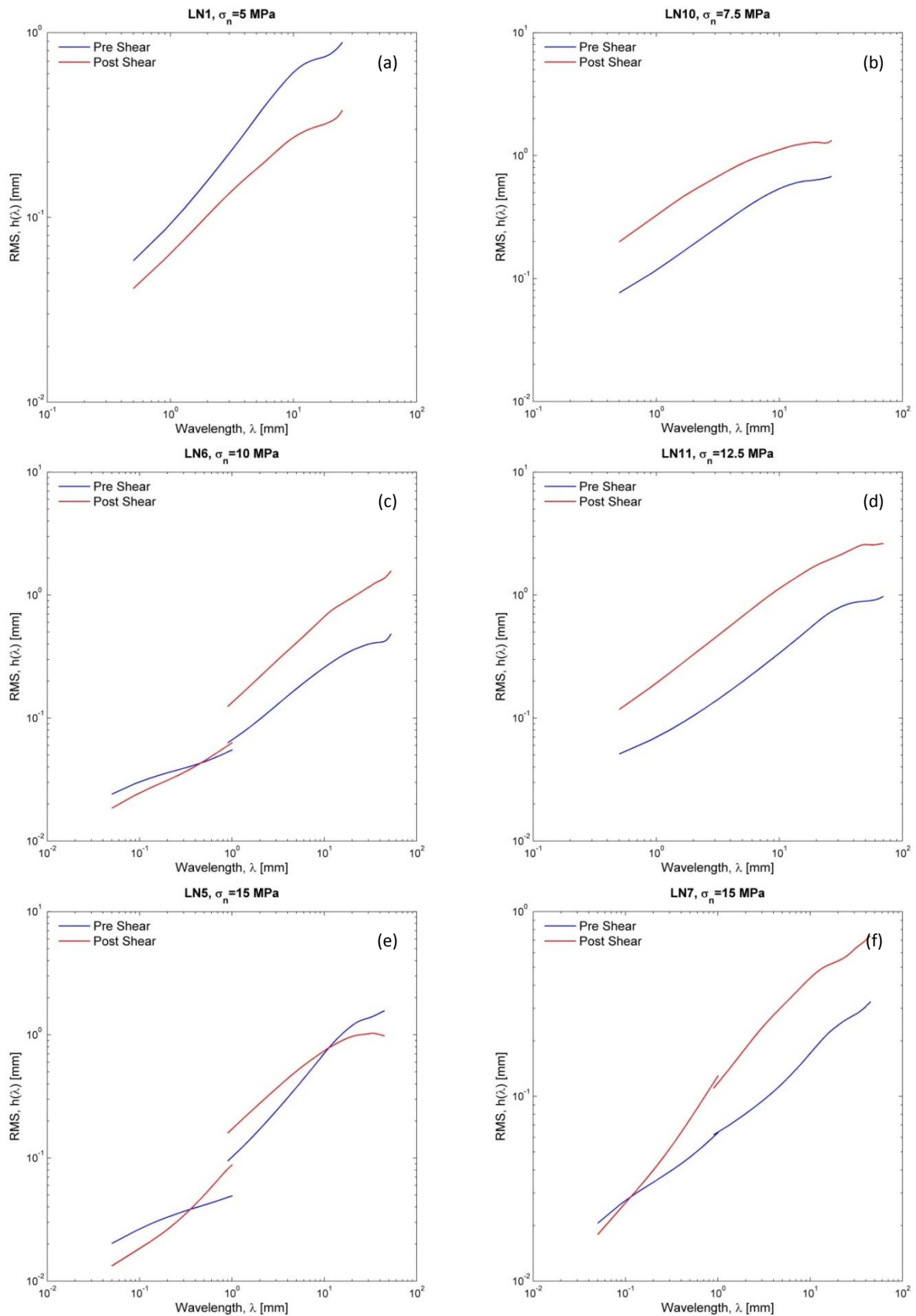
4.2.1.2 *RMS Roughness Measurements*

Figure 4.13. Root mean square vs. wavelength plots for pre-shear (blue) and post-shear (red) roughness. (a) Sample LN1, sheared under a normal stress of 5 MPa. (b) Sample LN10, sheared under a normal stress of 7.5 MPa. (c) Sample LN6, sheared under a normal stress of 10 MPa. (d) Sample LN11, sheared under a normal stress of 12.5 MPa. (e) and (f) Samples LN5 and LN7, respectively, sheared under a normal stress of 15 MPa.

Figure 4.12 and Figure 4.13 display the PSD and RMS roughness results, respectively. As a whole, the roughness results from both methods display the same pre and post-shear trends. At low normal stress (5 MPa), the surface evolved to a smoother, simpler geometry (Figure 4.12a and Figure 4.13a). For surfaces sheared under higher loads (7.5-15 MPa), the surfaces roughness evolved to a more complex geometry by becoming rougher (Figure 4.12 and Figure 4.13 b-f). However, an increase in surface roughness did not occur at all scales. Both PSD and RMS results for the high-resolution scans (Figure 4.12 and Figure 4.13 subplots *c*, *e* and *f*, data ranging wavelengths up to 0.4 mm) display surface smoothing at those wavelengths under normal stresses of 10 and 15 MPa. Moreover, these samples (LN10, LN5 and LN7) all display a "bend" in the PSD vs. wavelength curves (Figure 4.12 subplots *c*, *e* and *f*). The bend occurs around a wavelength of 0.4 mm.

4.2.1.3 *Roughness Evolution – PSD and RMS Ratios*

The pre and post-shear roughness data, from the PSD and the RMS analysis (sections 4.2.1.1 and 4.2.1.2), were used to quantify the roughness evolution by PSD and RMS ratios. The ratios were computed by dividing the post-shear data by the pre-shear data, per wavelength. Thus, ratios greater than 1 indicate surface roughening and vice versa.

The PSD and RMS values were averaged over wavelength ranges (in millimeters): 0.06-0.4 (for high-resolution scans), 0.4-1, 1-7 and greater than 7 for medium-resolution scans. The wavelength averaging ranges were set according to the wavelength ranges where the ratios exhibited stable values (Figure 4.14 and Figure 4.15). The mean ratios values were plotted against the normal stress for each wavelength range category (Figure 4.16 and Figure 4.17).

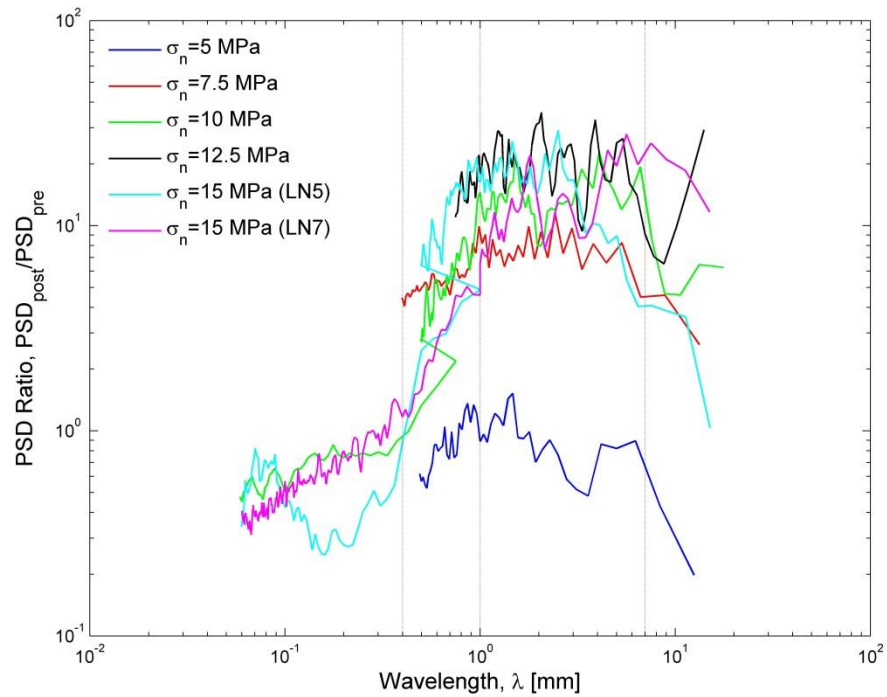


Figure 4.14. Variations of the PSD ratio with wavelength. The plot includes the results from medium-resolution scans of all the experiments. The grey vertical lines display the averaged wavelengths range used in the roughness evolution analysis.

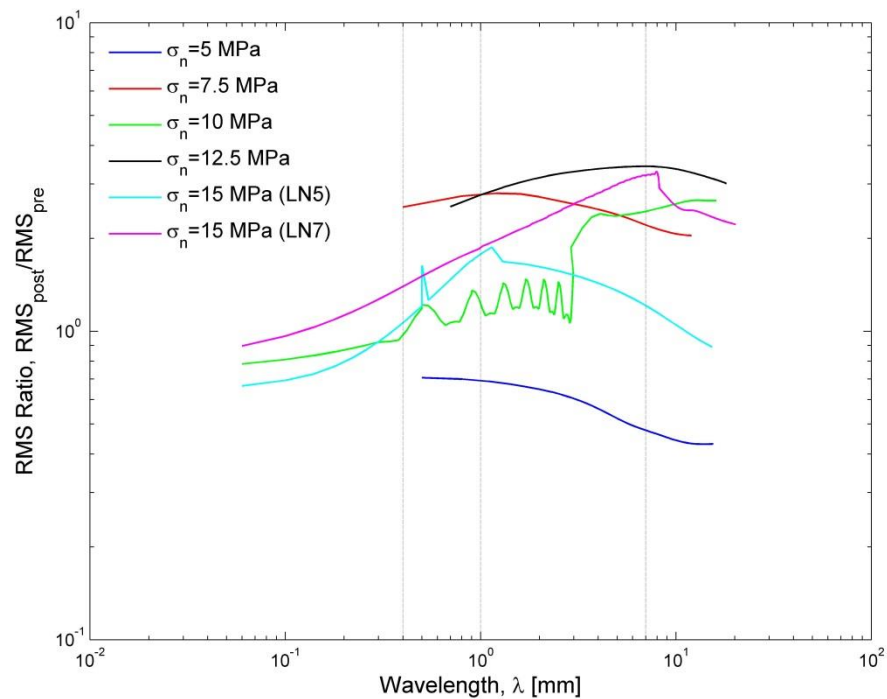


Figure 4.15. Variations of the RMS ratio with wavelength. The plot includes the results from medium-resolution scans of all the experiments. The grey vertical lines display the averaged wavelengths range used in the roughness evolution analysis.

Figure 4.14 displays the variations of the PSD ratio over different wavelengths. This plot was used to determine the limits where PSD ratios remained stable. The limits are plotted as

vertical lines in Figure 4.14. These limits were then used for the RMS ratio data (Figure 4.15) although this data set features less variability along the different wavelengths.

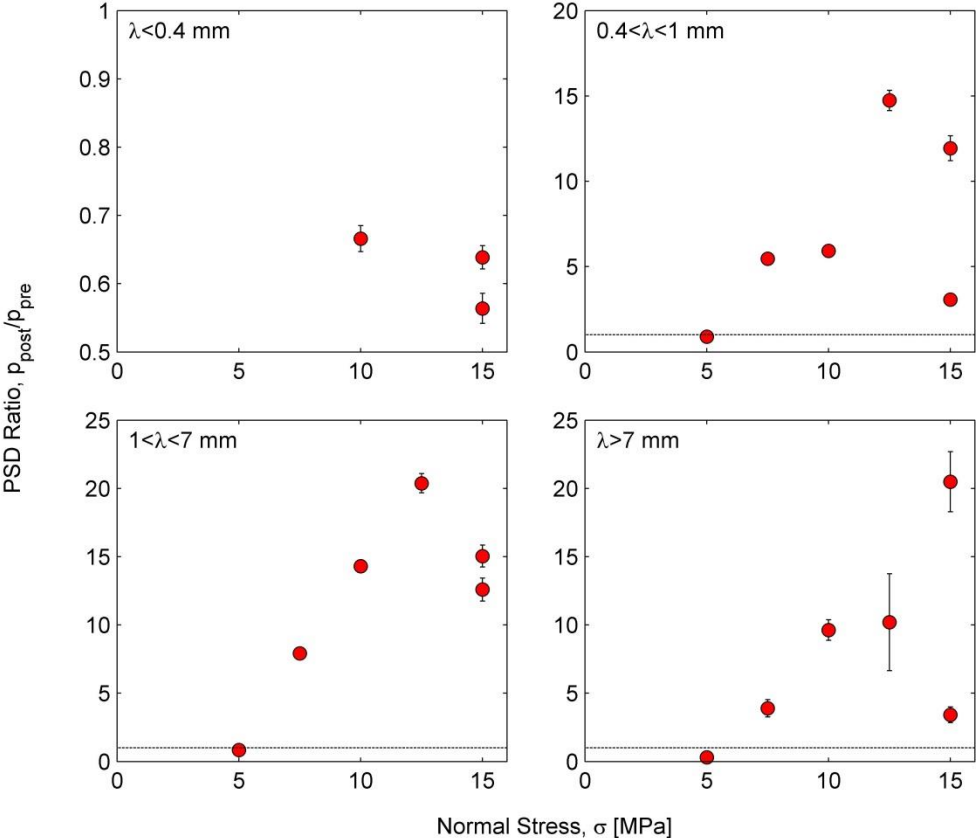


Figure 4.16. Mean PSD ratios for different wavelengths plotted against normal stress. Each frame refers to different wavelength averaging range (λ). The dashed line represents the PSD ratio value of one.

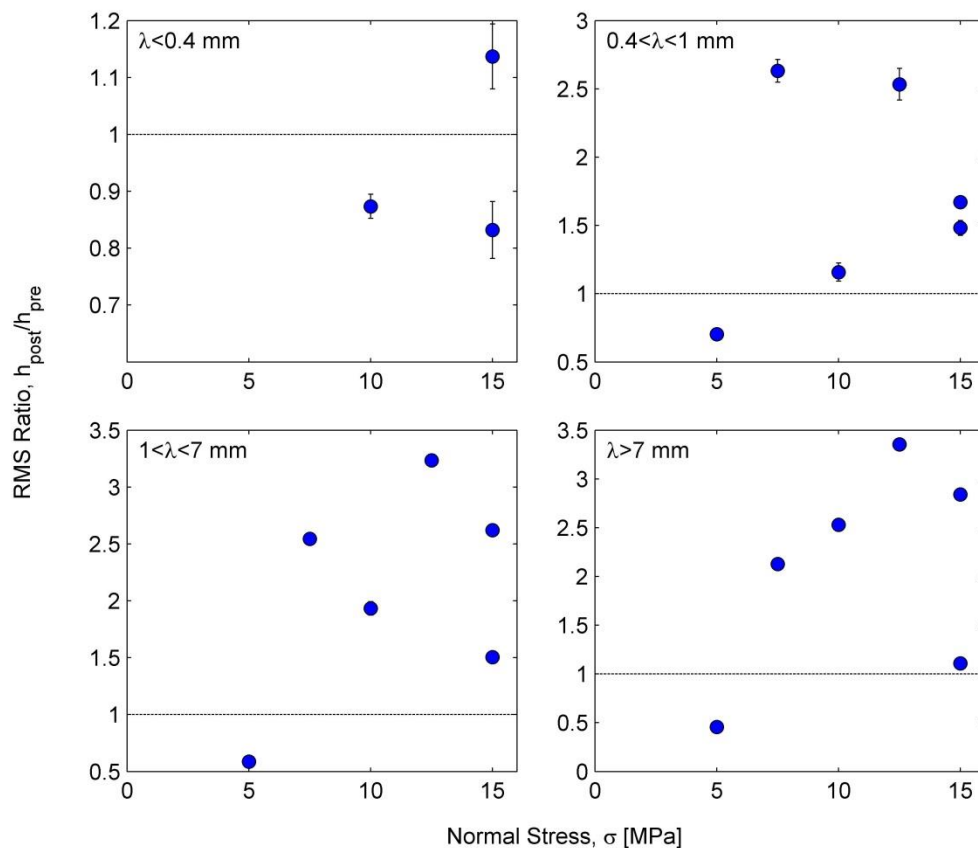


Figure 4.17. Mean RMS ratios for different wavelengths plotted against normal stress. Each frame refers to different wavelength averaging range (λ). The dashed line represents the RMS ratio value of one.

Both the PSD and RMS ratios display surface roughening with increased normal stress for wavelength greater than 0.4 mm. At the shortest wavelengths ($0.06 < \lambda < 0.4$) the PSD and RMS ratios are smaller than one, which correspond with surface smoothing. Increase of roughness values with increased normal stress is measured at the range of 1-7 mm, reaching a maximum at experiment LN11, sheared under 12.5 MPa. For the longest wavelengths (>7 mm) maximum ratio values correlated with the highest loads (12.5-15 MPa). However, between the two 15 MPa experiments the results display some differences. For the smallest wavelength range (0.06-0.4) sample LN5 exhibits smoothing, whereas sample LN7 roughening by both methods. For the medium wavelengths (categories 0.4-1 mm and 1-7 mm) the PSD ratio values are higher for sample LN5, whereas the RMS ratio values are higher for sample LN7. Both methods do correspond in these wavelengths, by indicating surface roughening. At the longest wavelengths (>7 mm) both methods agree, measuring greater surface roughening for sample LN7.

4.2.2 Hurst Exponent Estimation of the Fracture Surfaces

The tested fracture surfaces were analyzed, using the power spectral density (PSD) data, in order to estimate the Hurst exponent (H). A power law was fitted to the data using least-squares analysis in Matlab after enforcing the logarithm (base=10) function to the data. The PSD vs. wavelength data was down-sampled for the short-medium wavelengths (~ 0.4 - 4 mm) because at these wavelengths the PSD function samples more roughness profiles compared to longer roughness profiles (longer wavelengths: >4 mm). This ensured that the least squares analysis would account for each wavelength equally (PSD measurement points were more evenly distributed along the wavelengths). The power of the pre and post-shear PSD data (β) is related directly to the Hurst exponent (H) as explained in the chapter 3. This analysis was performed on medium-resolution scans exclusively.

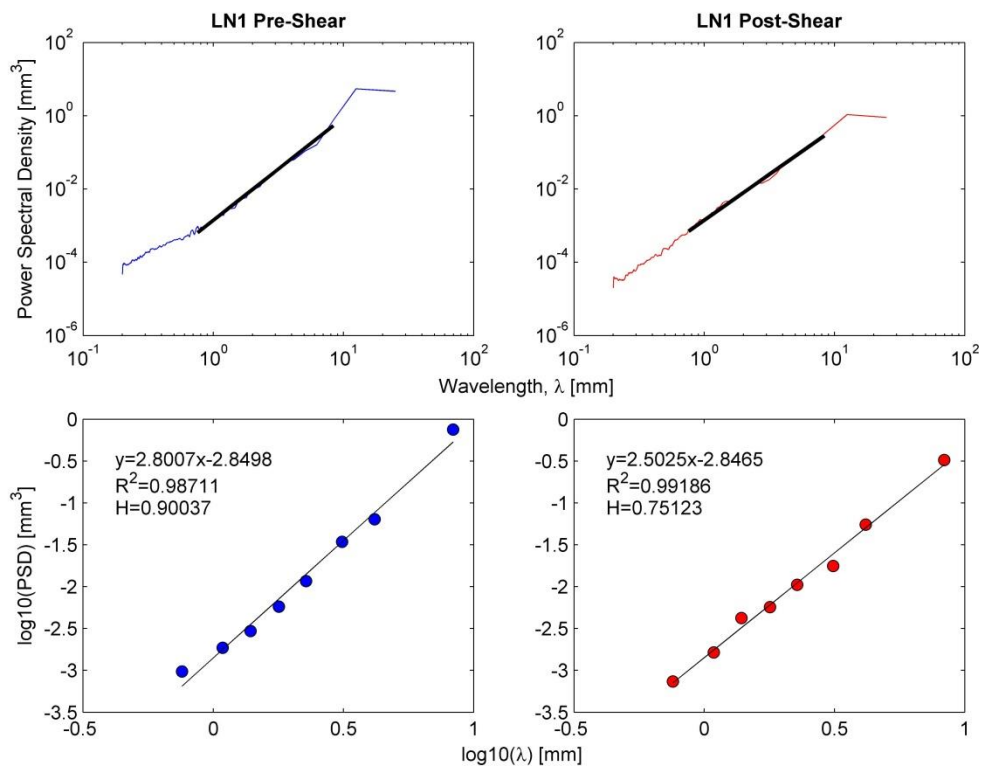


Figure 4.18. Least-squares analysis for sample LN1 ($\sigma_n=5$ MPa), blue color scheme represents the pre-shear data (left frames) and the red color scheme represents the post-shear data (right frames). Top frames represents the actual data with the fitted power law, bottom frames represent the linear fitting in arithmetic space, where H is the calculated Hurst exponent.

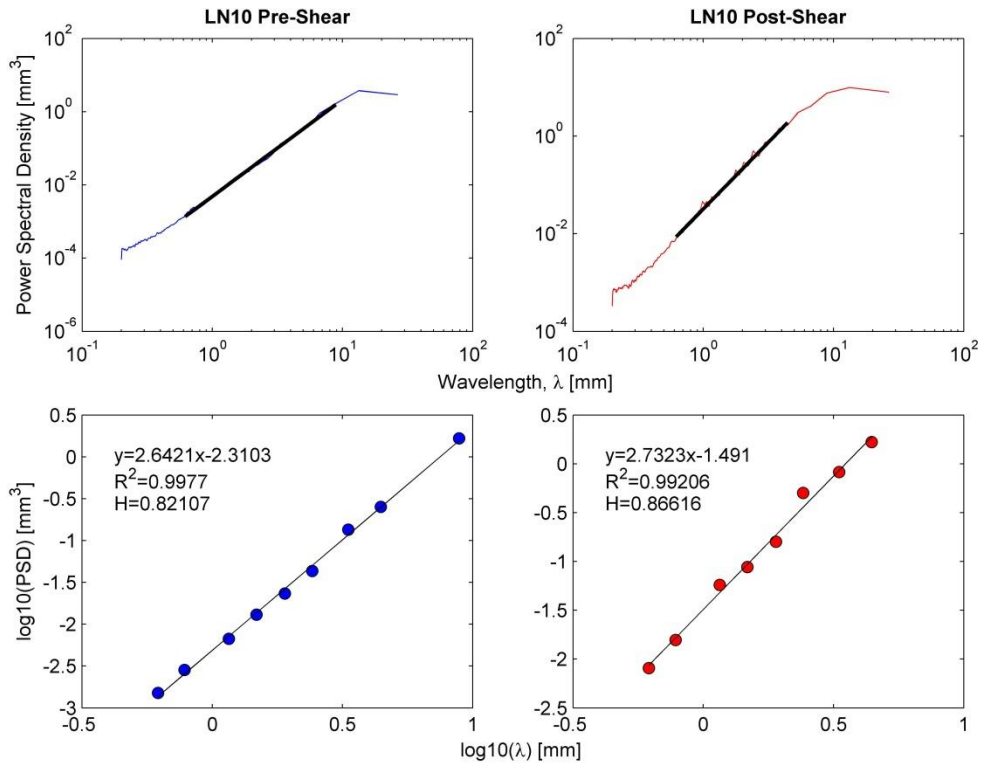


Figure 4.19. Least-squares analysis for sample LN10 ($\sigma_n=7.5$ MPa), blue color scheme represents the pre-shear data (left frames) and the red color scheme represents the post-shear data (right frames). Top frames represents the actual data with the fitted power law, bottom frames represent the linear fitting in arithmetic space, where H is the calculated Hurst exponent.

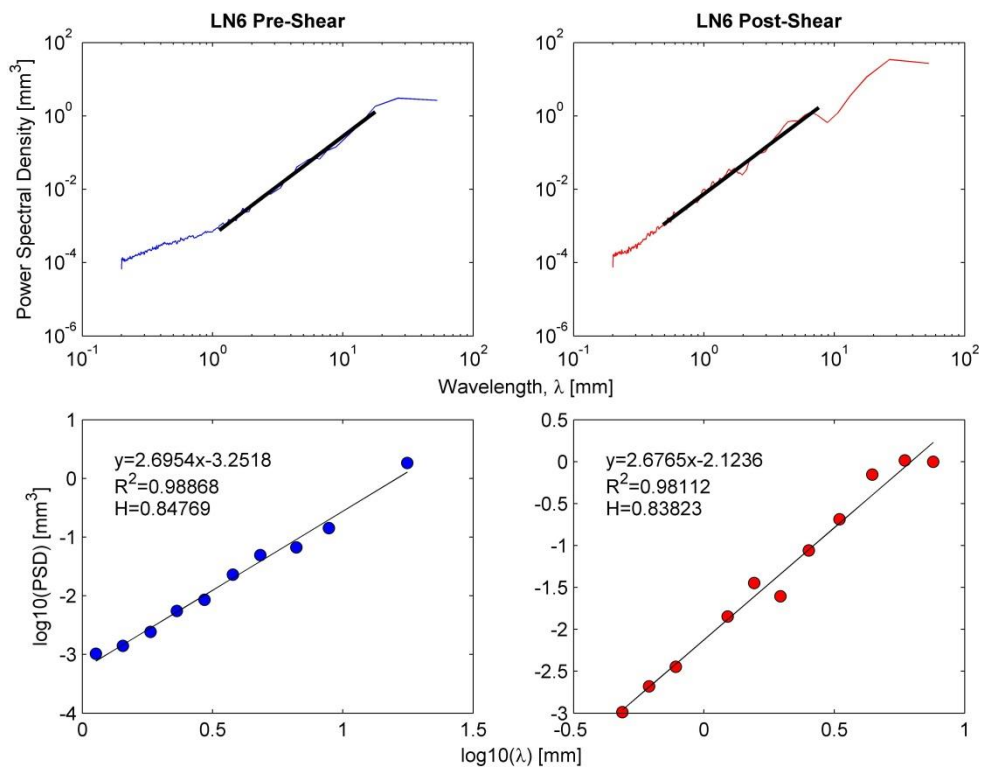


Figure 4.20. Least-squares analysis for sample LN6 ($\sigma_n=10$ MPa), blue color scheme represents the pre-shear data (left frames) and the red color scheme represents the post-shear data (right frames). Top frames represents the actual data with the fitted power law, bottom frames represent the linear fitting in arithmetic space, where H is the calculated Hurst exponent.

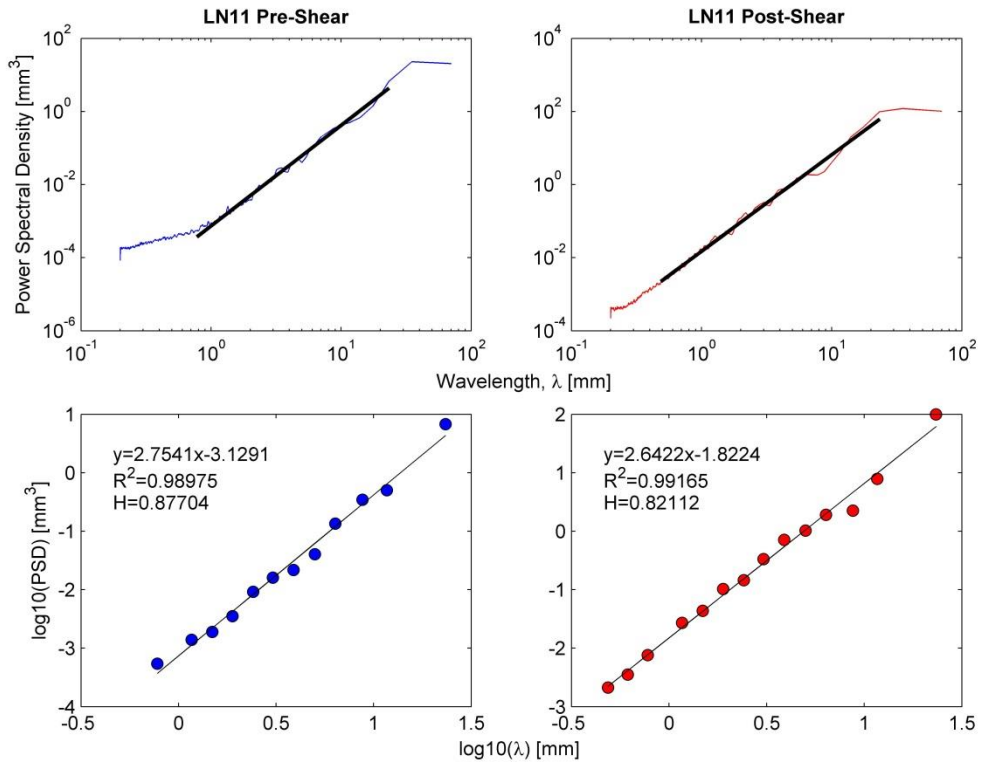


Figure 4.21. Least-squares analysis for sample LN11 ($\sigma_n=12.5$ MPa), blue color scheme represents the pre-shear data (left frames) and the red color scheme represents the post-shear data (right frames). Top frames represents the actual data with the fitted power law, bottom frames represent the linear fitting in arithmetic space, where H is the calculated Hurst exponent.

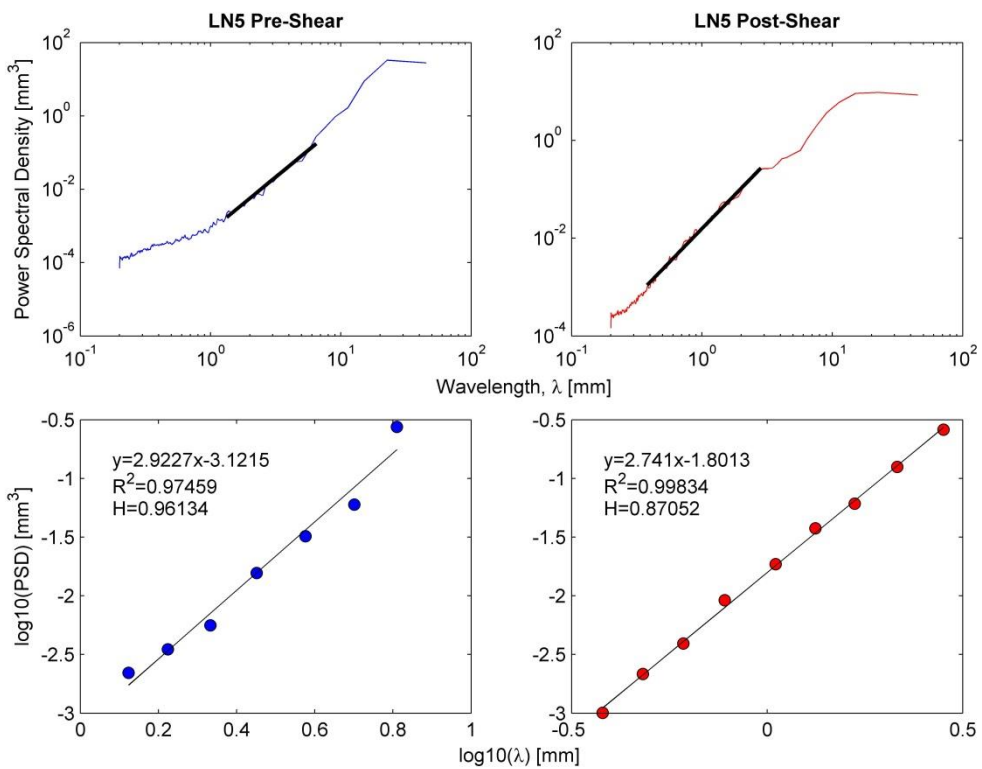


Figure 4.22. Least-squares analysis for sample LN5 ($\sigma_n=15$ MPa), blue color scheme represents the pre-shear data (left frames) and the red color scheme represents the post-shear data (right frames). Top frames represents the actual data with the fitted power law, bottom frames represent the linear fitting in arithmetic space, where H is the calculated Hurst exponent.

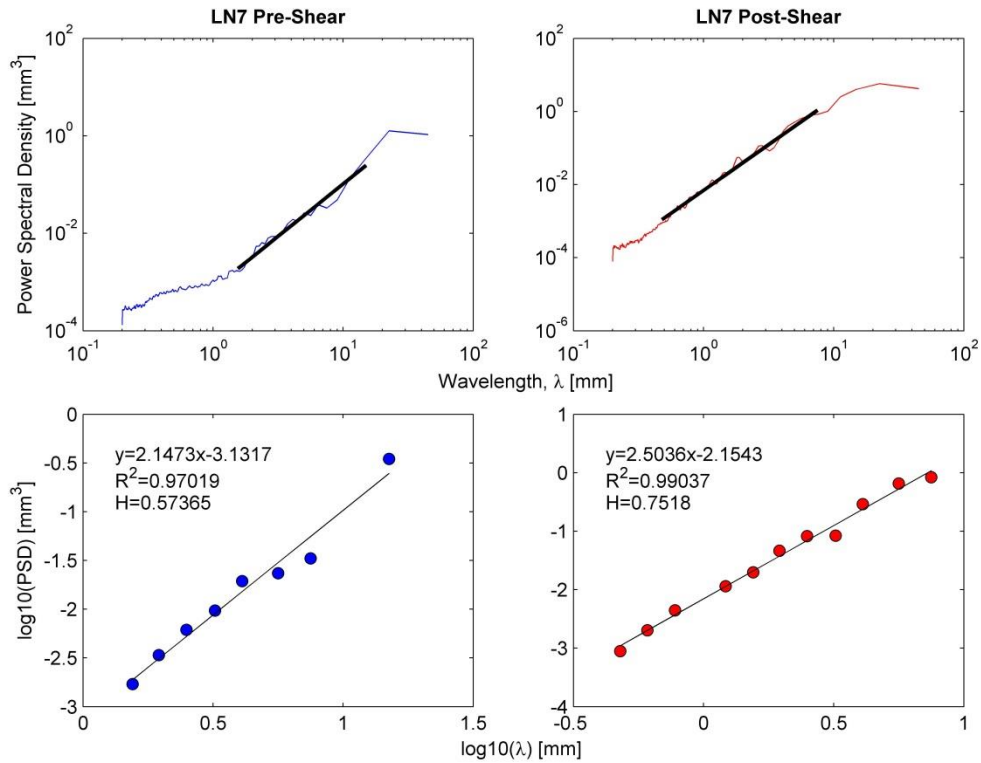


Figure 4.23 Least-squares analysis for sample LN7 ($\sigma_n=15$ MPa), blue color scheme represents the pre-shear data (left frames) and the red color scheme represents the post-shear data (right frames). Top frames represents the actual data with the fitted power law, bottom frames represent the linear fitting in arithmetic space, where H is the calculated Hurst exponent.

The following table summarizes the Hurst exponent results from all analyses (Figure 4.18-4.23):

Table 4.5. Calculated Hurst exponent results

Sample	Normal Stress [MPa]	H pre-shear		H post-shear	
		Value	Error	Value	Error
LN1	5	0.9	0.16	0.751	0.114
LN10	7.5	0.821	0.057	0.866	0.123
LN6	10	0.848	0.118	0.838	0.14
LN11	12.5	0.877	0.099	0.821	0.077
LN5	15	0.961	0.272	0.871	0.05
LN7	15	0.574	0.188	0.752	0.094

The analysis results (Figure 4.18-4.23, Table 4.5) exhibit Hurst exponent (H) values that range between 0.574 and 0.961. This range includes values from both the pre and post-shear surfaces. The values of H change before and after shear with maximum difference measured for sample LN7 and minimum difference measured for sample LN6. The values of H for the pre-shear surfaces range considerably, with a standard deviation of 0.134, this variability could be a product of the change in the slope of the PSD function at wavelengths smaller than

1. On the other hand, the values of H for the post-shear surfaces are less scattered and average at ~ 0.8 with a standard deviation of 0.054. This value of Hurst exponent is not uncommon and has been reported in past studies (e.g., Amitrano & Schmittbuhl, 2002). The computed values of H are valid for only the two orders of magnitude of length in which they were calculated from.

4.2.3 Visual-Morphological comparison

In addition to statistical analysis of roughness, the evolution of surface roughness was examined using optical measurements and photographic analysis (Figure 4.24-Figure 4.40 and Appendix I). Like the statistical analysis, visual morphological analysis was performed on the damage zones. The damage zones were identified by damage matrices, which were defined as the heights subtraction of the post-shear matrices from the pre-shear matrices (for pre and post-shear matrices plots, refer to Appendix I). Visual-morphological analysis was performed by comparing pre and post-shear profiles from the same damage zone. The pre and post-shear profiles represent matching rows from the pre and post-shear matrices, respectively. The heights of the pre and post-shear matrices were adjusted by identification of undamaged zones, which operated as a reference point. Some profiles exhibit areas where the post-shear profile is higher than the pre-shear profile (appear as negative values in the damage matrix), these localities include pulverized wear particles welded into the surface originating from the surrounding rock. This type of wear could not be removed from the rock surface prior to post-shear scanning; hence, it is inherently part of the measured data.

Post-shear surface pictures supplement the optical data. All the pictures were taken after removing the wear from the surfaces. Three main zones were identified on the sample surfaces: the penetrative damage zones (i.e. *damage zones*), undamaged zones, and zones of welded wear material (Figure 4.34). Regions in the surfaces which include combinations of the zones defined above also exist. Detailed analysis of the surface damage is presented below.

4.2.3.1 LN1 – Normal Stress=5 MPa

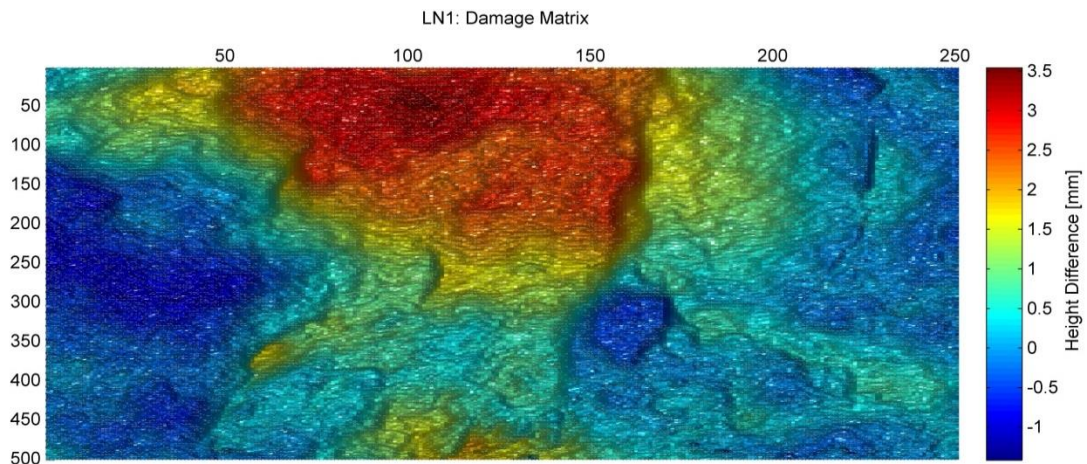


Figure 4.24. Damage matrix of the analyzed area from sample LN1. The matrix covers an area of $14.56 \times 25 \text{ mm}^2$. A large asperity (rows 1-300, columns 25-175) is completely sheared-off corresponding to the area of significant height difference.

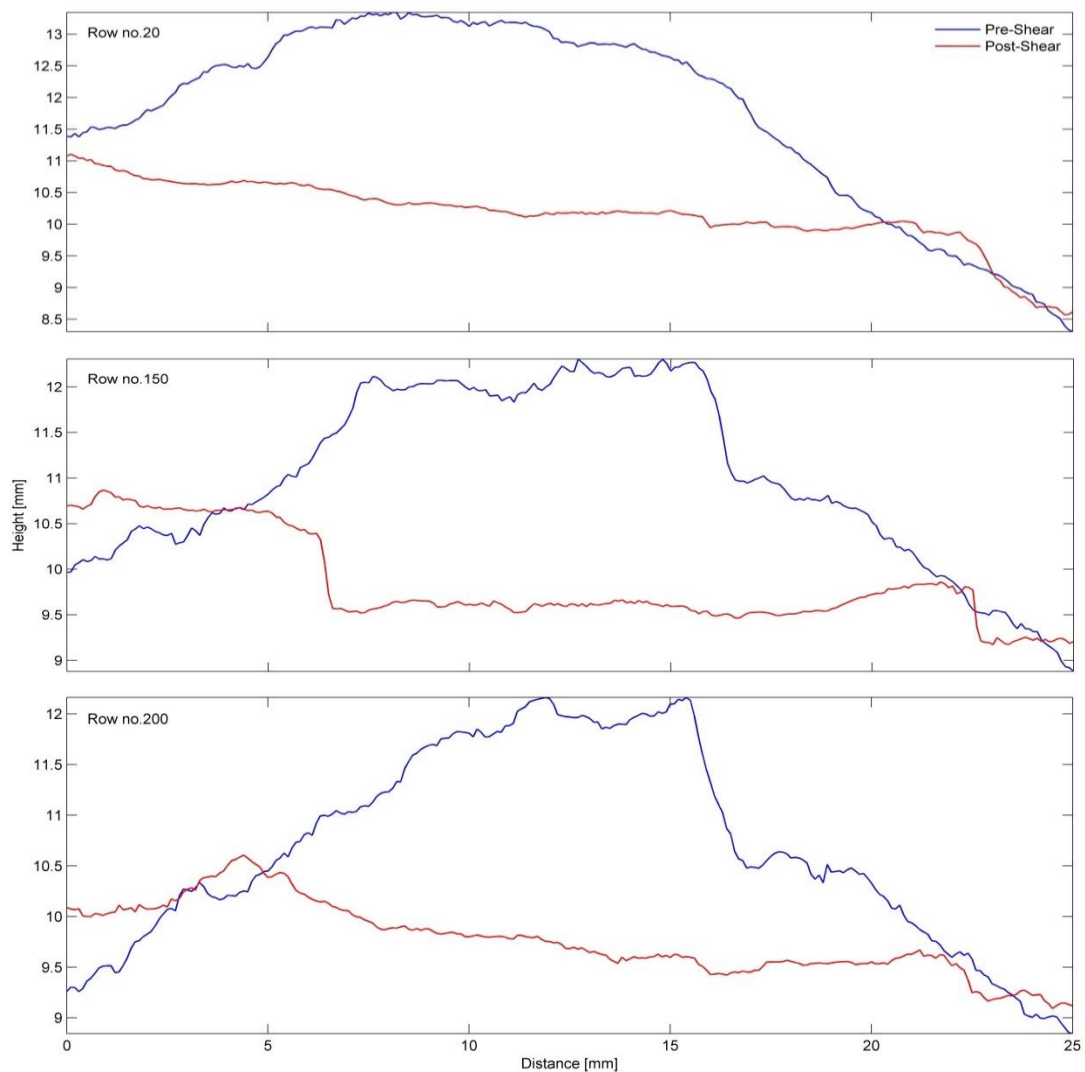


Figure 4.25. Pre (blue) and post-shear (red) profiles of damage. All three profiles display cross-sections of a sheared-off asperity. This asperity has great effect on the roughness of the pre-shear surface, once it is sheared-off the surface evolves to a smoother geometry.

The damage matrix for experiment LN1 (sheared under 5 MPa) reveals a large damage zone where a height difference of up to 3.5 mm is measured between the pre and post shear

height matrices (Figure 4.24). Cross-sections of the damage zone (Figure 4.25) show that a large asperity was truncated causing the overall roughness of the damage zone to decrease as a result.

4.2.3.2 LN10 - Normal Stress=7.5 MPa

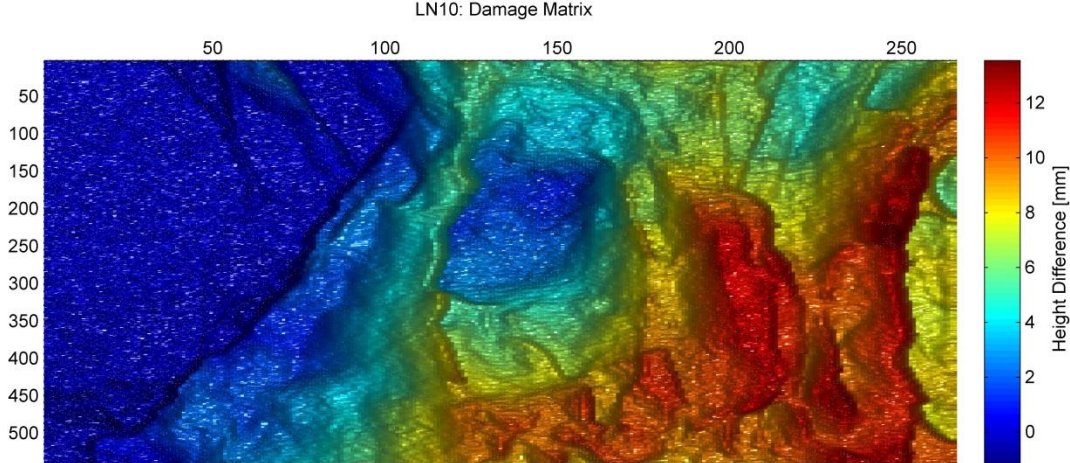


Figure 4.26. Damage matrix of the analyzed area from sample LN10. The matrix covers an area of 15.7x26.5 mm². A large damage zone featuring significant height difference is noticeable in the damage matrix, this zone includes fractures which are seen as elongated areas of great height difference values (parallel to the columns of the damage matrix).

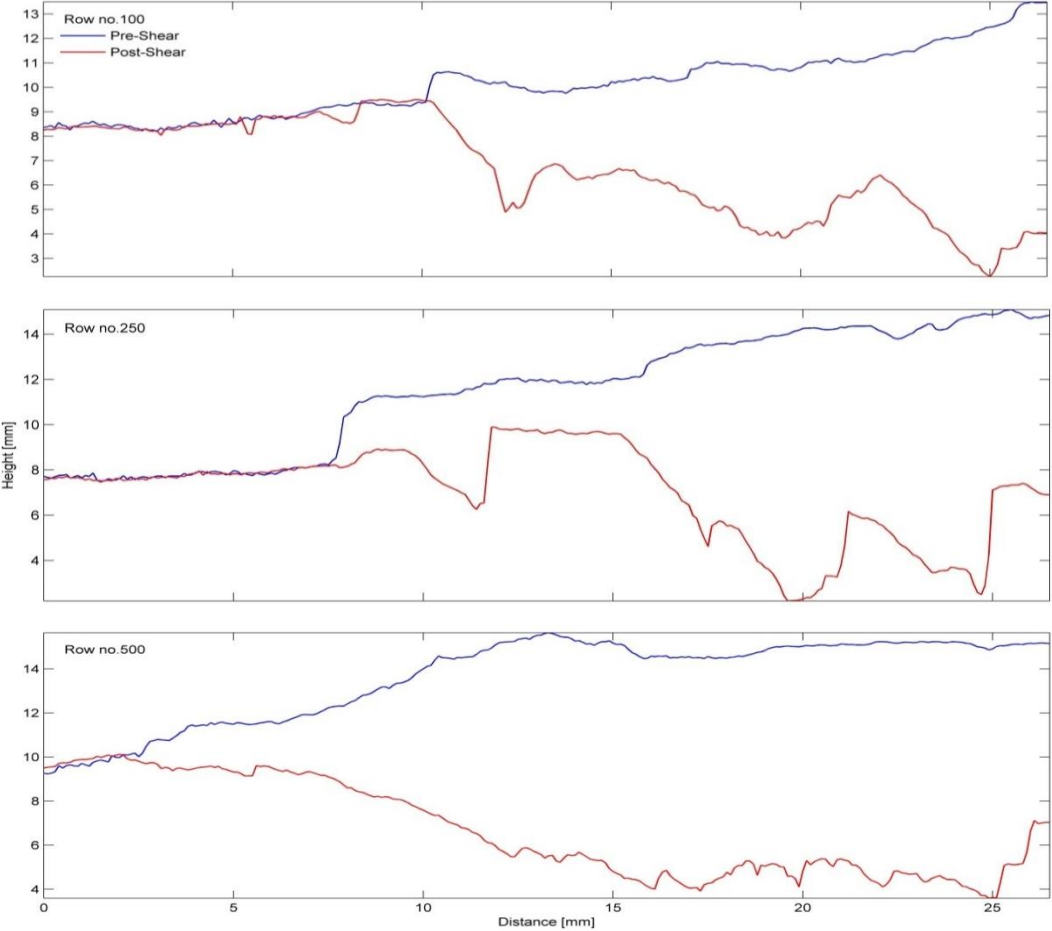


Figure 4.27. Pre (blue) and post-shear (red) cross-sections of the damage zone from sample LN10. The damage zone was created by removing a large portion of the surface material, resulting in greater surface roughness. The damage zone includes fractures, which are visible at distances: 12, 19 and 25 mm.



Figure 4.28. Post-shear photograph of sample LN10, top surface. The damage zone is visible on the right-hand side of the picture; it includes many tilted fractures, dipping to the right, and small white patches of pulverized rock. Undamaged zones can be seen to the left of the picture where the rock looks “fresh”. The areas covered in white powder are the welded wear localities. Direction of shear is to the right-hand side of the picture.

The damage matrix for experiment LN10 (sheared under 7.5 MPa) reveals a large damage zone that covers approximately half of the area of the matrix (Figure 4.26). The damage zone includes multiple fractures and pits (Figure 4.26-28). The fractures dip into the surface and cause penetrative damage. The detached material between the fractures leaves large pits in the surface, which are visible in the damage zone cross-sections (Figure 4.27). The post-shear profiles differ dramatically from the pre-shear profiles and display an overall increase in surface roughness.

4.2.3.3 LN6 – Normal Stress=10 MPa

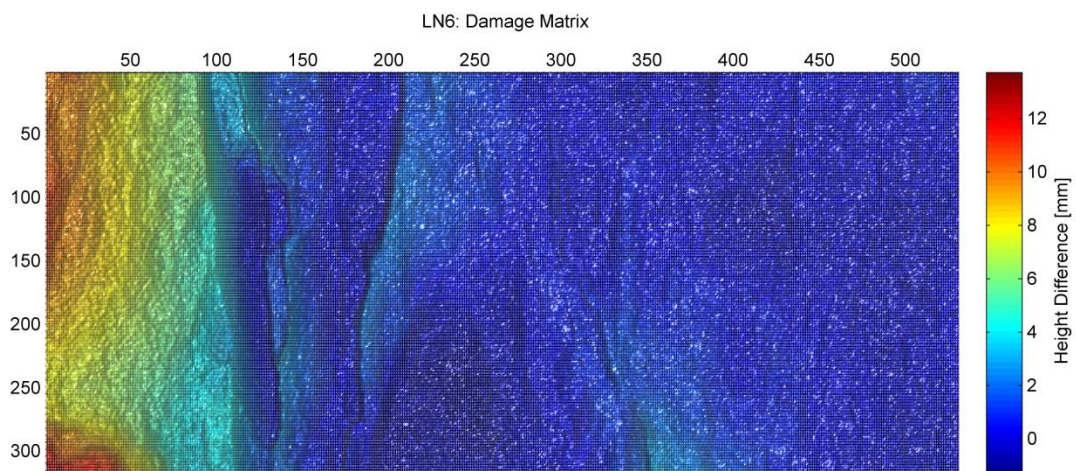


Figure 4.29. Damage matrix of the analyzed area from sample LN6. The matrix covers an area of $9.26 \times 53 \text{ mm}^2$. The damage zone is visible between columns 1-250. A large portion of the surface material is removed in the damage zone, including tilted fractures (elongated features which parallel the columns of the matrix).

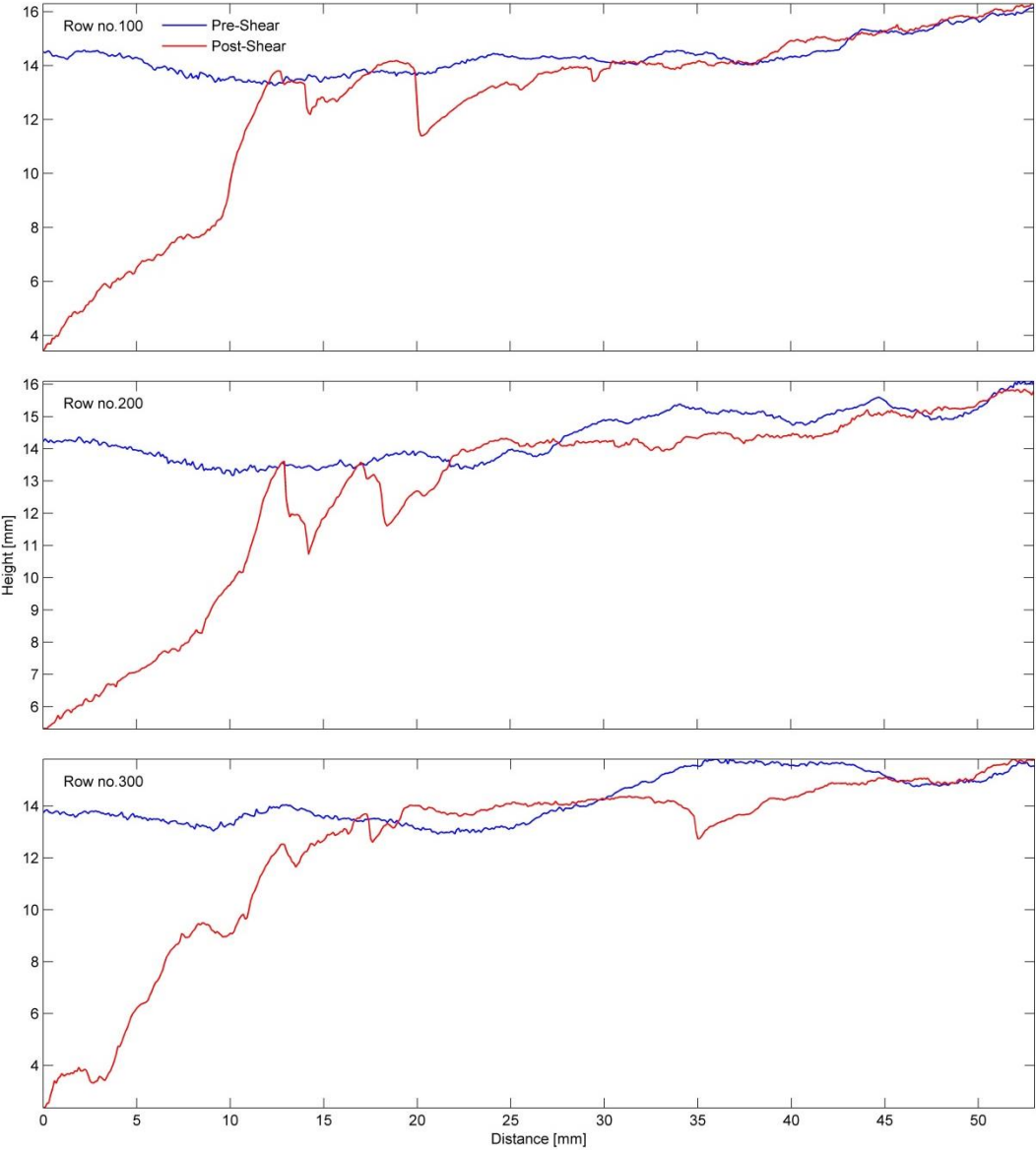


Figure 4.30. Pre (blue) and post-shear (red) cross-sections of the damage zone. The damage zone includes areas that evolved into rougher geometry with fractures (at distances 0-25 mm) and areas that underwent smoothing (profile #200 between distances 30-40 mm).



Figure 4.31. Post-shear photograph of sample LN6, bottom surface. The damage zone is seen on the bottom-left corner of the surface. The zone appears as a “hole” in the surface and includes tilted fractures dipping to the left. Shear direction is to the left-hand side of the picture.

The damage matrix for experiment LN6 (sheared under 10 MPa) reveals a relatively small damage zone (Figure 4.29), which is also seen in the surface picture (Figure 4.31). The maximum height difference between the pre and post-shear matrix reaches 13 mm. Most of the damage is limited to the edges of the surface (Figure 4.31) where a portion of the surface was detached. The damage zone includes dipping fractures visible in the damage matrix (Figure 4.29) and the damage zone cross-sections around distances of 10, 15, 18 and 35 mm (Figure 4.30).

4.2.3.4 LN11 – Normal Stress=12.5 MPa

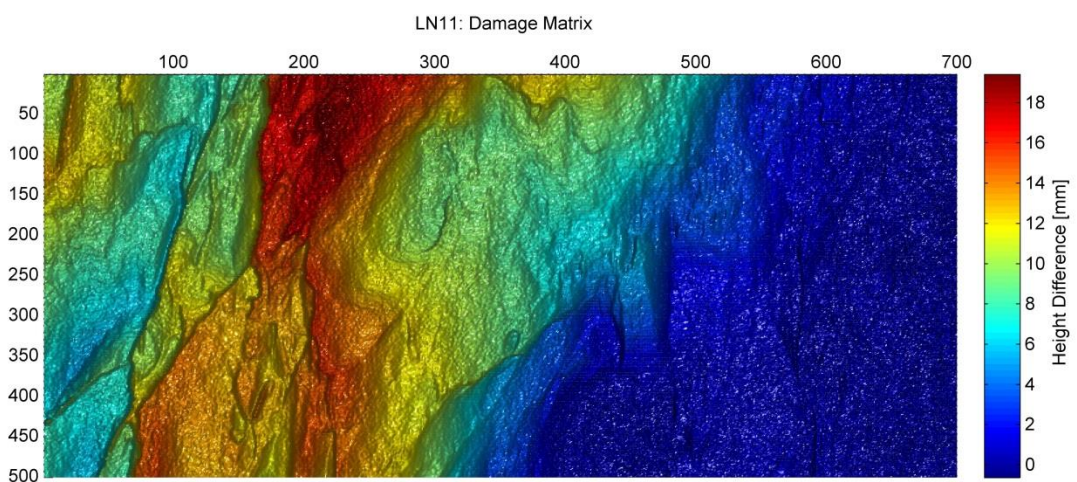


Figure 4.32. Damage matrix of the analyzed area from sample LN11. The matrix covers an area of $14.56 \times 70 \text{ mm}^2$. A large damage zone is visible on the left of the matrix and is located closely to an undamaged zone (blue area on the right of the matrix). Multiple fractures are visible in the damage zone and are noticeable as elongated features that are sub-parallel to the columns of the matrix.

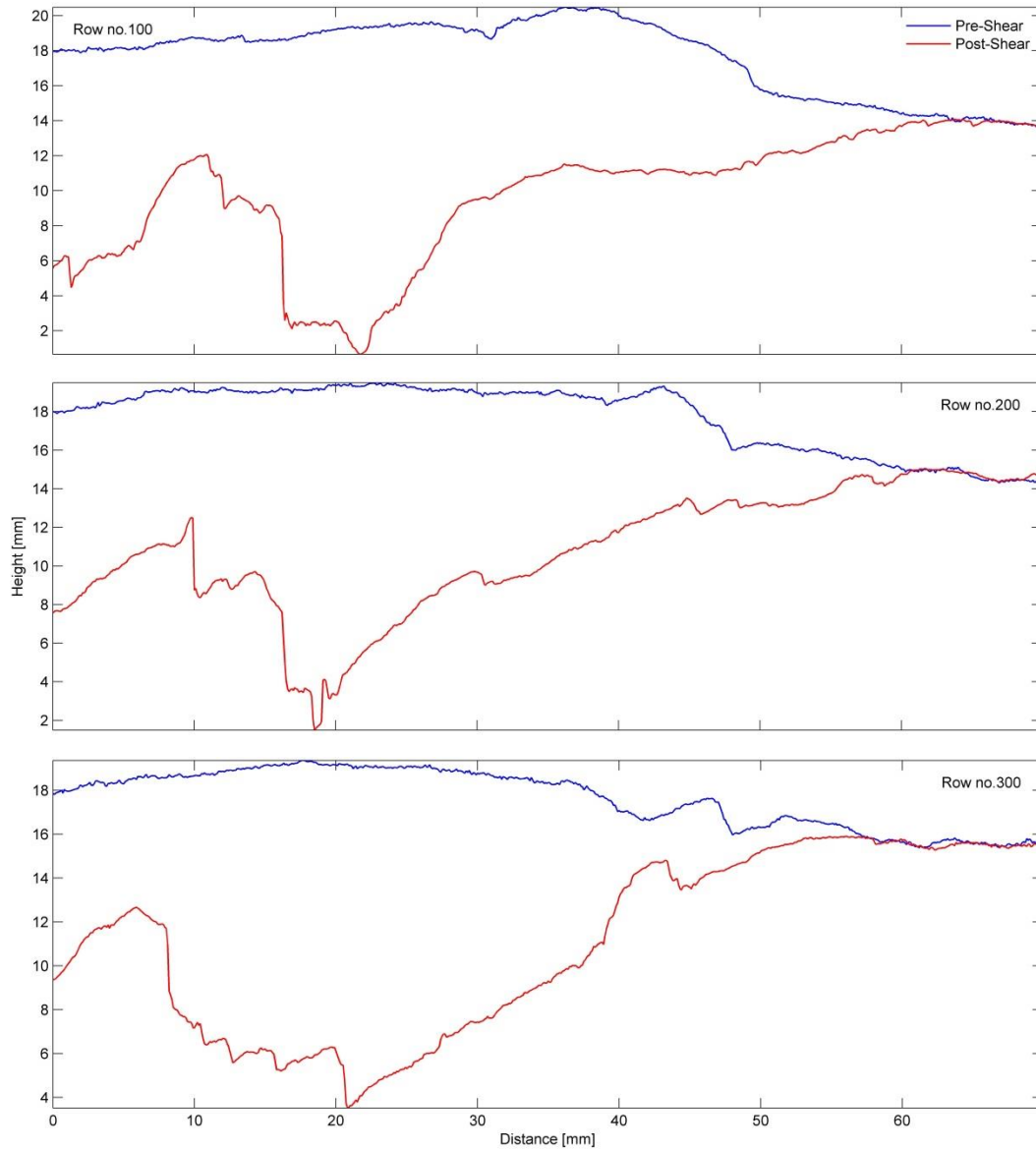


Figure 4.33. Pre (blue) and post-shear (red) cross-sections of the damage zone. The extensive damage zone is formed by removal of large rock volume from the surface. The shape of the new surface (post-shear) is irregular, including newly formed asperities and fractures.

The damage matrix for experiment LN11 (sheared under 12.5 MPa) reveals an extensive damage zone which includes multiple fractures which penetrate into the surface (Figure 4.32; Figure 4.33 at distances 10, 12 and 20 mm). The measured height difference between the pre and post-shear matrices reaches 19 mm and indicates the large wear volume produced in the experiment. The fractures in the damage zone are dense with a measured mean spacing of 2.67 mm and the post-shear surface topography is highly irregular as a direct result of the dipping fractures (Figure 4.33). The fractures penetrate and break the original surface material leaving pits with a variety of sizes and shapes. Examples for these are seen in Figure 4.33: top plate – distances 5, 20 mm; middle and bottom plates – distance 20 mm.

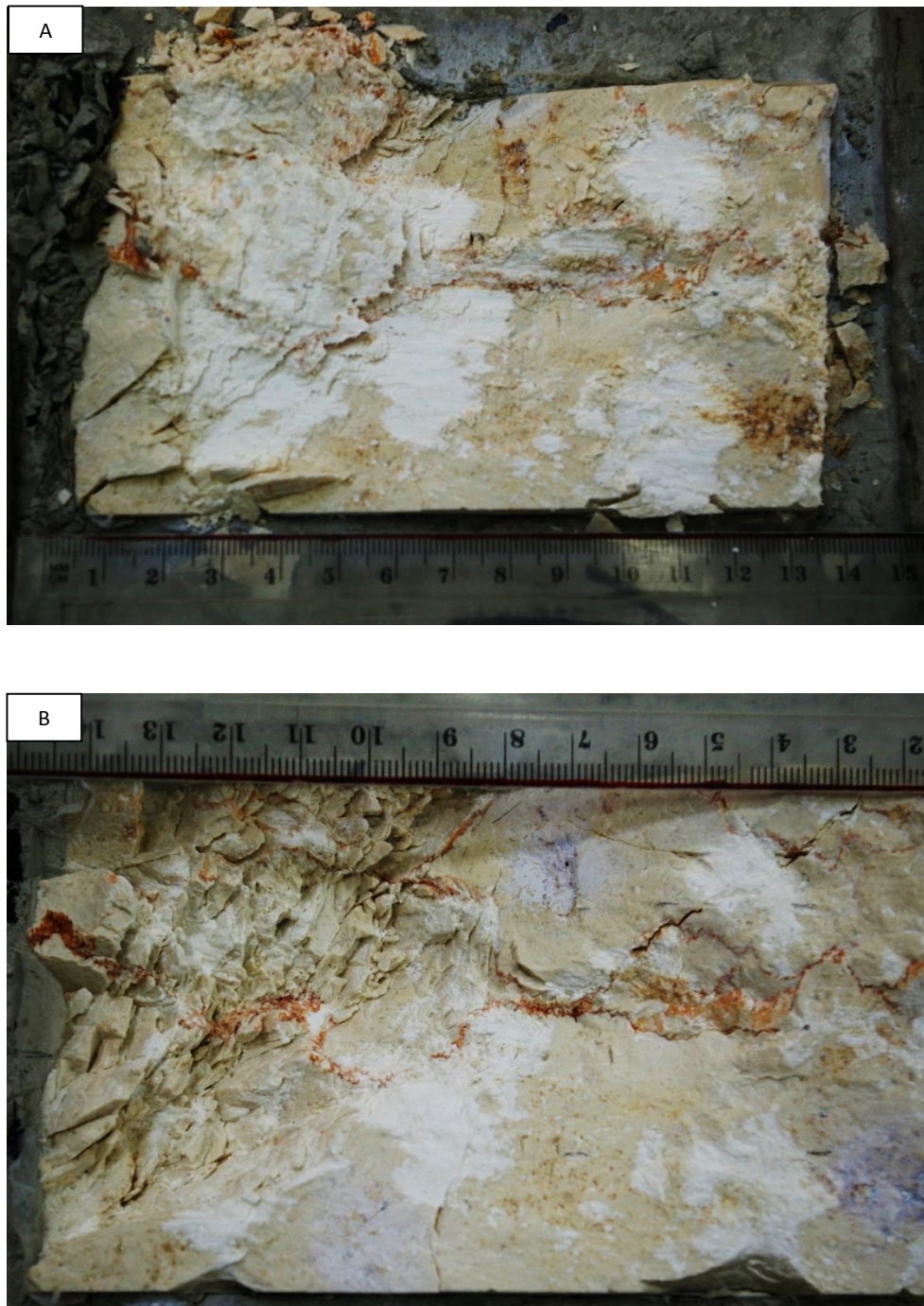


Figure 4.34. Post-shear photographs of sample LN11, bottom surface. (A) The post-shear surface prior to wear removal, note the large zone of penetrative damage at the left – this area is the damage zone (visible at B) covered by detached rock particles. Striations are visible on the white patches in the middle and the right of the surface. (B) The post-shear surface after wear removal. The damage zone is revealed at the left-hand side of the photograph, including fractures dipping to the top-left corner of the surface. White patches and non-damage zones are visible at the center and right-hand side of the surface.

The penetrative damage is clearly visible in Figure 4.34. Before wear removal (Figure 4.34A) only a small portion of the fractures is noticeable along with undamaged zones and dispersed localities of white welded wear particles. After wear removal (Figure 4.34B) the high density of the fractures is revealed and the localization of the penetrative damage is visible; all of the penetrative damage is localized in the damage zone (left-hand side of Figure 4.34B).

4.2.3.5 LN5 – Normal Stress=15 MPa

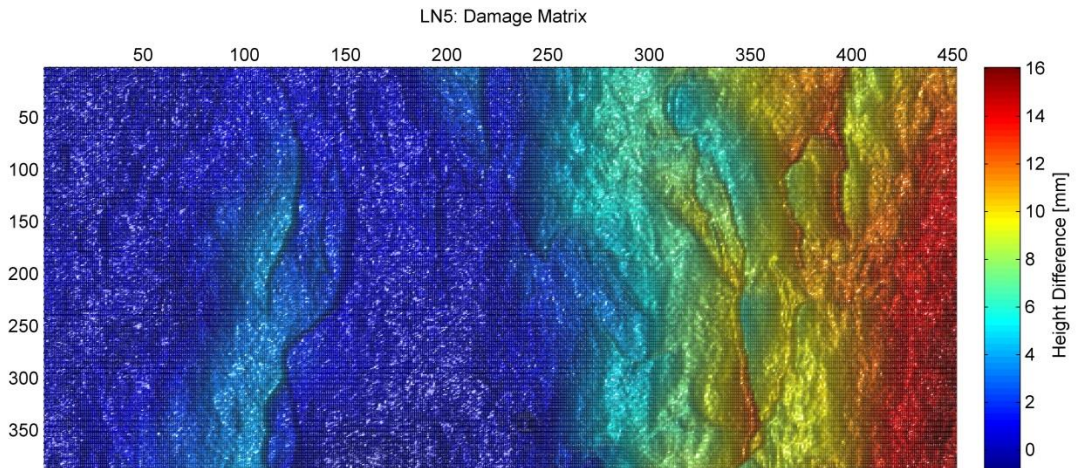


Figure 4.35. Damage matrix of the analyzed area from sample LN5. The matrix covers an area of 11.24×45.1 mm². The damage zone contains clear fractures, which are represented as elongated features between columns 100—150 and 300-400.

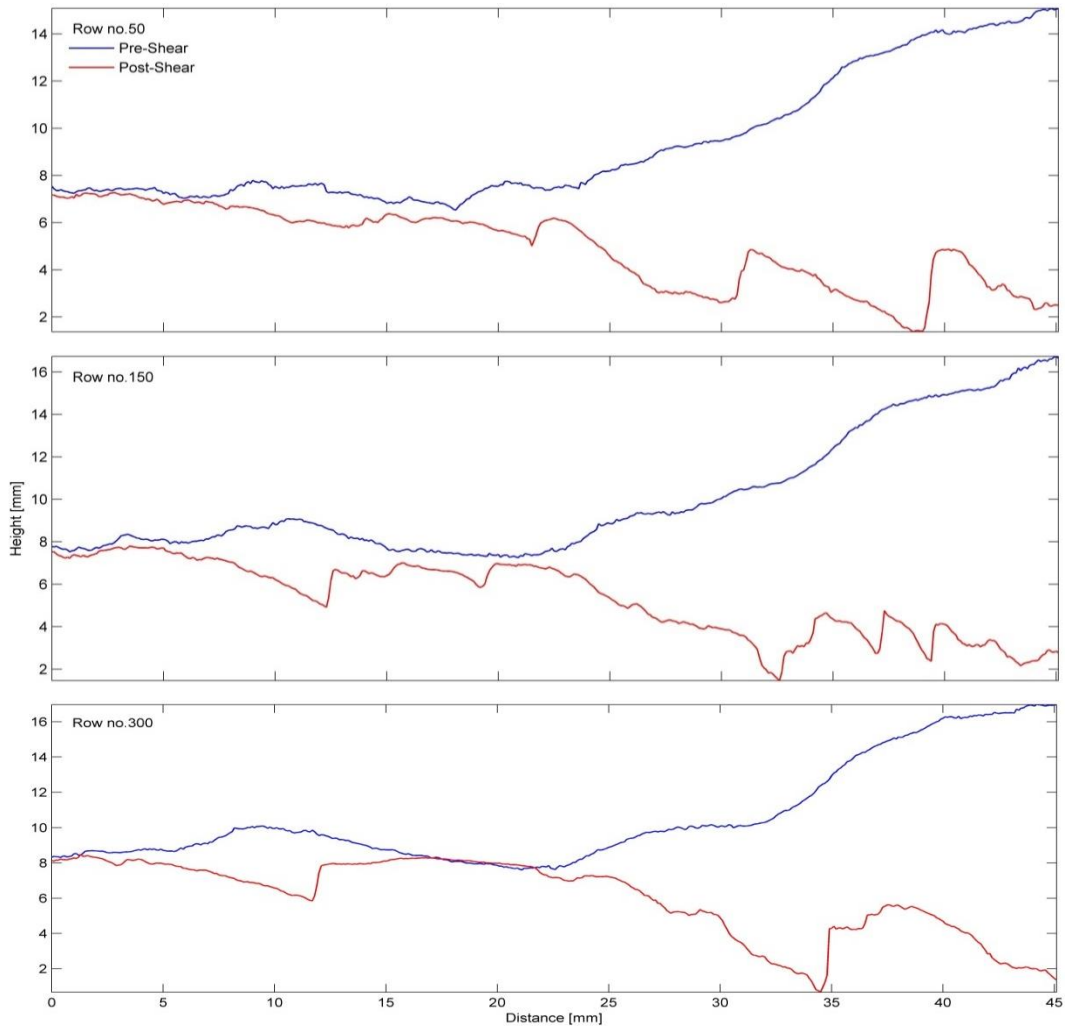


Figure 4.36. Pre (blue) and post-shear (red) cross-sections of the damage zone. The damage zone includes minor areas of small scale smoothing (profile #300, distances 15-22 mm) alongside major areas of surface roughening. The roughening of the surface is enhanced by fractures (all profiles, distances 12 and 30-45 mm) forming abrupt irregularities in the cross sections' geometry.



Figure 4.37. Post-shear photograph of sample LN5, bottom surface. The damage zone is visible in the right-hand side of the surface, note the jagged formations of broken rock when viewed from above. More damage and welded wear is visible on the rest of the surface in the white patches.

The damage matrix for experiment LN5 (sheared under 15 MPa) reveals a large damage zone with a height difference of up to 16 mm between the pre and post-shear matrices (Figure 4.35). Multiple dipping fractures are visible from the post-shear profiles (Figure 4.36) at distances: 12 mm (middle and bottom plates); 20 mm (top and middle plates); and multiple fractures between 30-40 mm (all plates). The fractures penetrate the surface causing pitting which lead to a rougher post-shear geometry (Figure 4.36), the traces of the fractures and the pits in the post-shear surface are noticeable on the right-hand side of Figure 4.37.

4.2.3.6 LN7 – Normal Stress=15 MPa

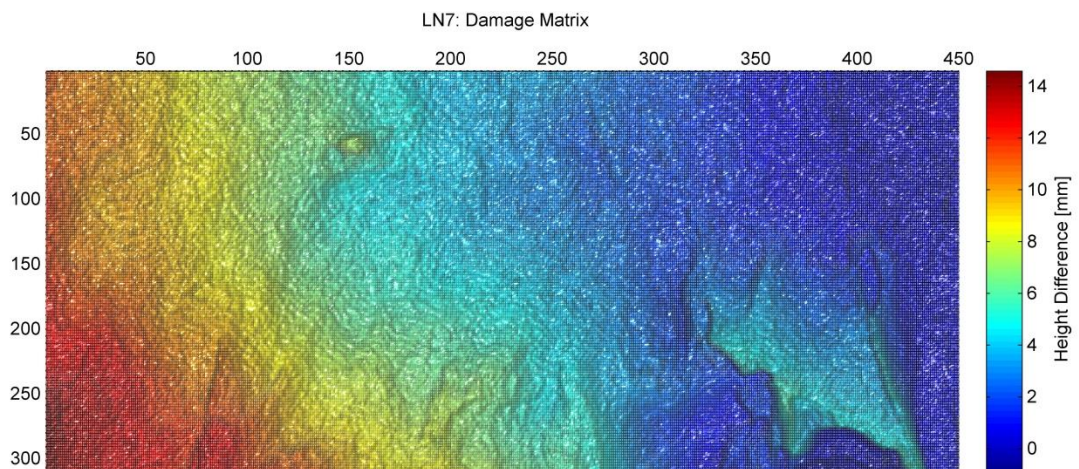


Figure 4.38. Damage matrix of the analyzed area from sample LN7. The matrix covers an area of $9.03 \times 45 \text{ mm}^2$. Two different damage zones are present in the damage matrix; large damage zone (between columns 1-250) – the change in the surface topography is gradual, increasing towards the bottom-left corner of the matrix; small damage zone (between columns 350-420) – looks as an abrupt change in the topography.

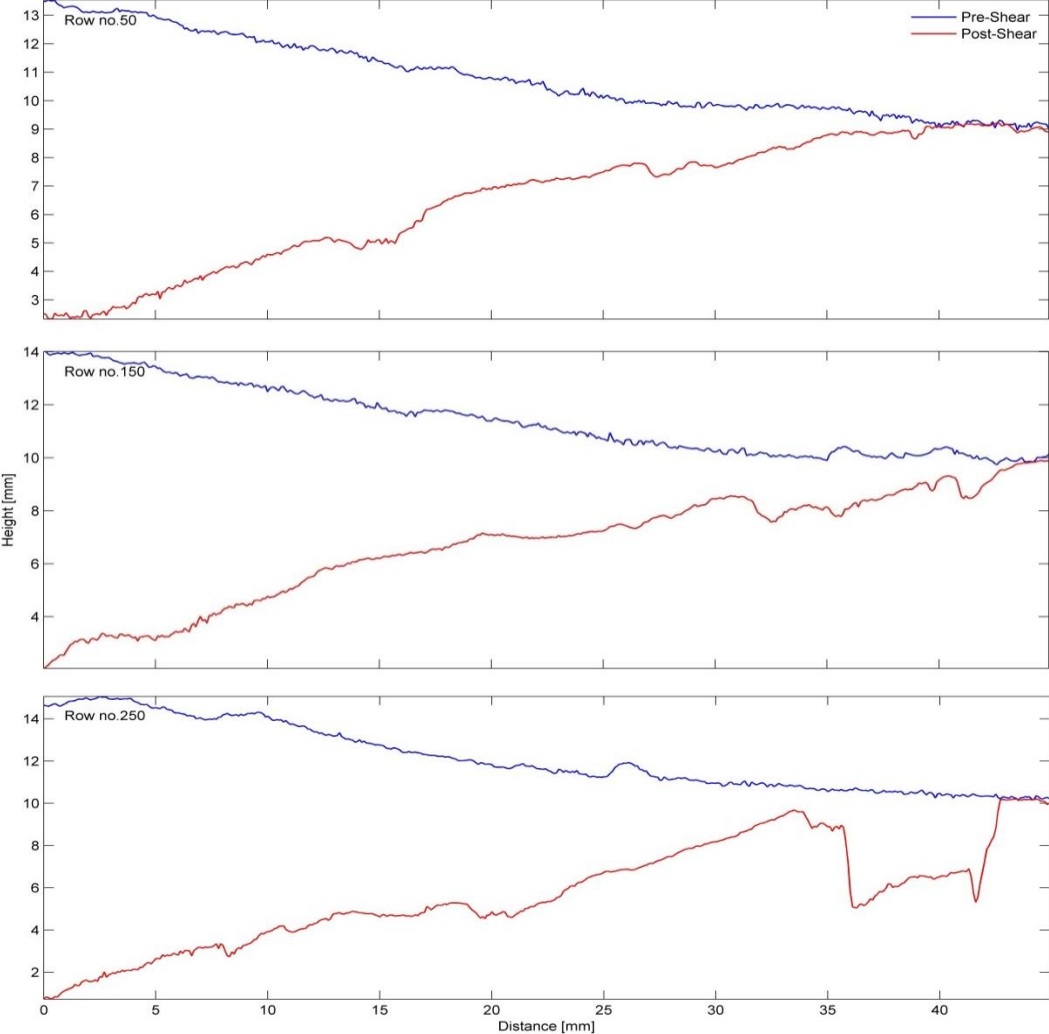


Figure 4.39. Pre (blue) and post-shear (red) cross-sections of the damage zone. Two sub-zones are visible; a large volume damage zone (all profiles, distances 0-35) which demonstrates a more gradual smooth change in surface roughness; and a small damage zone (profile #250, distances 35-45 mm), demonstrating great roughening of the post-shear surface as if the material was gouged (plucked) out.



Figure 4.40. Post-shear photograph of sample LN7, bottom surface. The damage zone is seen to the bottom-left corner of the surface. Notice the small fractures in the central white patch, their dip and direction is similar to the fractures in the damage zone.

The damage matrix for experiment LN7 (sheared under 15 MPa) reveals a medium-large damage zone with a maximum height difference of 14 mm between the pre and post-shear matrices (Figure 4.38). The damage zone contains some fractures (Figure 4.40) and a relatively large pit (Figure 4.39 bottom plate). These features increase the irregularity of the post shear surface when compared to the pre-shear surface. It should be noted that the amount of fractures present in this sample is smaller compared to the other high-normal stress experiments (including experiment LN5, which was sheared under the same normal stress).

To summarize, surfaces from all experiments contained zones of damage (including the main “damage zone”), and zones of no damage. The combination of the quantitative analysis of the damage zones and the visual analysis of the surface pictures suggest that the penetrating damage, fractures and pits, were the main cause for surface roughening. In experiment LN1, which was sheared under 5 MPa, no fractures were present in the post shear surface (refer to Appendix I) and the surface smoothed by decapitating a large, irregular asperity. The smoothing was clearly visible to the naked eye at most scales. However, for surfaces sheared under greater loads (≥ 7.5 MPa), surface roughening was prominent, featuring fractures (Figure 4.28; Figure 4.31; Figure 4.34; Figure 4.37; Figure 4.40). The fractures dip at high angles (30 - 50°) below the horizon against the shearing direction of the surface (Figure 4.41). The fragmentation caused by these fractures was expressed as significant surface irregularities. Moreover, even without the presence of the fractures, the

surface became rougher, breaking asperities of all sizes into complex shapes (Figure 4.33, profile #300, distance 45 mm).

Sample LN7 (Figure 4.39), sheared under 15 MPa, exhibited two different damage sub-zones. While the rock volume changed dramatically as in the other 15 MPa experiment (LN5), the large damage sub-zone does not contain fractures. Instead, the overall change in surface roughness is relatively small in the large sub-zone. The smaller damage sub-zone is more localized and looks as if the surface underwent plucking (gouged or scooped-out asperities), thus creating an abrupt change in the surface profile. Plucking was observed in other experiment (Figure 4.33 profile #300, distance 45 mm; Figure 4.36 profile #150, distance 5-15 mm), but not at such a large scale.

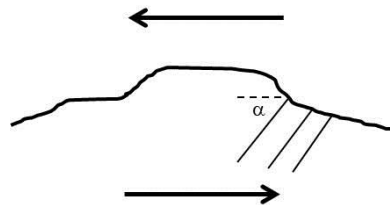


Figure 4.41. Schematic illustration of the shear induced fractures and their location on a rough surface. The solid black line represents the rough surface profile. The thin solid lines represent the fractures, their orientation is denoted by α . The arrows represent the direction of shear displacement.

4.2.4 Roughness Evolution Comparison of Two Mating Surfaces

Wear producing frictional sliding between two surfaces, inherently modifies their geometry. This section concludes the roughness evolution results, through RMS ratio, of mating areas from the bottom and top surfaces of each experiment.

Scanning the surfaces was done in “scanning strips”; which helped matching data from the top and bottom surfaces. Each scanning strip from the bottom surface had a matching counterpart in the top surface. Figure 4.42 includes six plots, each from a different run, under different normal stress conditions. Each plot includes RMS ratio data of a scanning strip from the bottom surface (blue) and its matching counterpart from the top surface (red). These results help determine the roughness changes of two contacting, mating areas in the surface.

The plots include data from medium-resolution scans, in order to account for greater surface area, thus errors are included at the smallest wavelength (0.2-0.5 mm) and the longest wavelength (greater than the total length of the sample; >13 mm). The analysis is performed with respect to the data in between the mentioned error zones (threads of the lines in each plot).

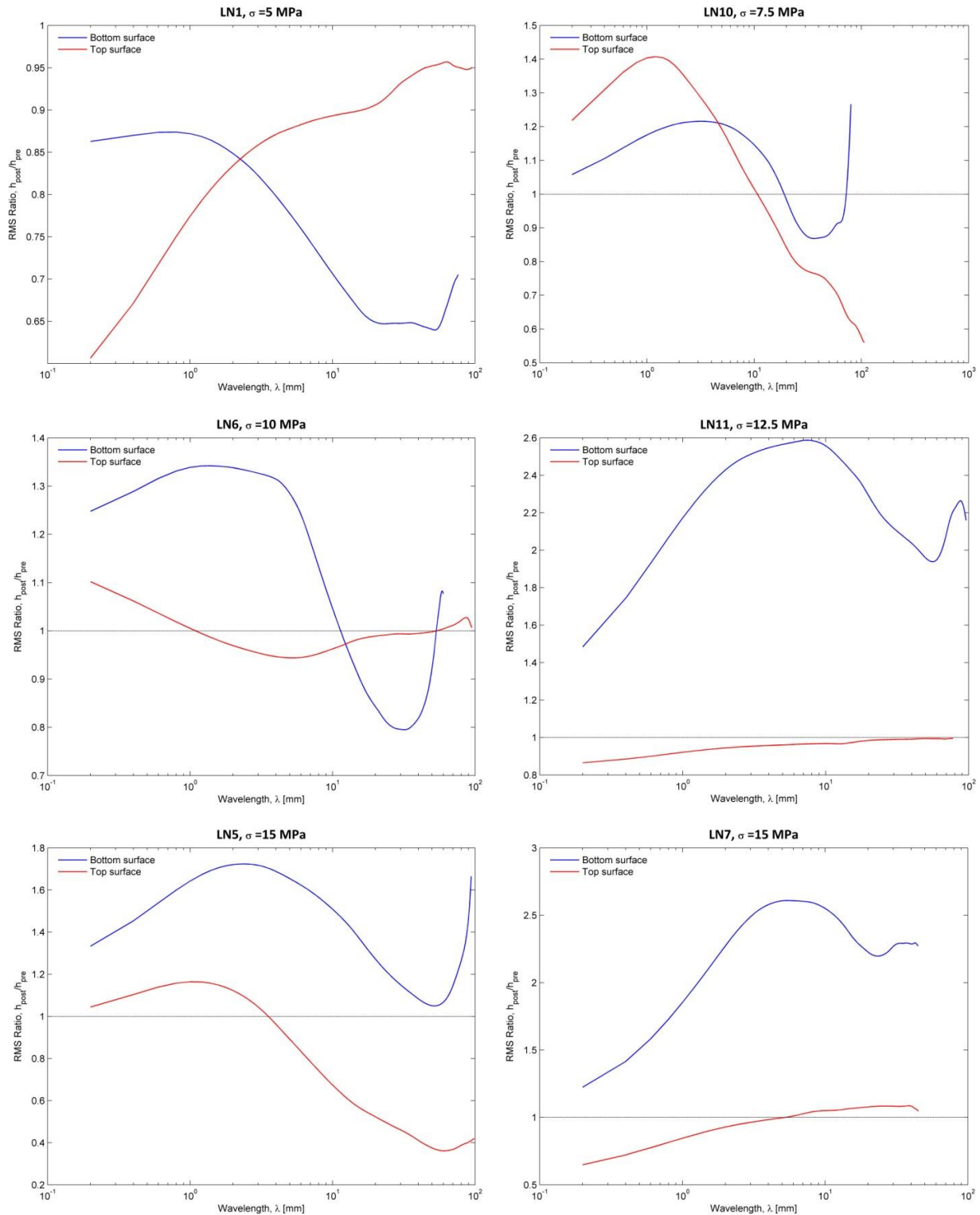


Figure 4.42. Mating surfaces roughness evolution comparison by RMS ratios. The RMS ratios for each mating surface are plotted for every experiment. Blue curve – bottom surface roughness evolution; Red curve – top surface roughness evolution.

Looking at the low normal stress runs (samples LN1 and LN10 sheared under 5 and 7.5 MPa, respectively), both mating surfaces experience roughness change. Under a load of 5 MPa (Figure 4.42 upper left plate), both surfaces smooth but at different wavelengths. Under a load of 7.5 MPa (Figure 4.42 upper right plate) the surfaces roughen in short-medium wavelengths (~ 0.5 -10 mm) but smooth at the long wavelengths (>10 mm). This behavior

differs between the surface only in intensity, where the upper surface experiences greater roughness change (roughening and smoothing).

The higher load runs (10-15 MPa) exhibit different behavior between the surfaces. Looking at the results for samples LN6, LN11 and LN7 (sheared under: 10, 12.5 and 15 MPa, respectively), one surface undergoes significant roughening (exceeding RMS ratio values of up to 2.5), while the opposite surface experiences minor changes, either smoothing or roughening. Sample LN5 (Figure 4.42 lower left frame), which was also sheared under 15 MPa, displays roughening at all scales at the bottom surface, while the top surface undergoes minor roughening at short wavelengths and smoothing at long wavelengths.

4.3 Wear Analysis

As noted in chapter 2, wear production is an intrinsic process during frictional sliding of rocks. The results shown in section 4.2 support this notion as the limestone surfaces underwent serious morphological changes during shear, the wear particles are a product of these changes. Wear volume was measured using optical measurements. The height difference between the pre-shear and the post-shear matrices was translated into removed material volume (=wear), utilizing the number of points in a matrix and the total area covered by the matrix (explained in the chapter 3). Two types of wear material were recognized during experimentation: crushed rock particles and powder (Figure 4.43). Crushed rock particles were large detached fractions of the rock surfaces, those wear products were removed from the surfaces prior to post-shear scanning by means of air pressure and scrubbing with a soft toothbrush. Powder, was recognized as pulverized rock with clay texture; this kind of wear was welded during shear to the surfaces (at some of the locations). The welded particles could not be removed from the surface by the noted methods. Instead, the surfaces were scanned with the localized zones of welded wear material. This material is noticeable from the cross-sections of the surface matrices as areas where the post-shear topography is higher than the pre-shear topography of the same location. The welded wear powder height differences (appear as negative height differences from the damage matrix) were not calculated as part of the total wear volume analyzed in this section.

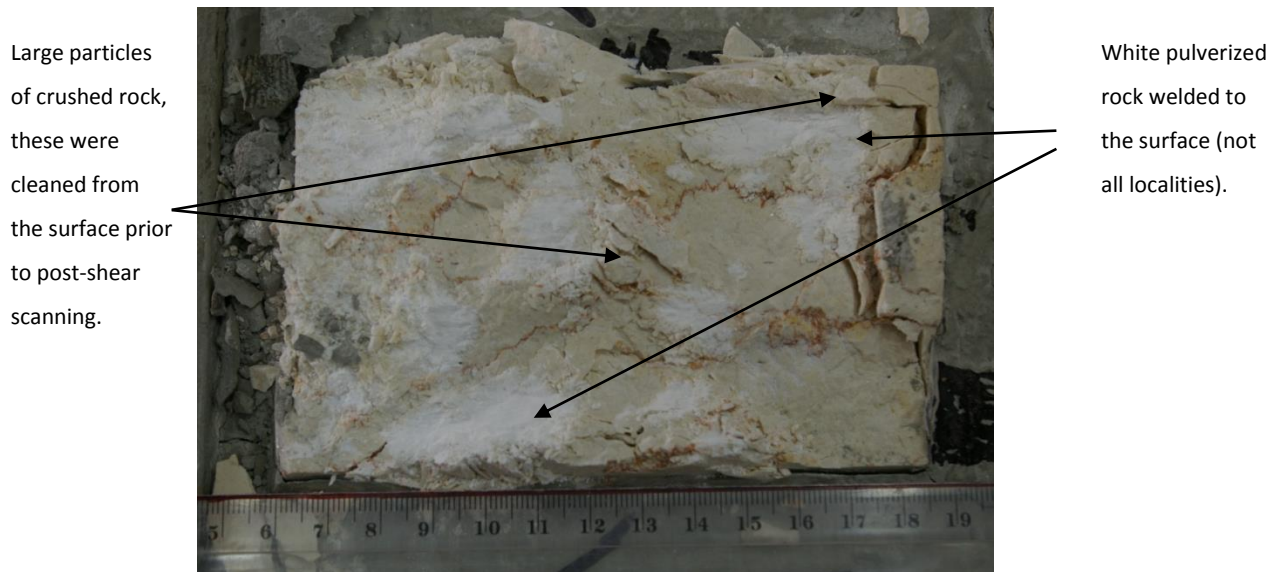


Figure 4.43. Post-shear photograph of the bottom surface of sample LN11. Two types of wear particles are visible: crushed rock and powder. The crushed rock is easily removed from the surface by hand of a jet of air. The white powder sticks to the surface at some locations and is scanned along with the rest of the surface in the post-shear scan. The direction of shear is to the right of the picture.

The wear analysis was performed on damage zones scanned by the 75 mm lens. The total measured wear volume from a damage zone was normalized by the total area of the the damage zone; hence, the wear volume is in units of millimeters.

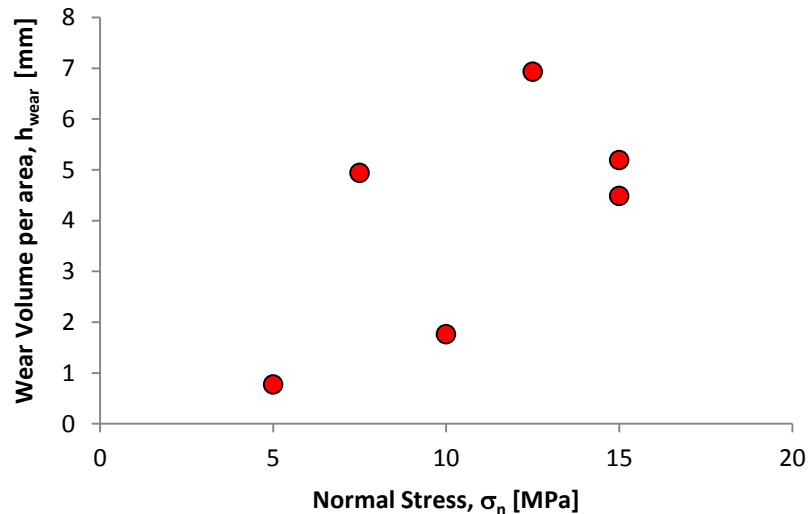


Figure 4.44. Variations of accumulated wear volume per damage zone with normal stress. Each data point represents one experiment.

The calculated wear volume increases with the normal stress, reaching a maximum value of ~7 mm when shearing under 12.5 MPa. The minimal wear volume is measured for the low normal stress experiment; sheared under 5 MPa. The 10 MPa experiment (LN6) yielded significant lower wear volume, with respect to the 7.5 and 12.5 MPa runs. Both 15 MPa runs (samples LN5 and LN7) produced similar wear volume, but still less than the maximum for the 12.5 MPa run.

5 Analysis of Experimental Results

5.1 Mechanical Interactions

In this section the experimental results are analyzed. Because stress, friction, wear and roughness are all interrelated aspects of frictional sliding it is important to examine them together. Thus, the direct shear test results are integrated with the roughness evolution results in order to better understand the relationship between them.

5.1.1 Dilation and Asperity Interactions

The dilation-displacement curves shown in section 4.1.1 present an interesting behavior. Once shear displacement ensues, the rough mating-surface configuration contracts, this is followed by a stage of dilation, during which peak shear stress is attained. This contraction-dilation behavior is controlled by the surface roughness. At the initial part of the shear loading segment, the asperities interlock and undergo elastic strain which causes the overall measured contraction. Afterwards, some of the interlocking asperities begin to slip and climb over each other through the proposed riding-up mechanism (*Scholz, 2002*) which in turn, causes the overall dilation. Therefore, it can be assumed that during shear displacement, the asperities interact via the interlocking and riding-up mechanisms.

5.1.2 Relation between Friction and Wear

The coefficient of friction was calculated here for two conditions, peak and residual shear stress. The peak friction coefficient (μ_{peak}) relates to the peak shear stress while residual friction coefficient (μ_{res}) relates to residual shear stress. Peak friction coefficient was measured after a few millimeters (2-6) of displacement for each experiment, during that stage the rough surfaces exhibited slip-hardening behavior (*Biegel et al., 1992*). The friction results in the experiments were interesting because maximum and minimum values of friction did not necessarily coincide with the normal stress imposed in the experiments. Maximum friction coefficient was measured in experiment LN11 ($\sigma_n=12.5$ MPa) where $\mu_{\text{peak}}=0.997$. Minimum values of the friction coefficient were measured in experiment LN1 ($\sigma_n=5$ MPa) and experiment LN6 ($\sigma_n=10$ MPa) where $\mu_{\text{peak}}=0.724$ and $\mu_{\text{peak}}=0.661$, respectively. In the latter experiment peak shear stress conditions were reached after a relative long displacement of 6 mm, which also included a minor event of shear sliding (Figure 4.3). The sliding event along with the long displacement prior to peak conditions could relate to the relatively low coefficient of friction measured in that experiment. Moreover, the stress-displacement behavior of experiment LN6 could also have been a product of the initial surface roughness as equal-roughness is irreproducible with the four-point bending method used to make the tested

surfaces. Furthermore, experiment LN6 exhibited a low value of shear stiffness (relative to the imposed normal stress) (Figure 4.11). The low shear stiffness of the surface could have also contributed to the relative “weak” mechanical behavior of the sliding interface.

Wear was calculated in each experiment through optical measurements as explained in section 3.4.6. As with the friction, the calculated peak wear volumes (per area) did not coincide with maximum normal stress levels. Instead, peak wear values were measured in experiment LN11 ($\sigma_n=12.5$ MPa) which also exhibited maximum friction. Minimum wear values were measured in experiment LN1 ($\sigma_n=5$ MPa) and LN6 ($\sigma_n=10$ MPa) where the lowest values of friction were also measured. Thus, it is argued here that wear volume per area relates better to the peak friction coefficient in frictional sliding of rough surfaces (Figure 5.1).

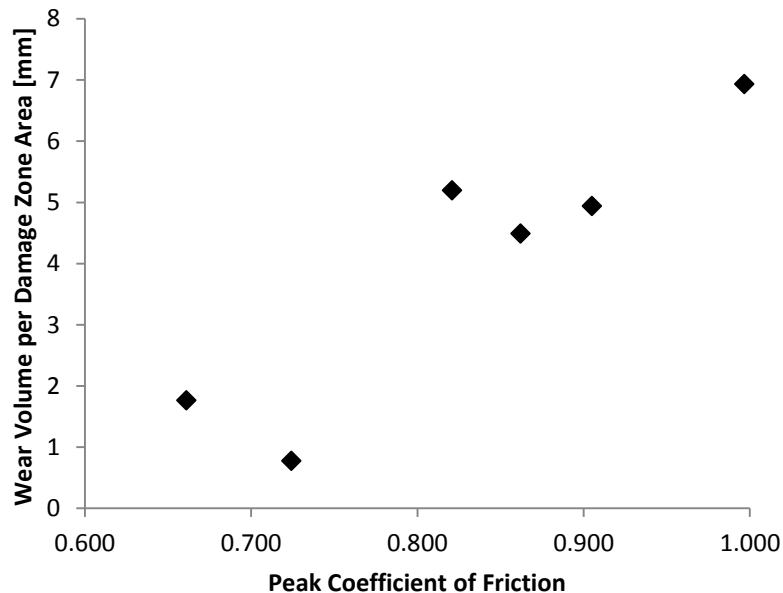


Figure 5.1. Variations of the calculated wear volume per area of damage zones with the measured peak friction.

5.1.3 Relation between the Wear and Roughness Evolution

Roughness evolution (PSD ratios) and wear volume were calculated using the optical measurements of the pre and post-shear surfaces at damage zones. The optical measurements and visual analysis both indicated that penetrative damage, caused to the sliding surface during shear, was responsible for the change in roughness and subsequently wear generation. The penetrative damage included fractures and pitting (caused by asperity plucking), which also relates to brittle fracture deformation. Figure 5.2 does not demonstrate any correlation between PSD ratios and the produced wear.

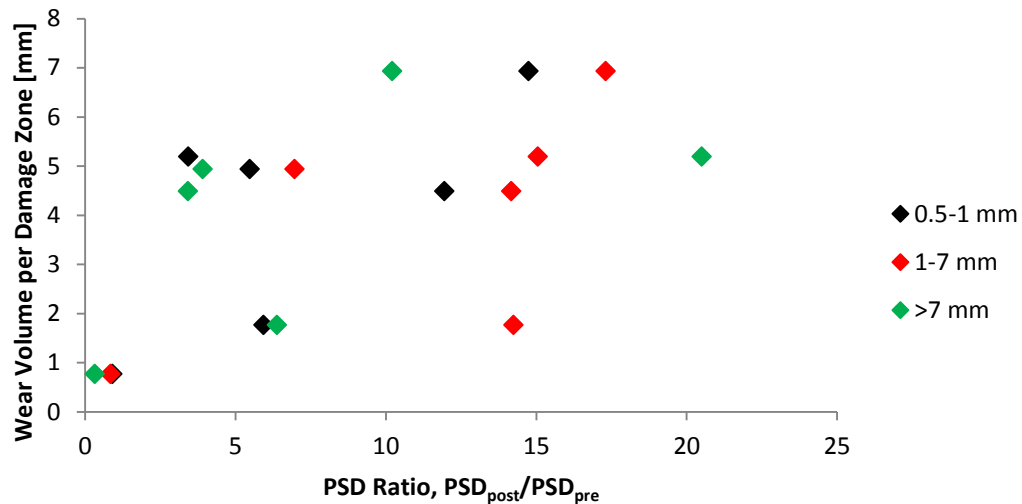


Figure 5.2. Relation between calculated wear volume per area with the PSD ratio (roughness evolution) of damage zones. PSD ratios are represented in three data sets, each one for a different wavelength range: black – 0.5 to 1 mm; red – 1 to 7 mm; and green – greater than 7 mm.

The wear-PSD ratio relation presented in Figure 5.2 is scattered, thus it is important to distinguish between wear and roughness evolution. Although roughness evolution and wear are part of the same phenomena, they do not necessarily scale with each other as roughness evolution relates to the mode of failure whereas wear is only a product of frictional sliding.

5.1.4 Relation between Roughness Evolution, Friction and the Stress Drop during Shear Displacement

The shear test results presented in section 4.1.1 exhibit a stress drop in shear stress between peak and residual stress conditions. The stress drop is referred to here as the shear stress drop ($\Delta\tau$) observed under the specific loading conditions of the present experiments. Maximum values of $\Delta\tau$ correlate with maximum values of friction coefficient and roughness evolution in experiment LN11 ($\sigma_n=12.5$ MPa). Minimum values of $\Delta\tau$ are calculated in experiment LN1 ($\sigma_n=5$ MPa), which exhibits a peak friction coefficient of 0.724 and PSD ratio below 1 that correspond with surface smoothing. The relation between the shear stress difference and the roughness evolution and the friction is plotted in Figure 5.3 below. It should be noted that data in this section does not include results from experiment LN6 as it exhibited anomalous values of peak friction coefficient (0.661) and stress drop (0.142 MPa).

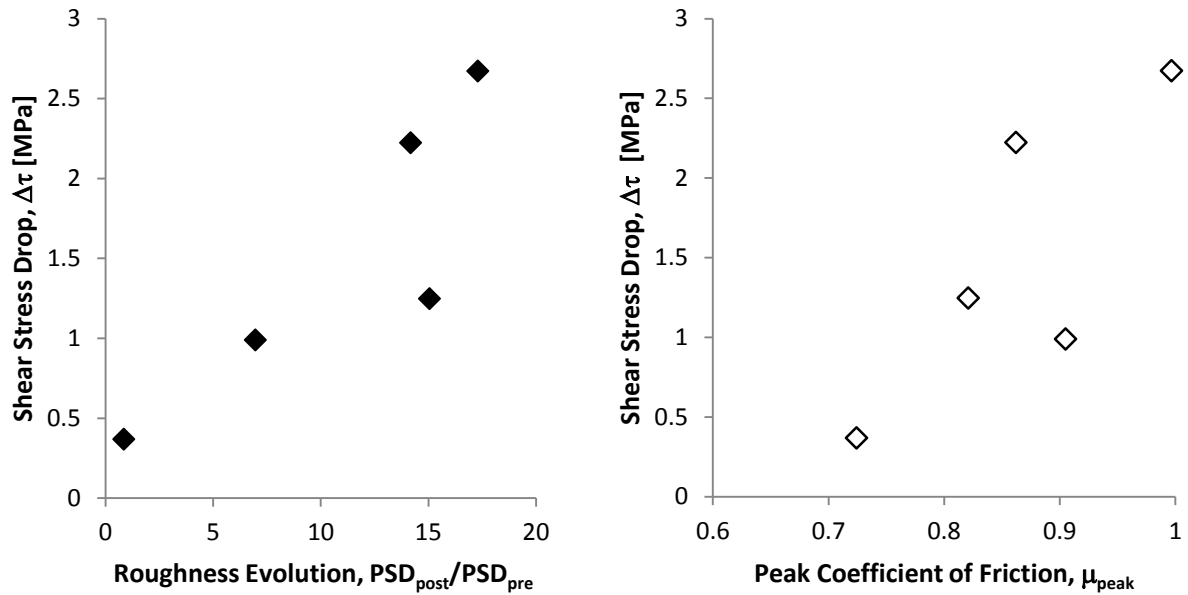


Figure 5.3. Left – variations of the shear stress drop with the calculated roughness evolution for wavelength range of 1-7 mm. Right – variations of the shear stress drop with the measured peak friction coefficient.

5.1.5 Mechanical Interpretation

The direct shear test results along with the roughness analysis reveal the roughness evolution of the rough, experimental faults. Under range of tested normal stress (5-15 MPa) the experimental slip surfaces exhibit an increase in roughness. Further visual and optical analyses indicate that the increase in roughness through shear is due to penetrative damage to the host rock. The plots in Figure 5.3 display a correlation between the shear stress drop and the roughness evolution and the peak coefficient of friction. Higher values of friction coefficient correspond to a more stable contact between two surfaces. As shear displacement increases more strain, and subsequently more strain energy, is accumulated on the stable contacts of the surfaces. The strain builds up with increased displacement until the asperities that make up the surfaces fail and yield. The mode of failure and degree relate to the roughness evolution, as higher PSD ratios correspond with fracturing and pitting of the original surface, thus causing the roughness to irreversibly change. Pitting and fracturing are manifestations of the released strain energy that accumulated on the once-stable high friction contacts. The shear stress drop is also related to the released strain energy during slip as seen in eq. (5.1) (Jaeger *et al.*, 2007). Therefore, the shear stress drop scales with both the roughness evolution and the coefficient of friction of rough surfaces.

$$\Delta E_{seismic} = M\Delta\tau/2G \quad (5.1)$$

Where $\Delta E_{seismic}$ is the radiated seismic energy during an earthquake, M is the seismic moment, $\Delta\tau$ is the stress drop and G is the shear modulus.

Because dilation is observed in all experiments during the initial stages of shear displacement, it is argued here that peak friction relates to the interlocking mechanism proposed by *Wang & Scholz (1994)*. Nevertheless, the interlocked asperities do not shear-off cleanly as in the *Wang & Scholz (1994)* model, but break partially or completely and form complex morphology.

The validity of this interpretation is examined by means of an analytical model in the next section (5.2).

5.2 Analytical Model

This chapter presents an analytical model (*Chester & Chester, 2000*) in order to support the suggested mechanisms that explain the results, as presented in chapter 4 and in section 5.1.5. As mentioned before, roughness evolution and wear generation from frictional sliding of rock surfaces relate to the stress distribution inside the rock medium and along the contacting interface. The analytical model results provide the principal stresses and their distribution inside an elastic medium (which represents the rock material in the experiments) and along the interface between two elastic bodies in relative motion. The *Chester & Chester (2000)* model is used as a conceptual framework for the stress distribution problem, inside and along the edges of an elastic medium, and not as a mean for calculating the specific stress distribution of each and every direct shear test in this study.

Chester & Chester (2000) presented an analytical solution for stress distribution on a wavy interface based on theory of elasticity. They solved this problem in two-dimensions, assuming plane-strain conditions, for a wavy interface between two elastic half-spaces (Figure 5.4). *Sagy & Brodsky (2009)* used *Chester & Chester (2000)* solution to analyze their field observations on natural fault surfaces. They concluded that slip on a fault with realistic geometry requires some degree of yielding of the host rock. A Matlab code based on *Chester & Chester (2000)* solution was written by *Sagy & Brodsky (2009)* and used for analyzing the stress distribution around asperities during shear. This code is modified here to model the stresses under loading conditions and material properties similar to those in the experiments. An analysis of the stress difference distribution is also added assuming the rock fails through brittle fracture and that the stress difference controls the damage evolution (*Ashby & Sammis, 1990*).

5.2.1 Model Assumptions

The model considers two elastic half-spaces separated by a wavy interface (Figure 5.4). The rough interface is represented as a sine function:

$$\zeta = A \sin(2\pi x/L) \quad (5.2)$$

Where A is the amplitude and L is the total nominal length of the interface.

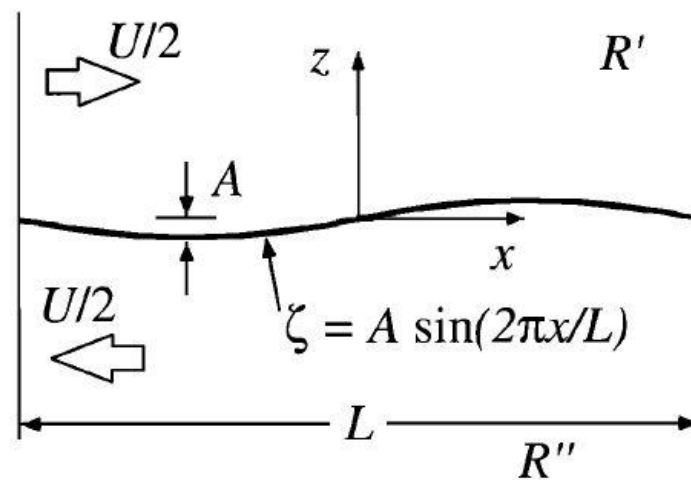


Figure 5.4. Initial geometry and boundary conditions of the model. R' and R'' denote the upper and lower half-spaces which are displaced relative to the interface by $U/2$ and $-U/2$, respectively. The coordinate system x and z is parallel and perpendicular, respectively, to the mean orientation of the interface. The wavy interface is of the length L and is in the form of a sine function given by ζ (Chester & Chester, 2000).

The half-spaces are subjected to far-field stresses and are displaced relative to each other according to a preset total displacement U . The code then calculates the principal stresses in the upper half-space (represented by a mesh grid) following the elastic equations in *Chester & Chester (2000)*. The code outputs include: distribution maps of the principal stresses (maximum and minimum) in the upper half-space; distribution map of the principal stress difference $\sigma_{\max} - \sigma_{\min}$ (*i.e.* $\Delta\sigma$) in the upper half-space; and a distribution map of the directional principal stress vectors (*i.e.* *stress trajectories*) in the upper half-space.

Six analyses were performed with an attempt to model the six direct shear tests. For each run (labeled A-F), input parameters were inserted manually according to the parameters measured at peak strength conditions during the actual experiments. These parameters include: normal stress and the peak coefficient of friction of the surface. Other input parameters were kept constant for all runs and are summarized in the following table:

Table 5.1. Constant input parameters in model

Parameter	Symbol	Value	Notes
Young's modulus	E	57 GPa	Davidesko, 2013
Poisson's ratio	ν	0.29	Davidesko, 2013
Stress ratio	k	0.4085	Assuming uniaxial strain
Nominal interface length	L	1	Unit length
Displacement	U	$1 \times 10^{-3}L$	
Roughness amplitude	A	$1.5 \times 10^{-2}L$	

The elastic parameters for the half-spaces were input according to measurements performed on the same limestone material by *Davidenko (2013)*. The far field stresses were set at a vertical (normal) and horizontal orientation relative to the mean sliding plane, the initial principal stress orientation in direct shear experiments. The stress ratio is defined as $k = \sigma_h / \sigma_n$ where σ_h is the horizontal far-field stress and σ_n is the normal (vertical) far-field stress. The value of k is estimated assuming uniaxial strain conditions where $k = \nu / (1 - \nu)$ (*Goodman, 1989*). This assumption is justified as no lateral strain of the half-space is permitted due to the high stiffness of the shear box steel which restrains any possible lateral expansion during normal compression of interface shear. The nominal interface length is set as unit length and the total displacement (U) and roughness amplitude (A) are set relative to L .

Because the solution assumes linear elasticity, it is crucial to set a displacement during which the material remains within the linear elastic regime and does not undergo inelastic, irreversible deformation. The total shear displacement (U) in the model was thus limited to $1 \times 10^{-3}L$ based on laboratory experiments on intact rock cylinders (*Davidenko, 2013*). For this amount of displacement the material undergoes a strain of:

$$\varepsilon = \frac{1 \times 10^{-3}L}{L} = 0.001 \quad (5.3)$$

Which is clearly within the elastic region (Figure 5.5).

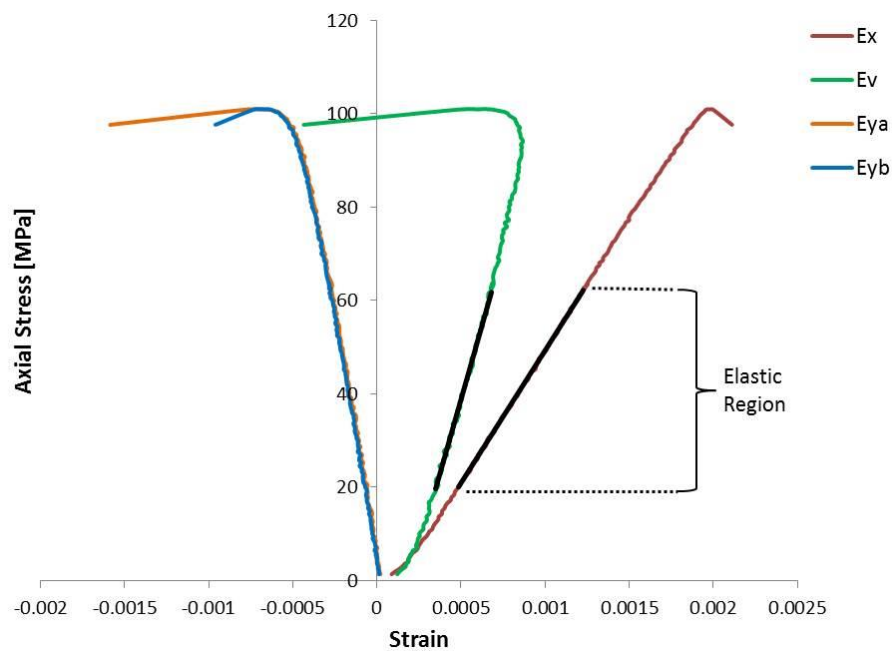


Figure 5.5. Stress-strain curves from a uniaxial test performed on studied limestone. Ex (red) refers to the axial stress-strain curve; Ev (green) refers to the axial stress-volumetric strain curve; Eya (orange) and Eyb (blue) refer to axial stress-radial strain curve in two transverse directions (*Davidenko, 2013*).

Along with the elastic strain measurements, material failure was tested for each run in order to further validate the elastic behavior of the upper half-space. The computed principal stress difference throughout the medium was checked with a Coulomb-Mohr type failure criterion for the intact rock material. This procedure insures that the displacement-induced principal stresses in the medium do not exceed its mechanical strength. In terms of principal stresses Coulomb-Mohr criterion may be expressed as (e.g., *Goodman, 1989*):

$$\sigma_1 = q_u + \sigma_3 \tan^2\left(45 + \frac{\phi}{2}\right) \quad (5.4)$$

Where σ_1 and σ_3 are the maximum and minimum principal stresses, respectively, q_u is the uniaxial compressive strength and ϕ is the angle of internal friction of the intact rock. Uniaxial compressive strength of the tested limestone used was 100 MPa (*Davidenko, 2013*). The angle of internal friction was assumed to be 35° which corresponds with the lower limit of typical values in limestone formations (*Goodman, 1989*). The cohesion of the limestone was estimated using the following relation (e.g., *Goodman, 1989*):

$$C = \frac{q_u(1 - \sin \phi)}{2 \cos \phi} \quad (5.5)$$

Where C is the cohesion of the rock, q_u is the uniaxial compressive strength and ϕ is the angle of internal friction of the intact rock. Thus, the cohesion of the limestone that was estimated to be 26.03 MPa (using the mentioned values for q_u and ϕ).

5.2.2 Results

Six runs, labeled A-F, were performed, each analogous to a direct shear experiment performed in the laboratory (see chapter 4). All model runs were computed using the same values of input parameters (section 5.2.1) except for the coefficient of friction of the interface and the normal stress. The coefficient of friction and normal stress were set according to the peak friction coefficient and the target normal stress measured in the corresponding experiments.

Select results are presented in Figure 5.6-Figure 5.9, for results from the other runs please refer to Appendix II. The space under the green line (contact interface) in the plots should be ignored as it does not depict the stresses on the lower, matching half-space.

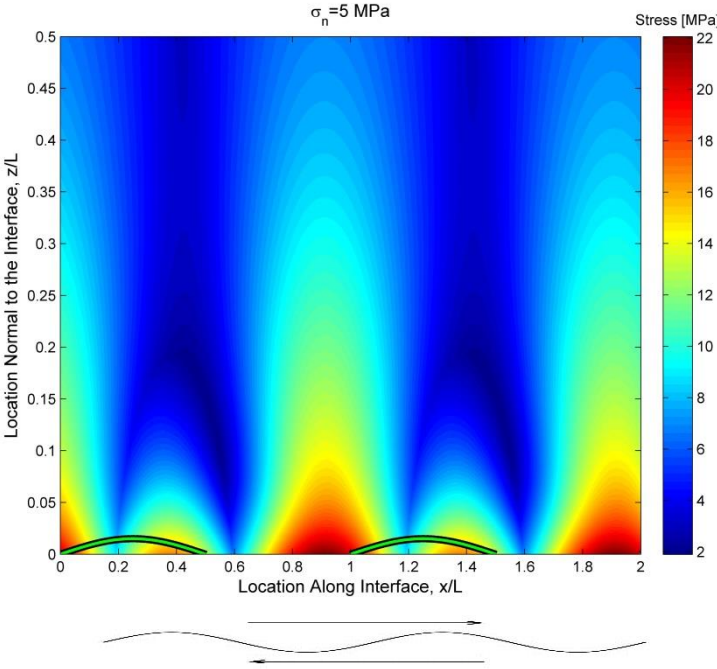


Figure 5.6. Maximum principal stress (σ_1) distribution throughout the upper half-space from run A, sheared under 5 MPa with a friction coefficient of 0.724.

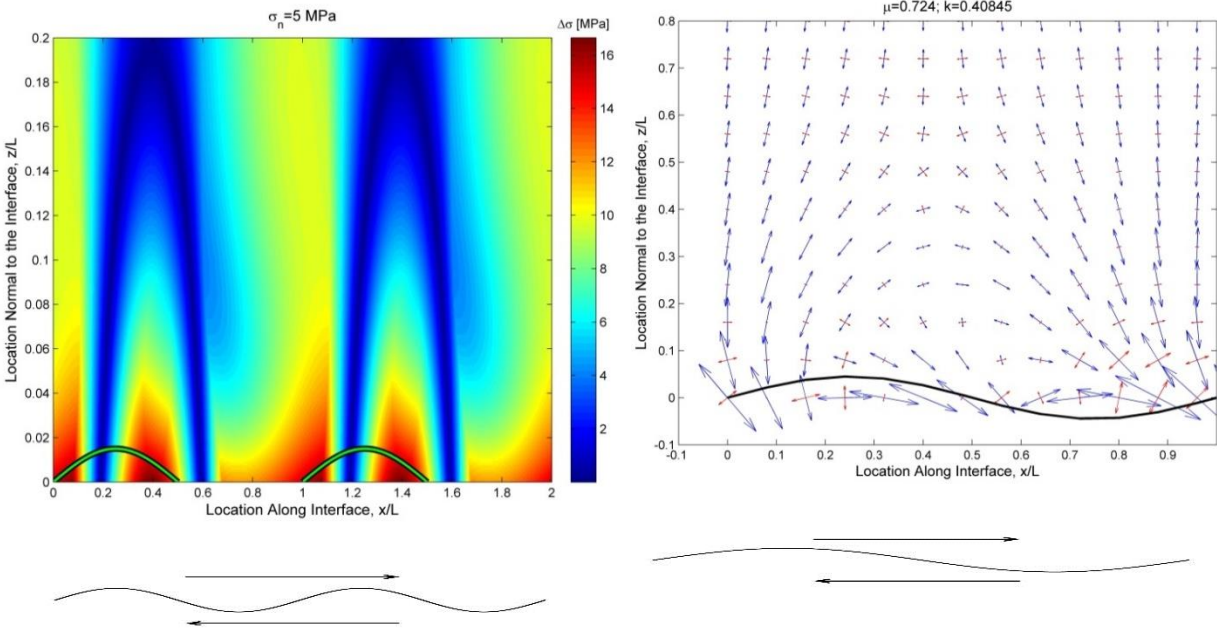


Figure 5.7. Stress distribution maps in the upper half-space for run A, sheared under 5 MPa with a friction coefficient of 0.724. Left panel – principal stress difference, the green wavy line in the bottom represents the interface geometry. Right panel – principal stress trajectories, the blue and red arrows represent the maximum and minimum stresses, respectively. The solid black wavy line in the bottom represents the interface.

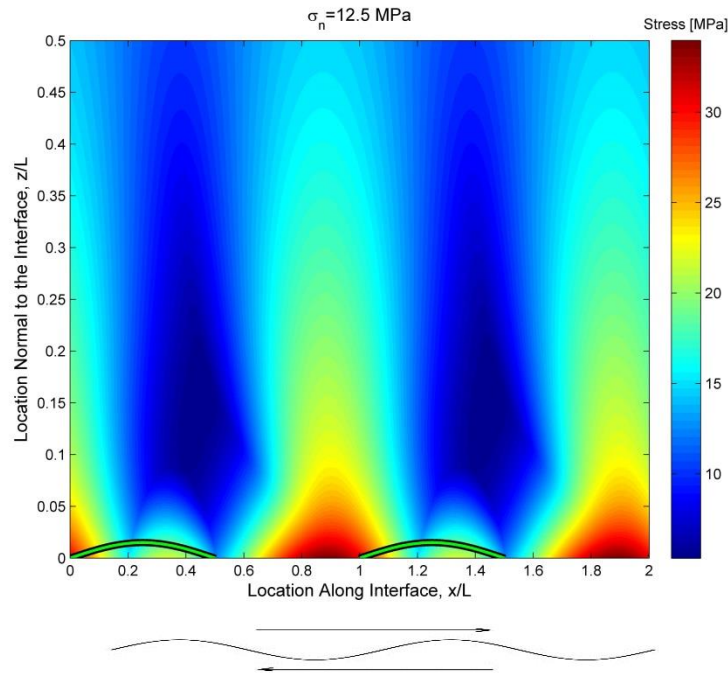


Figure 5.8. Maximum principal stress (σ_1) distribution throughout the upper half-space from run D, sheared under 12.5 MPa with a friction coefficient of 0.997.

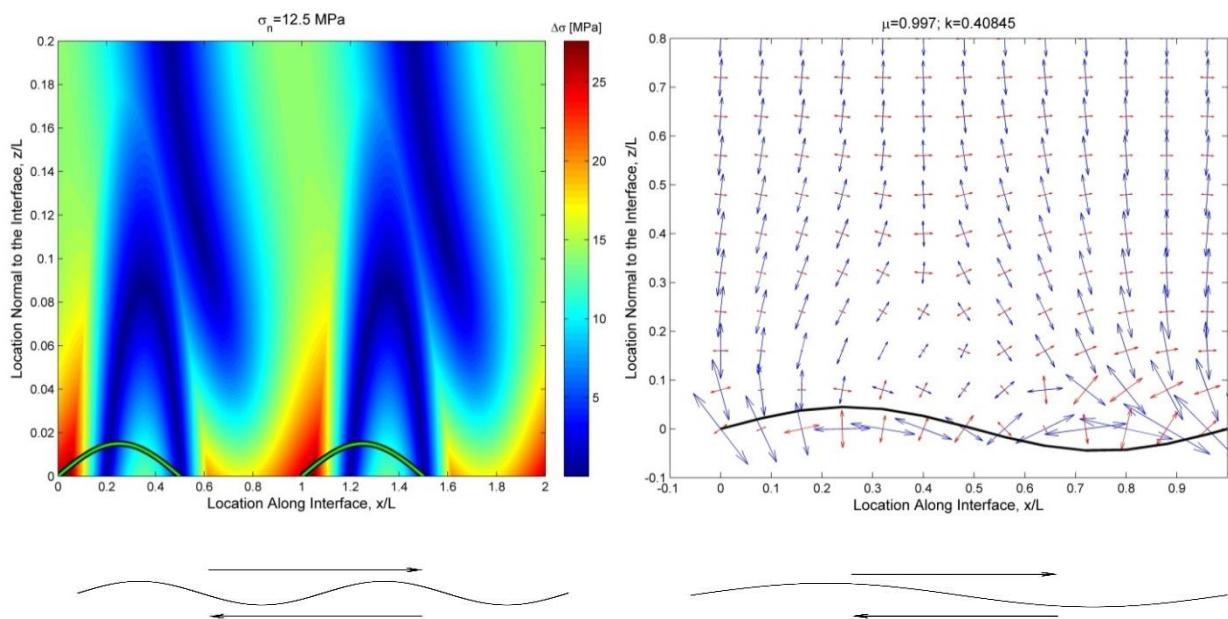


Figure 5.9. Stress distribution maps in the upper half-space for run D, sheared under 12.5 MPa with a friction coefficient of 0.997. Left panel – principal stress difference, the green wavy line in the bottom represents the interface geometry. Right panel – principal stress trajectories, the blue and red arrows represent the maximum and minimum stresses, respectively. The solid black wavy line in the bottom represents the interface.

The stress difference distribution throughout the material is affected by the interface geometry of the two half-spaces (Figure 5.7 and Figure 5.9). High values of stress difference ($\Delta\sigma$) were calculated close to the interface at restraining bends (at asperity flanks dipping to the left). Conversely, low values of $\Delta\sigma$ were calculated further away from the interface and close to the interface at releasing bends (at asperity flanks dipping to the right). Moreover, higher values of $\Delta\sigma$ were measured further away from the interface (towards $z/L=0.2$) for the

high normal stress runs ($\sigma_n > 10$ MPa) compared to the low normal stress runs ($\sigma_n < 10$ MPa). Figure 5.7 and Figure 5.9 (right panels) and also in Appendix II, exhibit the effect of the interface geometry on the stress trajectories throughout the material and close to the interface itself. The near-interface stress field is affected by the waviness of the interface. The stress trajectories follow the surface topography. The maximum principal stress trajectories (blue arrows in Figure 5.7 and Figure 5.9) dip into the interface at high to low angles relative to the mean orientation of the interface. Table 5.2 summarizes the results of the maximum stress difference from the model along with wear and roughness evolution data from the parallel experiments.

Table 5.2. Model results for runs A-F

Model Run	Parallel Experiment	Imposed σ_n [MPa]	Measured μ_{peak}	Modeled Maximum σ_1 [MPa]	Modeled Orientation of σ_1 [deg.]	Modeled Maximum $\Delta\sigma_{\text{max}}$ [MPa]
A	LN1	5	0.724	22.056	34.12	15.374
B	LN10	7.5	0.905	27.372	30.23	20.641
C	LN6	10	0.661	25.324	44.03	17.916
D	LN11	12.5	0.997	33.966	33.25	26.503
E	LN5	15	0.862	33.463	40.7	25.626
F	LN7	15	0.821	32.65	43.34	24.791

In Table 5.2, σ_n is the normal stress applied both in the experiment and the model run. μ_{peak} is the peak friction coefficient measured in each experiment and input in the model, σ_1 is the maximum principal stress calculated in the medium and $\Delta\sigma_{\text{max}}$ is the maximum principal stress difference calculated in the medium. The modeled orientation of σ_1 is relative to the mean sliding plane and in direction of imposed displacement.

5.2.3 Summary

An analytical model that computes the elastic stresses along a wavy surface during shear was applied to explain the experimental results and to further examine the relationship between surface roughness, damage, friction and stress. The results (Figure 5.6-6.6, Appendix II, Table 5.2) show that: (1) stress magnitude, near the contacting interface, increases as a function of imposed normal stress; (2) the maximum principal stress (σ_1) and maximum principal stress difference ($\Delta\sigma_{\max}$) increase as a function of the friction coefficient; and (3) principal stress trajectories are affected by the geometry of the contacting interface and dip relative to the mean sliding plane at medium-high angles (~ 30 - 50°).

The effects of the surface roughness and stress distribution on the mechanics of frictional sliding is further examined by comparing the model results with the experimental results. Table 5.3 summarizes the model results and the experimental results.

Table 5.3. Model results combined with experimental results.

Model Run	Parallel Experiment	Imposed σ_n [MPa]	Measured μ_{peak}	Modeled Maximum σ_1 [MPa]	Modeled Maximum $\Delta\sigma_{\max}$ [MPa]	Measured Wear Volume per Damaged Area [mm]	Measured PSD Ratio
A	LN1	5	0.724	22.056	15.374	0.776	0.838
B	LN10	7.5	0.905	27.372	20.641	4.939	6.954
C	LN6	10	0.661	25.324	17.916	1.768	14.238
D	LN11	12.5	0.997	33.966	26.503	6.933	17.303
E	LN5	15	0.862	33.463	25.626	4.492	14.167
F	LN7	15	0.821	32.65	24.791	5.196	15.046

Where σ_n is the normal stress applied both in the experiment and the model run, μ_{peak} is the peak friction coefficient measured in each experiment and input in the model, σ_1 is the maximum principal stress calculated in the medium, $\Delta\sigma_{\max}$ is the maximum principal stress difference calculated in the medium. Wear volume and PSD ratios (mean values referring to wavelength range of 1-7 mm) were measured from each experiment.

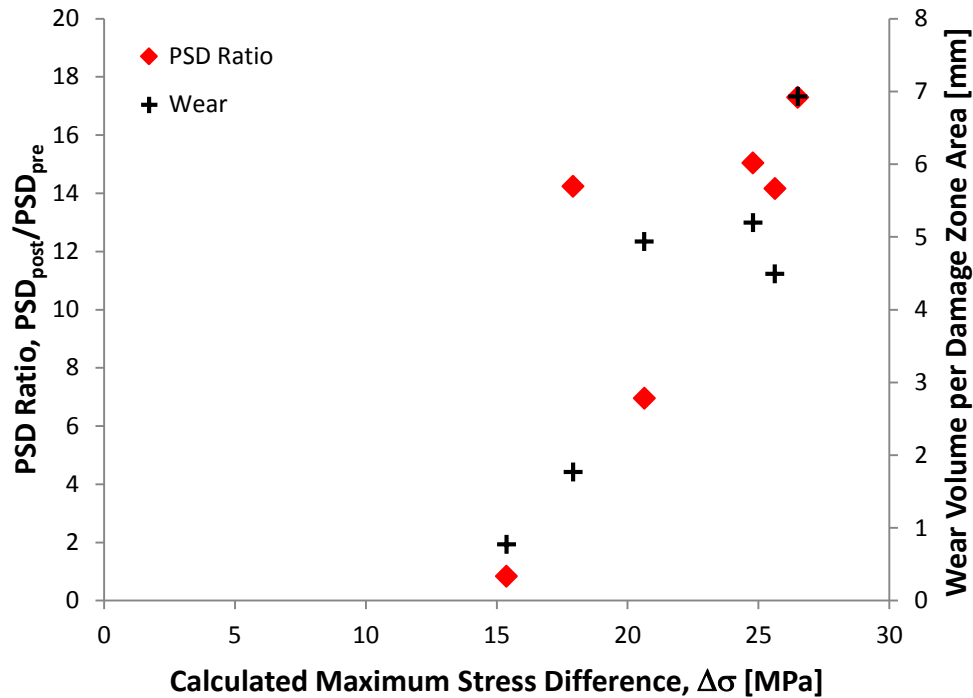


Figure 5.10. Relation between the calculated maximum stress difference (modeled) and the measured PSD ratio (red diamonds) and measured wear (black open squares). Note the PSD ratio series (red diamonds) outlier at (12,14.2) which represents the data used from experiment LN6 ($\sigma_n=10$ MPa). The friction coefficient for this sample was significant lower compared to the other experiments ($\mu=0.661$).

The combined model-experimental results (Table 5.3, Figure 5.10) exhibit a correlation between the calculated maximum stress difference ($\Delta\sigma$) and the PSD ratio (roughness evolution) along with the generated wear volume per area of damage zones. The shear-induced stress difference is an important factor in rock mechanics as it relates to Coulomb-Mohr failure theory and to damage evolution (Ashby & Sammis, 1990). According to the theory, mechanical failure in rocks or soils takes place along a plane due to the shear stress acting along that plane. The Coulomb-Mohr failure criterion can also be expressed in terms of principal stress, where failure occurs once a certain limit of principal stress difference ($\Delta\sigma$) is surpassed (Jaeger *et al.*, 2007). The model predicts that for a rough, wavy interface, small displacements cause stress amplification in the material and along the contacting interface. The magnitudes and orientations of the amplified principal stresses can explain the failure mechanism of the penetrative damage that is observed in the direct shear experiments. Brittle fractures can propagate from the interface into the material as stress, and consequently principal stress difference, builds up on the contacting interface and exceeds the strength limit of the host rock. Hence, the model supports the idea that surfaces become rougher due to penetrative damage and better relate to friction along an interface rather than imposed normal stress levels.

6 Discussion

Direct shear experiments coupled with geometrical measurements reveal the roughness evolution of rough, experimental fault surfaces. The results suggest that surface roughness increases with applied normal stress during shear displacement. Visual analysis of the wear particles and the sheared surfaces indicate that surface roughening is possible through shear by penetrative damage to the host rock.

The experimental and modeled results are here by discussed in relation to the mechanics of faults both in the laboratory and in the field. While the results in the current study suggest that the roughness of the experimental fault surfaces increases with shear, *Davidenko et al. (2014)* report a decrease in roughness with shear. The difference between this study and the *Davidenko et al. (2014)* study is attributed to the different range of normal stress studied in each case. Where *Davidenko et al. (2014)* conducted direct shear tests under a normal stress of 2 MPa, while in the current study normal stress levels ranges between 5-15 MPa.

6.1 Statistical Self-Affinity of Experimental Fault Surfaces

Power spectral density (PSD) and root mean square (RMS) methods were applied to quantify the surface roughness of experimental fault surfaces in limestone. The post-shear surfaces were fitted well by a power-law curve along the range of 10^{-1} -10 mm (Figure 4.18-Figure 4.23) and therefore suggest that the surfaces exhibited self-affine fractal geometry, parallel to slip direction, with Hurst exponent (H) values of about 0.8 (Table 4.5). The range of the calculated H values was quite large in comparison to the values reported in previous works (e.g. *Brown & Scholz, 1985; Bouchaud et al., 1990; Chen & Spetzler, 1993; Power & Durham, 1997; Amitrano & Schmittbuhl, 2002*). This range was probably a product of the relative short length scale (10^{-1} to 10 mm) over which the H values were calculated. Furthermore, the method that was used to create the experimental surfaces (section 3.1) could have also accounted for the range of the calculated H values as equal-roughness surfaces were impossible to reproduce through four-point bending.

On the other hand, the geometry of some of the pre-shear experimental surfaces was not self-affine along the measured range. At scales smaller than 0.8 mm the PSD-wavelength curve deviates from the typical form creating a “bend” in the curve where the power of PSD function $\beta \rightarrow 0$ (hence the Hurst exponent $H \rightarrow 0$ as well). Such bending might relate to white noise in the spectrum. The bend is noticeable in both the pre and post-shear curves

(Figure 6.1), but around different wavelengths. This bend is a product of the material grain size, because the PSD represents the roughness of the entire surface statistically, it reflects the mean parameters of the surface. At pre-shear PSD curves, the bend is located around 0.4 mm wavelength, which corresponds to the mean grain diameter of the tested limestone (*Davidenko, 2013*). At post-shear curves the bend “moves” around smaller wavelength, this is attributed to the roughness evolution in which the grains themselves break due to shear. Thus, the roughness evolution at wavelengths smaller than the average grain size, reflect damage at a sub-grain scale. This scale differs from the scale of topography because of the variability of the grains themselves in terms of sedimentary source, shape, size and mineralogy. This grain variability should also be present, if not amplified, in igneous rocks as well where the rock matrix is composed of different minerals. Hurst exponent of 0.8 is assumed to be a universal value for fractures (*Bouchaud et al., 1990*). The results presented here demonstrate evolution of non-fractal surfaces to fractal surfaces with a typical exponent through shear.

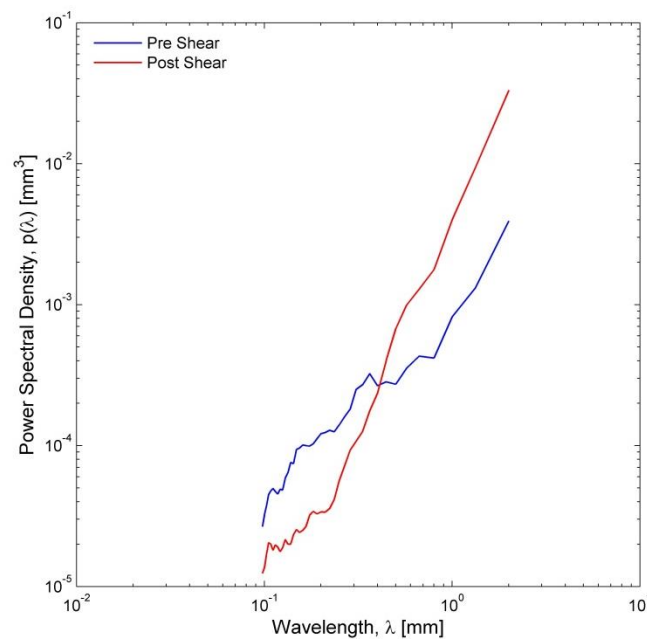


Figure 6.1. PSD roughness functions for sample LN5, sheared under 12 MPa. Both the pre-shear (blue) and post-shear (red) curves display a power law behavior at the long wavelengths. The deviation from this form, referred to as the “bend”, is clearly noticeable for the pre-shear curve at wavelengths around 0.4 mm and for the post-shear curve at wavelengths around 0.15 mm. Note that at sub-grain wavelengths ($\lambda < 0.4$ mm) the surface smoothens, this is attributed to the grains themselves and do not represent the surface topography.

6.2 The Relationship between Stress, Friction, Roughness and Wear

The correlations given in chapter 5 and section 4.2 present complex relations between stress, friction, roughness and wear. Normal stress and roughness affect friction, which in turn correlates to wear. Wear is the product of roughness evolution that also relates to the stress drop observed during frictional sliding. These correlations raise questions regarding the relations between friction, applied stresses, roughness and wear production.

6.2.1 Friction and Wear of Rough Surfaces

Bowden & Tabor (1950) suggested that surfaces connect and interact through asperities as all surfaces exhibit some degree of roughness. *Wang & Scholz (1994)* proposed that during frictional sliding the surfaces interact through the asperities by three mechanisms: interlocking, riding-up (gliding) and ploughing. Experimental results in this study suggest that for rough, self-affine surfaces, the interlocking and riding-up are the dominant mechanisms. This is noticeable from the dilatational behavior of the surfaces during shear displacement (section 4.1.1) and from the visual-optical analysis of the post-shear surfaces (section 4.2.3). *Wang & Scholz (1994)* also proposed a model for the effect of normal stress on the asperity contacts (Figure 6.2). The *Wang & Scholz (1994)* model introduced a new parameter, h , the interlocking distance. When normal stress is applied across the contacting interface, the interlocking distance grows, this analogues the increase in real contact area. If the interlocking distance surpasses a critical value, h_c , the asperities lock and shear off, for values of h below the critical value, asperities deform elastically and slide over each other (gliding or riding up mechanisms). The model predicted that an increase in normal stress, initial surface roughness and displacement correlates to an increase in wear production which is also suggested by *Queener et al. (1965)* model for frictional sliding. Moreover, the *Wang & Scholz (1994)* model supports the two-stage wear production-displacement function proposed by *Queener et al. (1965)*.

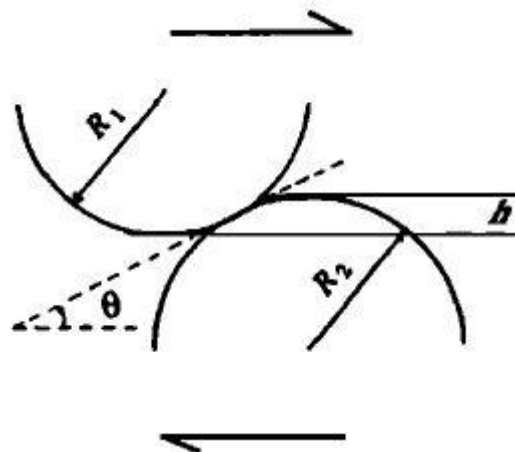


Figure 6.2. Schematic diagram for an interlocking contact between two spherical asperities. Arrows indicate the relative shear sliding, R_1 and R_2 are the radii of two asperities, h is the interlock distance of two contacting asperities, and θ is the contact angle (*Wang & Scholz, 1994*).

However, the results in section 4.3 and the correlation in section 5.1.2 suggest that wear production better relates to the peak friction coefficient rather than imposed normal stress. Although friction-wear correlation seems intuitive, it is not true for all materials as studies in material sciences indicate (e.g. Freeman et al., 2000). Friction is proportional to normal force,

when normal stress is applied on two bodies the real area of contact between them grows (Bowden & Tabor, 1950; Archard, 1953). Consequently, more wear is produced during frictional sliding under increased normal stress (Queener *et al.*, 1965; Wang & Scholz, 1994). However, most of the research in frictional sliding and wear involve slip on smooth, planar surfaces that are only rough in the small scales (e.g., Bowden & Tabor, 1950; Archard, 1953; Queener *et al.*, 1965; Biegel *et al.*, 1992; Wang & Scholz, 1994; Lee & Rutter, 2004; Hsu & Shen, 2004; Rao & Das, 2011; Hirose *et al.*, 2012). More recent studies suggest that the roughness of natural rock surfaces in faults affects the local, near-interface stress field (Candela *et al.*, 2011; Goebel *et al.*, 2013). Moreover, Fang & Dunham (2013) suggest that roughness adds an additional shear resistance, termed "roughness drag", which along with the pure frictional resistance implies a complex frictional behavior of rough surfaces. Therefore, it is argued here that not only does the friction depend on the normal stress, but also on the local stress field at the vicinity of the contact interface and the roughness itself. Suggesting that for rough surfaces, wear relates better to friction than normal stress.

6.2.2 Damage-Roughness-Stress Relations

Observations from the shear experiments indicate that penetrative damage, sustained by the rock during shear displacement, is the mechanism responsible for the measured increase in roughness. Sagy & Brodsky (2009) suggest that slip on surfaces with realistic geometry, requires internal yielding of the host rock. As said before, it is assumed that asperities from opposite surfaces interact with each other by the interlocking and riding-up mechanisms (Wang & Scholz, 1994; Scholz, 2002). However, the Wang & Scholz (1994) model does not account for the mode of failure but rather assumes that the asperities shear-off. The observations in this study indicate that at low normal stresses (5 MPa) the asperity summits decapitate (partially or completely), which decreases roughness. At high normal stresses (≥ 7.5 MPa) the surfaces undergo extensive damage, which increases roughness. Other studies exhibit similar results; Cho *et al.* (2008) show that a damage zone grows around a rough sliding plane in synthetic rock during direct shear experiments. This damage zone includes shear fractures, tensile fractures and Riedel shears that propagate to the surrounding host rock (e.g., Caine *et al.*, 1996). Davidesko *et al.* (2014) show that rough, self-affine limestone surfaces smooth when sheared under low normal stress (2 MPa) with an increase in shear displacement (5-15 mm). Boneh *et al.* (2014) show that ground rock surfaces, become rougher through pitting, fracturing and plucking when sheared under increasing normal stress and shear displacements smaller than 50 mm. Boneh *et al.* (2014) also show that for shear displacements greater than 50 mm, the surfaces smooth.

The idea that the geometry of a surface affects the local stress field during shear is tested in section 0 with an analytical model introduced by *Chester & Chester (2000)*. The results of the model suggest that surface geometry alters the near-interface stress field both in direction (stress trajectories) and in magnitude. Stress amplifications and related principal stress differences arise in the material during shear displacement. The stress amplification (stress concentrations) and stress difference correlate to the friction on the surface. Moreover, areas of amplified stress and stress difference propagate into the host material beyond the amplitude of the asperities. Along with the stress trajectories, which dip into the material at medium-high angles (30-50°) relative to the mean sliding plane, penetrative damage is likely, assuming the rock fails according to the Coulomb-Mohr failure criterion. The modeled orientation of the maximum principal stress along with the high stress and stress difference levels mentioned before, agree with the occurrence and orientation of the cracks measured on the post-shear surfaces. These cracks reflect the local stress field near the sliding plane during slip (*Chester & Chester, 2000*).

Chester & Chester (2000) display the same friction-roughness-stress distribution relation in their runs, suggesting that high friction corresponds with a more stable contact and less perturbation of the near-interface (fault) stress field. Therefore, the geometry of the interface plays a double role; it distributes stress unevenly in the material and along the contacting interface and affects the friction coefficient, which in turn amplifies the far-field stresses in the vicinity of the sliding interface. The stable high-friction contact can therefore occupy greater strain with increased displacement. These stable contacts "accumulate" more strain energy, which accompanied with high stress difference levels, yield the host rock which causes the stored elastic energy to release at once. The correlation between the stress drop (shear stress drop, $\Delta\tau$) and the roughness evolution (section 5.1.4) emphasizes the relation between the friction, roughness and stress. Maximum friction is measured in the experiment (LN11) that also displays maximum roughening. Surface roughening correlates to greater stress drop, as more strain energy is focused towards fracturing and plucking. Furthermore, it is argued here that under the studied normal stresses the friction across a surface is dependent on the roughness of the surface, as indicated by *Byerlee (1978)*, and thus affects the normal stress-peak friction results (Figure 4.10) by introducing more scatter.

The effects of the geometry are further examined by comparing the model results (chapter 0, Appendix II) to a reference model (Figure 10.9 in Appendix II).

The reference model is exactly alike the runs described in chapter 0 except for the interface geometry. The reference model depicts a perfectly smooth surface sheared under an imposed normal stress of 12.5 MPa. All input parameters for this model follow the corresponding values in Table 5.1 (section 5.2.1) except for roughness amplitude of zero. The result (Figure 10.9) indicates that the stresses and stress differences are uniform throughout the material and along the interface. The stress trajectories in the material do not deviate from the imposed far-field stresses.

Thus, it is suggested that the near-interface stress field dictates the mode of failure of the asperities and wear production during sliding. The friction coefficient, which is dependent on the material properties and the surface geometry, echoes the local stress field near the interface and by this relates to the wear production. Strain energy accumulated on the rough, high-friction contacts releases through fracturing and plucking, which in turn, correspond to greater roughness evolution.

6.3 Relations between the Experimental Results and Field Observations

It is accepted here that the penetrative damage, which exceeds the scale of the initial surface roughness, is the cause for the increase in surface roughness in the experimental faults. By integrating the experimental and model results of the current study with the results of *Sagy & Brodsky (2009)* it is apparent that what controls the observed damage around faults (both experimental and natural) is surface roughness (amplitude to wavelength ratio), normal stress and amount of slip. The damage zones around natural faults are examined here with a reference to the observed damage in the experimental faults. The basis of such a comparison is due to the fact that natural faults are non-planar surfaces (e.g., *Brown & Scholz., 1985; Power et al., 1988; Scholz, 2002; Renard et al., 2006; Sagy et al., 2007; Candela et al., 2009*). The ratio between the roughness amplitudes and wavelengths in the experimental faults is in the range for natural faults (10^{-2} - 10^{-4} , *Power et al., 1988*). Furthermore, the roughness amplitudes to wavelength ratio is greater or similar to the slip to rupture length ratio both calculated in the experimental faults (10^{-2}) in current study and in natural faults (10^{-5} , *Scholz, 2002*).

The experimental damage zones in the current study share a resemblance to damage zones observed in natural faults. The experimental surfaces produce two types of wear material (section 4.3), pulverized rock and rock fragments. Pulverized rock particles account for a fraction of the total wear and relate to abrasive wear, perhaps through local hardness differences between the contacting surfaces. Rock fragments make up the bulk of the

produced wear, these wear products form by brittle fracture. Upon removal, rock fragments leave pits, holes and fractures in the host rock. The fractures propagate into the host rock at different orientations that reflect the local stress field near the sliding interface during shear displacement, as discussed in section 6.2.2. Natural faults are typically zones of deformed rock with a complex internal structure and three-dimensional geometry (Wibberley *et al.*, 2008). Fault zones are characterized by two structural components: a damage zone and a fault core (Caine *et al.*, 1996; Ben-Zion & Sammis, 2003; Micarelli *et al.*, 2006; Faulkner *et al.*, 2010). Fault damage zones include fault-related fracture sets, veins and minor faults over a wide range of length scales. Little or no offset is accumulated by the minor faults with the majority of the displacement being localized in the central slip surface (Micarelli *et al.*, 2006). This is also observed on the experimental slip surfaces where the entire displacement is carried on the main slip plane. Other structures such as extensional fractures, synthetic faults and wing cracks (Figure 6.3) resemble the traces of the penetrative damage on the post-shear experimental surfaces. These structures, categorized as “wall damage”, can result from frictional attrition as slip builds up on a fault (Kim *et al.*, 2004). Similar to the experimental damage zones, density of fractures in damage zones surrounding faults decrease with distance from the main sliding plane (Sagy & Brodsky, 2009; Faulkner *et al.*, 2010). The spatial distribution of the damage in natural fault zones relates directly to the near-interface stress field, which is suggested to be the key in the roughness evolution of the experimental surfaces during shear.

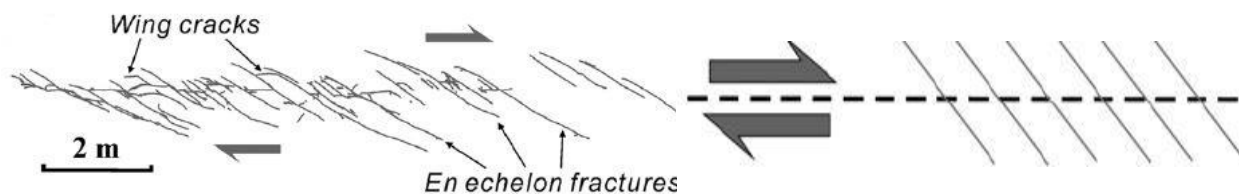


Figure 6.3. Examples of wall damage zones; Left – extension fractures around a strike-slip fault trace. Right – Schematic illustration of extensional fractures (Kim *et al.*, 2004).

The internal structure of fault zones and its formation is important for understanding both the permeability and flow in rocks and the seismogenic behavior of faults. The fault roughness and its development controls the nucleation, propagation and arrest of earthquakes (Lay *et al.*, 1982; Aki, 1984; Scholz, 2002; Wibberley *et al.*, 2008). Thus, further experimental and field research is needed for the understanding of the role and effects of the geometry of faults.

7 Conclusions

1. Rough limestone surfaces subjected to normal and shear stresses exhibit damage zones where the surface geometry changes through shear. Under the tested range of normal stress, the roughness of the damage zones increased with applied normal stress.
2. Surface roughness increased through a penetrative damage mechanism that reflected the local stress field in the vicinity of the sliding interface. Therefore, loading configuration and the initial geometry control the fracturing-shearing process. The maximal resistance to shear, which relates to the near-interface stress field, dictated the amount of damage sustained by the host rock and consequently the produced wear during frictional sliding.
3. The roughness evolution of the experimental surfaces relates to the stress drop experienced during direct shear experiments as they both reflect (along with other processes such as heat, grain rotations etc.) the sudden release of the elastic energy accumulated during the initial stage of sliding. A portion of the accumulated elastic energy is channeled towards breaking the host rock, thus creating damage. The roughness evolution and normal stress levels relate to the mode of failure of the host rock and its intensity during frictional sliding, assuming failure through intact asperity material follows the Coulomb-Mohr failure criterion. Failure of the asperities was possible due to the alteration of the near-fault stress field, which itself was a product of normal stress, amount of slip and surface roughness.
4. The roughness of experimental limestone surfaces evolves through shear thus changing the geometry of the surfaces from non-fractal to a self-affine fractal. The Pre-shear experimental rough limestone surfaces do not exhibit self-affine geometry because of the size of the grains that make up the surface. It is only after shear, under the tested range of normal stress, that the surface geometry evolves to a fractal self-affine geometry with a Hurst exponent value of ~ 0.8 . The change from non-fractal pre-shear geometry to fractal post-shear geometry is attributed to the increase in surface roughness which includes breaking the grains themselves.
5. Damage zones which were generated during shear of rough, interlocked surfaces in the laboratory share structural similarity to damage zones around natural faults observed in the field. The experimental faults also resembled natural faults as they exhibited surface roughness (amplitude to wavelength ratio) which is greater or equal to the amount of slip

during a single event. Thus, experimental research of rough surfaces with realistic geometry is key to the understanding of the mechanics of faults and their evolution in the upper crust.

8 References

- Aki, K. (1984). Asperities, barriers, characteristic earthquakes and strong motion prediction. *J. Geophys. Res.*, Vol. 89, No. B7, 5867-5872.
- Amitrano, D., & Schmittbuhl, J. (2002). Fracture roughness and gouge distribution of. *J. of Geophys. Res.*, 107 (B12), 2375, doi:10.1029/2002JB001761.
- Archard, J. F. (1953). Contact and rubbing of flat surfaces. *Journal of Applied Physics*, Vol. 24, Num. 8, 981-988.
- Ashby, M. F., & Sammis, C. G. (1990). The damage mechanics of brittle solids in compression. *Pure and Applied Geophysics*, 133(3), 489-521.
- Barton, N. (1976). Rock Mechanics Review: The Shear Strength of Rock and Rock Joints. *International Journal of Rock Mechanics, Mining Science and Geomechanics Abstracts*, Vol. 13, 255-279.
- Barton, N. R., & Choubey, V. (1977). The shear strength of rock joints in theory and practice. *Rock Mechanics 10 (1-2)*, 1-54.
- Ben-Zion, Y., & Sammis, C.G. (2003). Characterization of fault zones. *Pure and Applied Geophysics*, 160, 677-715.
- Biegel, R. L., Wang, W., Scholz, C. H., Boitnott, G. N., & Yoshioka, N. (1992). Micromechanics of rock friction 1. Effects of surface roughness on initial friction and slip hardening in westerly granite. *J. Geophys. Res.* 97, 8951-8964.
- Biran, O. (2011). *Rate and state friction experiments in direct shear*. Beer Sheva, IL: Ben Gurion University of the Negev.
- Boneh, Y., Chang, J., Lockner, D. A., & Reches, Z. (2014). Fault Evolution by Transient Processes of Wear and Friction. *Pure and Applied Geophysics*, Vol. 171, Issue 11, 3125-3141.
- Bouchaud, E., Lapasset, G., & Planès, J. (1990). Fractal dimension of fractured surfaces: A universal value? *Europhys. Lett.*, 13, 73-79.
- Bowden, F. P., & Tabor, D. (1950). *The Friction and Lubrication of Solids*. Oxford: Oxford University Press.

- Brace, W. F. & Byerlee, J. D. (1966). Stick-slip as a mechanism for earthquakes. *Science*, 153(3739), 990-992.
- Brace, W. F., Paulding, B. W., & Scholz, C. H. (1966). Dilatancy in the fracture of crystalline rocks. *J. Geophys. Res.*, 71(16), 3939-3953.
- Brodsky, E. E., Gilchrist, J. J., Sagy, A., & Collettini, C. (2011). Faults smooth gradually as a function of slip. *Earth and Planetary Science Letters*, Vol. 302, 185-193.
- Brown, S. R., & Scholz, C. H. (1985). Broad Bandwidth Study of the Topography of Natural Rock Surfaces. *Journal of Geophysical Research*, Vol. 90, No. B14, 12,575-12,582.
- Byerlee, J. (1978). Friction of Rocks. *Pure and Applied Geophysics*, Vol. 116, 615-626.
- Byerlee, J. D. (1967). Frictional characteristics of granite under high confining pressure. *J. of Geophys. Res.* 72(14), 3639-3648.
- Caine, J. S., Evans, J. P., & Forster, C. B. (1996). Fault zone architecture and permeability structure. *Geology*, 24(11), 1025-1028.
- Candela, T., Renard, F., Bouchon, M., Brouste, A., Marsan, D., Schmittbuhl, J., & Voisin, C. (2009). Characterization of fault roughness at various scales: Implications of three-dimensional high resolution topography measurements. *Pure Appl. Geophys.*, 166, 1817-1851, doi:10.1007/s00024-009-0521-2.
- Candela, T., Renard, F., Bouchon, M., Schmittbuhl, J., & Brodsky, E. E. (2011). Stress drop during earthquakes: effect of fault roughness scaling. *Bull. seism. Soc. Am.* 101(5), 2369-2387.
- Candela, T., Renard, F., Schmittbuhl, J., Bouchon, M., & Brodsky, E. (2011). Fault slip distribution and fault roughness. *Geophysical Journal International*, Vol. 187, 959-968.
- Chen, G., & Spetzler, H. (1993). Topographic characteristics of laboratory induced shear fractures. *Pure Appl. Geophys.*, 140, 123-135.
- Chen, X., Madden, A. S., Bickmore, B. R., & Reches, Z. E. (2013). Dynamic weakening by nanoscale smoothing during high-velocity fault slip. *Geology*, 41(7), 739-742.
- Chester, F.M., & Chester, J. S. (2000). Stress and deformation along wavy frictional faults. *Journal of Geophysical Research*, v. 105, 23421-23430.

- Chester, F.M., Evans, J.P., & Biegel, R.L. . (1993). Internal structure and weakening mechanisms of the San Andreas fault. *J. Geophys. Res.*, *98*, 771-786.
- Cho, N., Martin, C. D., & Segol, D. C. (2008). Development of a shear zone in brittle rock subjected to direct shear. *International Journal of Rock Mechanics and Mining Sciences*, *45*(8), 1335-1346.
- Coulomb, C. A. (1781). Théorie des machines simples, en ayant égard au frottement de leurs parties, et a la roideur des cordages. *Mem. Math. Phys.*, *X*, 161-342.
- Davidesko, G. (2013). *Evolution of Surface Roughness Through Shear*, M.Sc. Thesis. Beer-Sheva, Israel: Ben-Gurion University of the Negev.
- Davidesko, G., Sagy, A., & Hatzor, Y. H. (2014). Evolution of slip surface roughness through shear. *Geophys. Res. Lett.*, *41*, 1492-1498, doi:10.1002/2013GL058913.
- Deere, D. U., & Miller, R. P. (1966). *Engineering classification and index properties of rock*, Technical Report No. AFNL-TR-65-116. Albuquerque, NM: Air Force Weapons Laboratory.
- Dieterich, J. H. (1979). Modeling of rock friction 1. Experimental results and constitutive equations. *Journal of Geophysical Research*, *84*(B5), 2161-2168.
- Dunham, E. M., Belanger, D., Cong, L., & Kozdon, J. E. (2011). Earthquake ruptures with strongly rate-weakening friction and off-fault plasticity, Part 1: Planar faults. *Bulletin of the Seismological Society of America*, *101*(5), 2296-2307.
- Fang, Z., & Dunham, E. M. (2013). Additional shear resistance from fault roughness and stress levels on geometrically complex faults. *Journal of Geophysical Research: Solid Earth*, Vol. *118*, doi:10.1002/jgrb.50262, 3642-3654.
- Faulkner, D. R., Jackson, C. A. L., Lunn, R. J., Schlische, R. W., Shipton, Z. K., & Wibberley, C. A. J. (2010). A review of recent developments concerning the structure, mechanics and fluid. *J. of Structural Geology*, *32*, 1557-1575.
- Freeman, M. E., Furey, M. J., Love, B. J., & Hampton, J. M. (2000). Friction, wear and lubrication of hydrogels as synthetic articular cartilage. *Wear*, *241*, 129-135.
- Freund, L. B. (1998). *Dynamic Fracture Mechanics*. Cambridge, GB: Cambridge University Press.

- Goebel, T. H. W., Candela, T., Sammis, C. G., Becker, T. W., Dresen, G., & Schorlemmer, D. (2013). Seismic event distribution and off-fault damage during frictional sliding of saw-cut surfaces with pre-defined roughness. *Geophysical Journal International*, *196*, 612-625.
- Goodman, R. E. (1989). *Introduction to Rock Mechanics, Second Edition*. John Wiley and Sons.
- Haneberg, W. C., Mozley, P. S., Moore, J. C., & Goodwin, L. B. (1999). *Faults and subsurface fluid flow in the shallow crust*. Washington DC: American Geophysical Union Geophysical Monograph Series, 113.
- Hansen, A., & Schmittbuhl, J. (2003). Origin of the universal roughness exponent of brittle fracture surfaces: stress-weighted percolation in the damage zone. *Physical review letters*, *90*(4), 045504.
- Hirose, T., Mizoguchi, K., & Shimamoto, T. (2012). Wear processes in rock at slow to high slip rates. *J. of Structural Geology*, *38*, 102-116.
- Hoek, E. (2014). Retrieved from Rocscience: https://www.rocscience.com/hoek/corner/4_Shear_strength_of_discontinuities.pdf
- Hsu, S. M., & Shen, M. (2004). Wear prediction of ceramics. *Wear*, *256*, 867–878.
- Jaeger, J. C., Cook, N. G., & Zimmerman, R. W. (2007). *Fundamentals of rock mechanics*. Blackwell Publishing.
- Kanamori, H., & Brodsky, E.E. (2004). The physics of earthquakes. *Rep. Prog. Phys.*, *67*, 1429–1496.
- Lay, T., Kanamori, H., & Ruff, L. (1982). The asperity model and the nature of large subduction zone earthquakes. *Earthquake prediction research*, *1*, 3-71.
- Lee, A. G. G., & Rutter, E. H. (2004). Experimental rock-on-rock frictional wear: Application to subglacial abrasion. *J. of Geophys. Res.*, *109*, B09202, doi:10.1029/2004JB003059.
- Malamud, B. D., & Turcotte, D. L. (1999). Self-affine time series: I. Generation and analyses. *Adv. Geophys*, *40*, 1-90.
- Mandelbrot, B. B. (1983). *The Fractal Geometry of Nature*. New York: W. H. Freeman and Company.

- Micarelli, L., Benedicto, A., & Wibberley, C. A. J. (2006). Structural evolution and permeability of normal fault zones in highly porous carbonate rocks. *Journal of Structural Geology*, 28(7), 1214-1227.
- Otsuki, K. (1978). On the relationship between the width of shear zone and the displacement along fault. *Journal of the Geological Society of Japan*, Vol. 84, No. 11, 661-669.
- Patton F. D., & Deere D. U. (1970). Significant geologic factors in rock slope stability. *Planning Open Pit Mines Proc. Symp.Theor. Background Plann. Open Pit Mines with spec. Ref. to slope stability* (pp. 143-151). Johannesburg: Balkema, Cape Town.
- Patton, F. (1966). Multiple modes of shear failure in rock. *Proc. 1st Congr. Int. Soc. Rock Mech.* , (pp. 1, 509-513). Lisbon.
- Persson, B. N. (2006). Contact mechanics for randomly rough surfaces. *Surface Science Reports*, 61 (4), 201-227.
- Power, W. L., & Durham, W. B. (1997). Topography of natural and artificial fractures in granitic rocks: Implications for studies of rock friction and fluid migration. *Int. J. Rock Mech. Min. Sci.*, Vol. 34, No. 6, 979-989.
- Power, W. L., Tullis, T. E., & Weeks, J. D. (1988). Roughness and Wear During Brittle Faulting. *J. Geophys. Res*, 93, No. B12, 15268-15278.
- Queener, C. A., Smith, T. C., & Mitchell, W. L. (1965). Transient Wear of Machine Parts. *Wear*, Vol. 8, pp. 391-400.
- Rao, R. N. & Das, S. (2011). Effect of sliding distance on the wear and friction behavior of as cast and heat-treated Al–SiCp composites. *Materials and Design*, 32, 3051-3058.
- Reches Z., & Lockner, D. A. (2010). Fault weakening and earthquake instability by powder lubrication. *Nature*, Vol. 467, 452-456.
- Renard, F., Mair, K., & Gunderson, O. (2012). Surface roughness evolution on experimentally simulated faults. *J. of Structural Geology*, 45, 101-112.
- Renard, F., Viosin, C., Marsan, D., & Schmittbuhl, J. (2006). High resolution 3D laser scanner measurements of a strike-slip fault quantify its morphological anisotropy at all scales. *Geophys. Res. Let.*, 33, L04305 doi: 10.1029/2005GL025038.

- Robertson, E. G. (1983). Relationship of fault displacement to gouge and breccia thickness. *Miner. Engr.* 35, 1426-1432.
- Sagy, A., & Brodsky, E. (2009). Geometric and rheologic asperities in an exposed fault zone. *Journal of Geophysical Research*, Vol.114, B02301, doi:10.1029/2008JB005701.
- Sagy, A., Brodsky, E., & Axen, G. J. (2007). Evolution of fault-surface roughness with slip. *Geology*, Vol. 35, Num. 3, 283-286.
- Santner, E., Klaffke, D., Meine, K., Polaczyc, Ch., & Spaltmann, D. (2006). Effects of friction on topography and vice versa. *Wear*, 261, 101-106.
- Scholz, C. H. (1987). Wear and gouge formation in brittle faulting. *Geology*, Vol.15, 493-495.
- Scholz, C. H. (2002). *The Mechanics of Earthquakes and Faulting, 2nd Edition*. Cambridge, UK: Cambridge University Press.
- Scholz, C. H., & Engelder, J. T. (1976). The role of asperity indentation and ploughing in rock friction - I. *Int. J. Rock Mech. Min. Sci. & Geomech. Abstr.* Vol. 13, 149-154.
- Sibson, R. H. (1977). Fault rocks and fault mechanisms. *J. of Geol. Soc. London*, Vol. 133, 191-213.
- Simonsen, I., Hansen, A., & Nes, O. M. (1998). Determination of the Hurst exponent by use of wavelet transforms. *PHYSICAL REVIEW E*, Vol. 58, Num. 3, 2779-2787.
- Simonsen, I., Tarrats, A., & Vandembroucq, D. (2002). Characterization of rough self-affine surfaces by electromagnetic wave scattering. *Journal of Optics A: Pure and Applied Optics*, 4(5), S168-S174.
- Stein, S., & Wysession, M. (2003). *An Introduction to Seismology, Earthquakes, and Earth Structure*. Blackwell Publishing.
- Tatone, B. S., & Grasselli, G. (2013). An investigation of discontinuity roughness scale dependency using high-resolution surface measurements. *Rock mechanics and rock engineering*, 46(4), 657-681.
- Tests, I. S. (1978). Suggested methods for the quantitative description of discontinuities in rock masses. *Int. J. Rock Mech. Min. Sci. & Geomech. Abstr.*15, 319-368.

- Wang, W., & Scholz, C. H. (1994). Wear processes during frictional sliding of rock: A theoretical and experimental study. *Journal of Geophysical Research*, Vol.99, No. B4, pp. 6789-6799.
- Wesnousky, S. G. (1988). Seismological and structural evolution of strike-slip faults. *Nature*, v. 335, 340-342.
- Wibberley, C. A. J., Yielding, G., & Di Toro, G. (2008). Recent advances in the understanding of fault zone internal structure: a review. *Geological Society, London, Special Publications*, 299(1), 5-33.

9 Appendix I

This chapter includes figures of the pre and post-shear matrices that were used for the roughness analysis in section 4.2.

9.1 Experiment LN1 ($\sigma_n=5$ MPa)

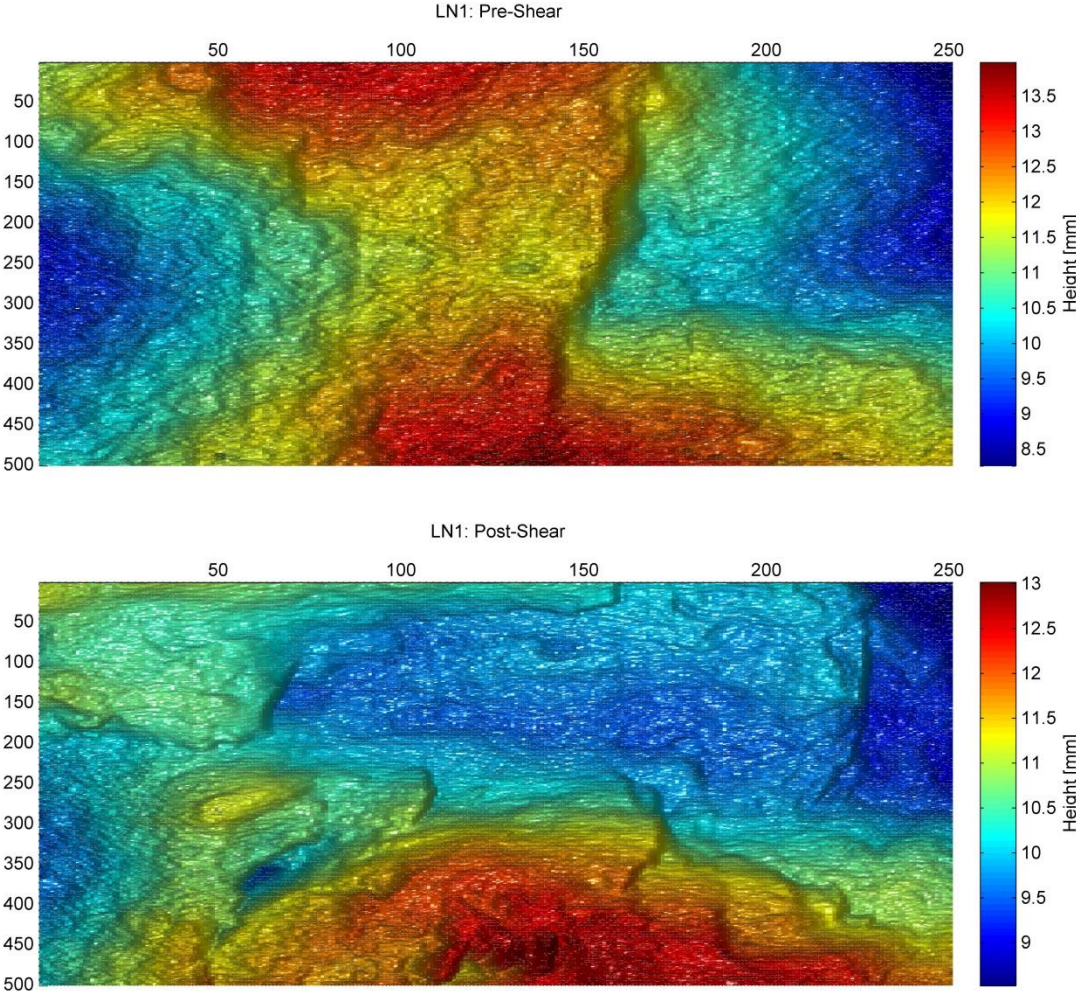


Figure 9.1. Pre (top) and post-shear (bottom) damage zone matrices for sample LN1. The matrices cover an area of 25×14.56 mm².

9.2 Experiment LN10 ($\sigma_n=7.5$ MPa)

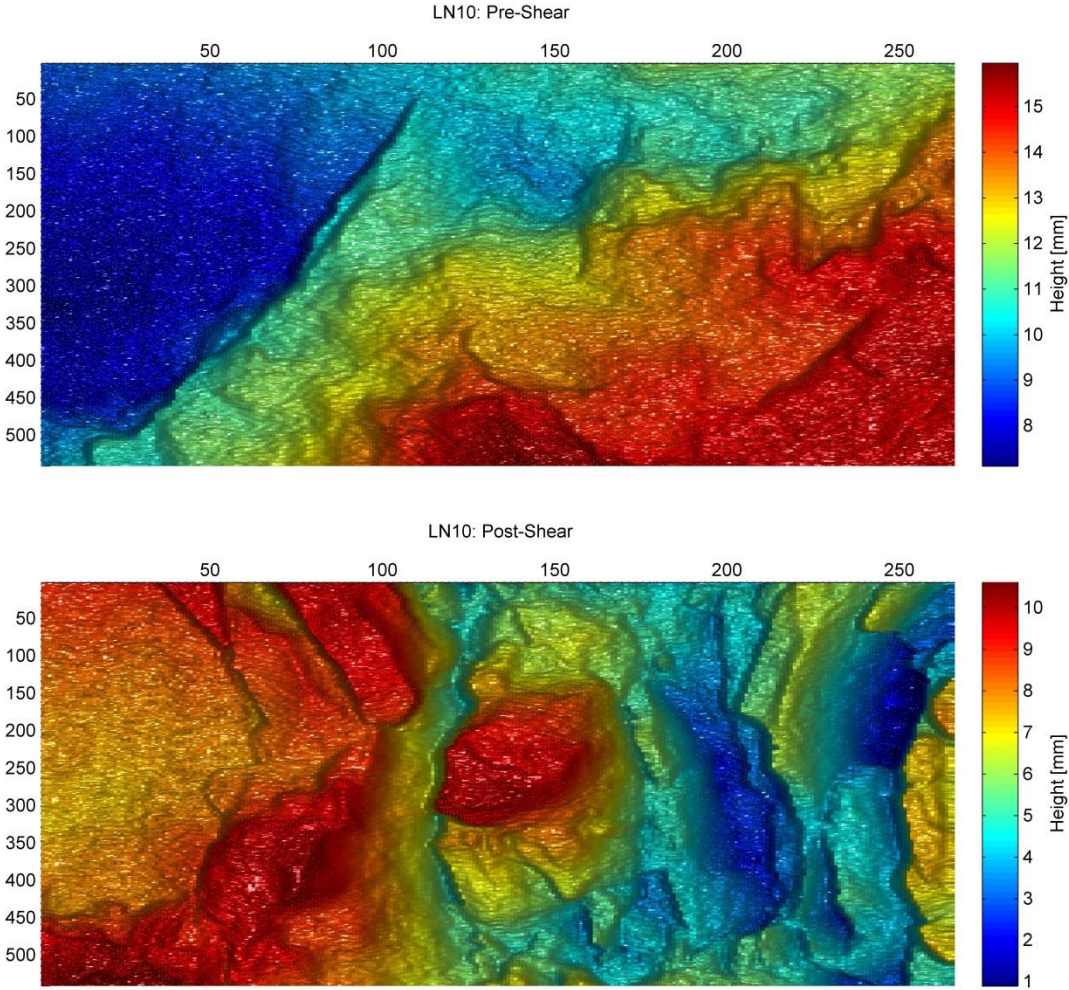


Figure 9.2. Pre (top) and post-shear (bottom) damage zone matrices for sample LN10. The matrices cover an area of 26.5×15.7 mm².

9.3 Experiment LN6 ($\sigma_n=10$ MPa)

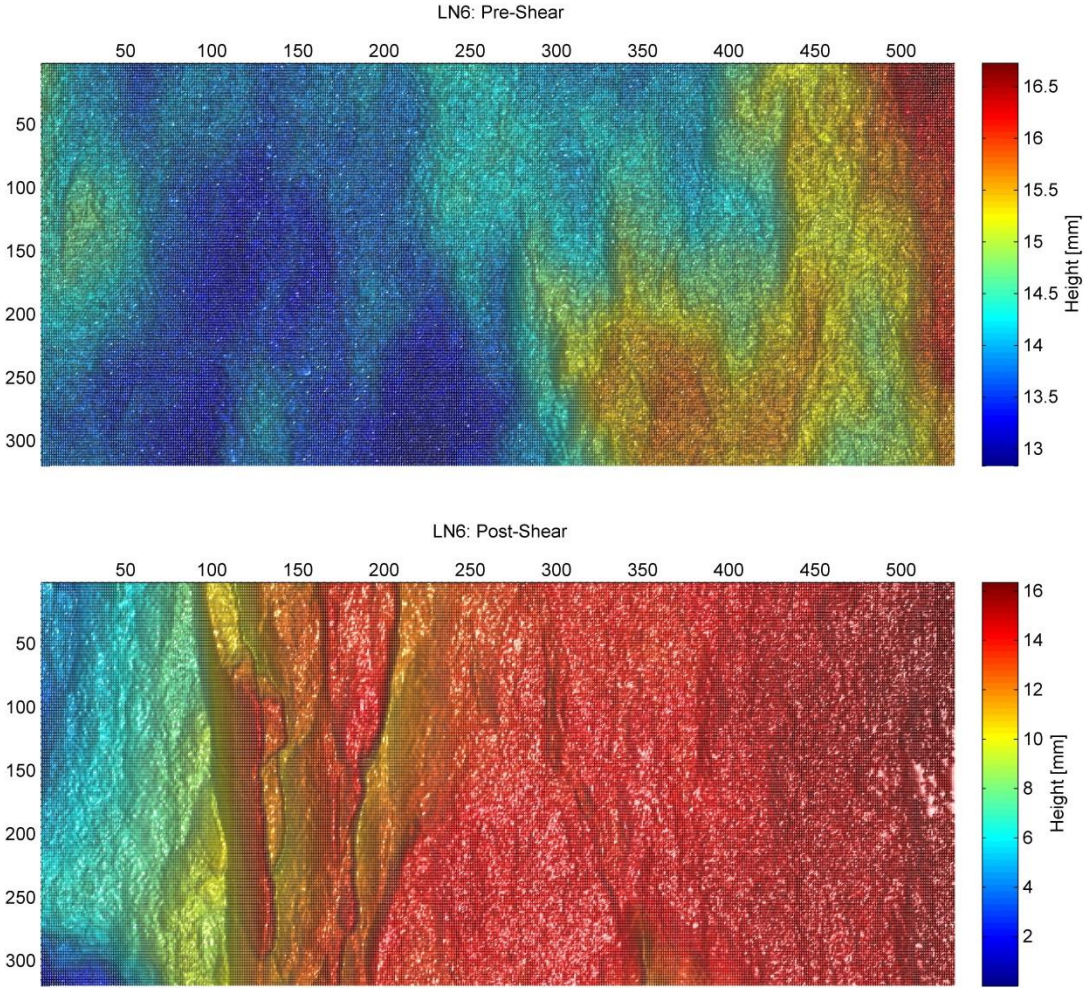


Figure 9.3. Pre (top) and post-shear (bottom) damage zone matrices for sample LN6. The matrices cover an area of 53x9.26 mm².

9.4 Experiment LN11 ($\sigma_n=12.5$ MPa)

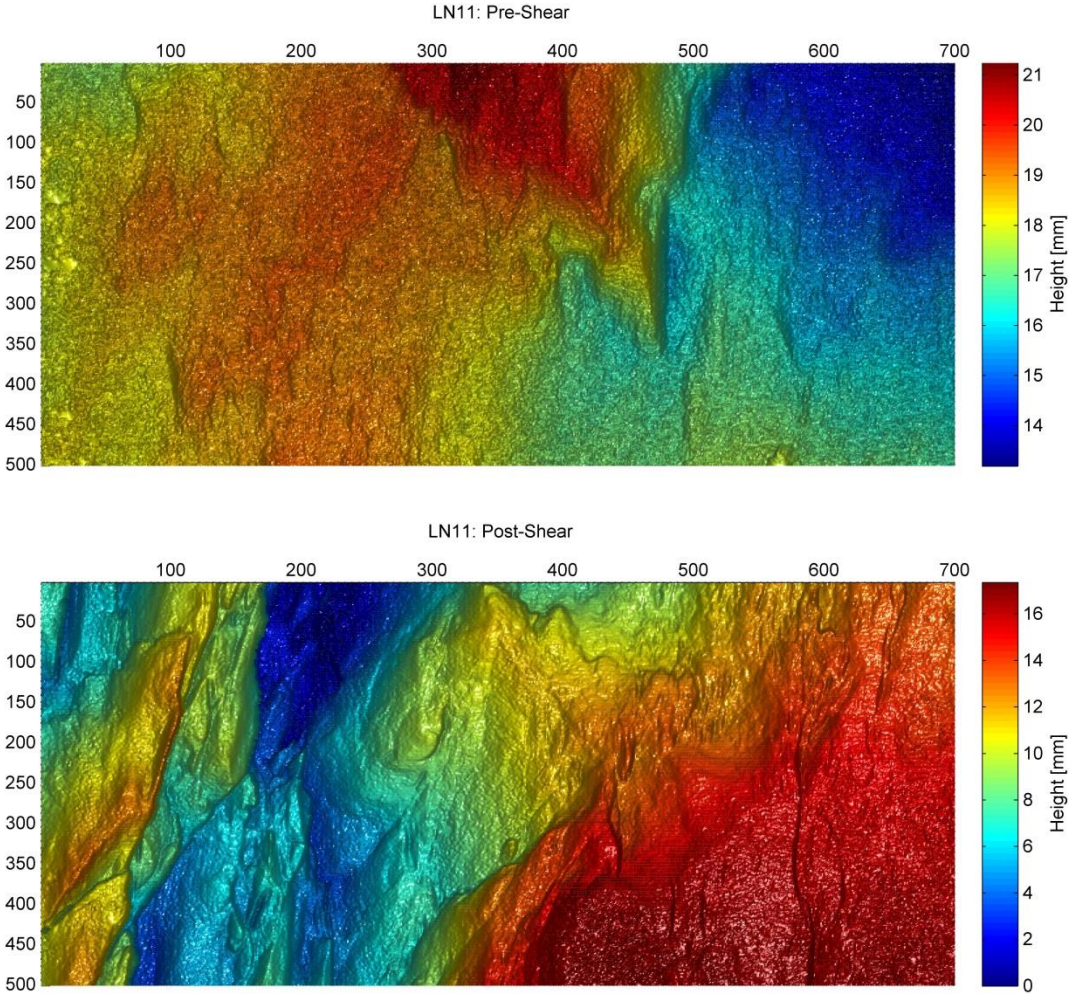


Figure 9.4. Pre (top) and post-shear (bottom) damage zone matrices for sample LN11. The matrices cover an area of 69.9×14.56 mm².

9.5 Experiment LN5 ($\sigma_n=15$ MPa)

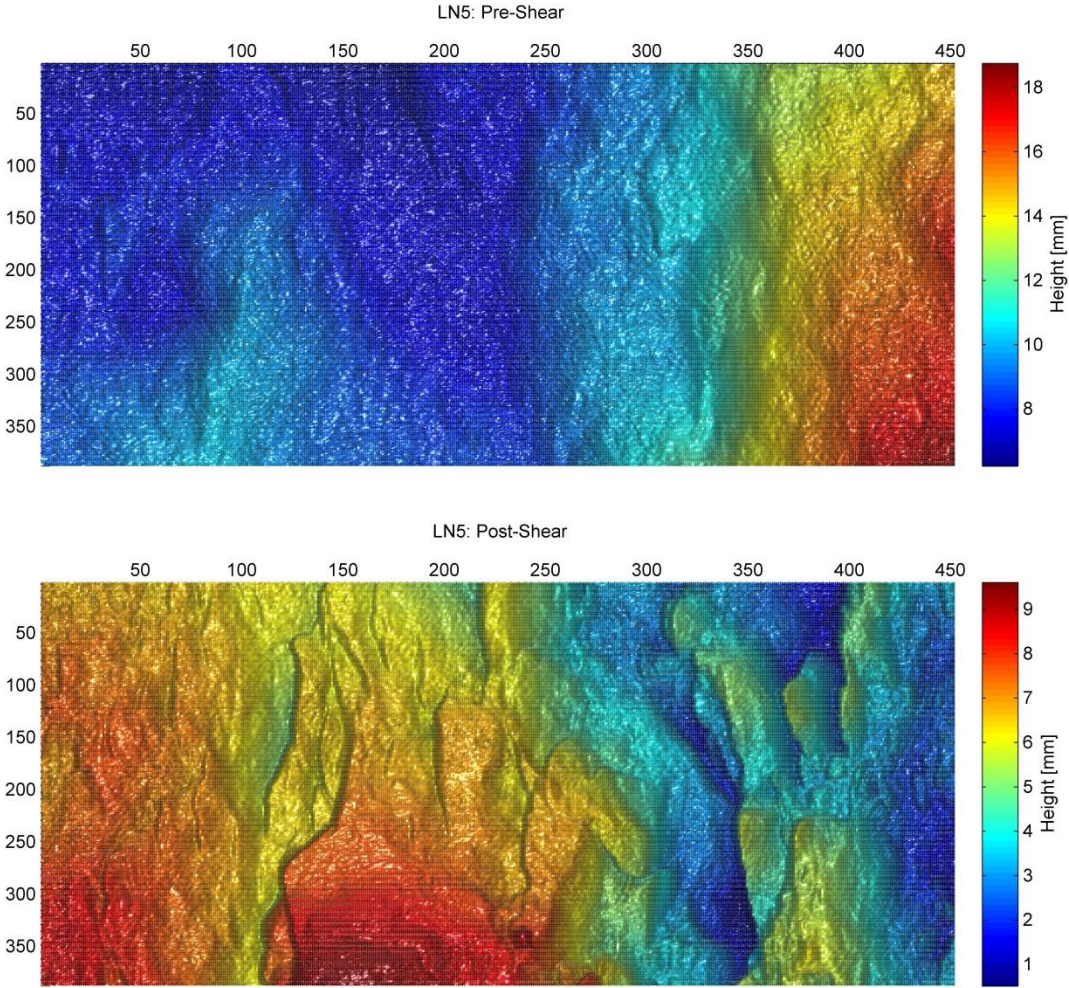


Figure 9.5. Pre (top) and post-shear (bottom) damage zone matrices for sample LN5. The matrices cover an area of 45.1×11.24 mm².

9.6 Experiment LN7 ($\sigma_n=15$ MPa)

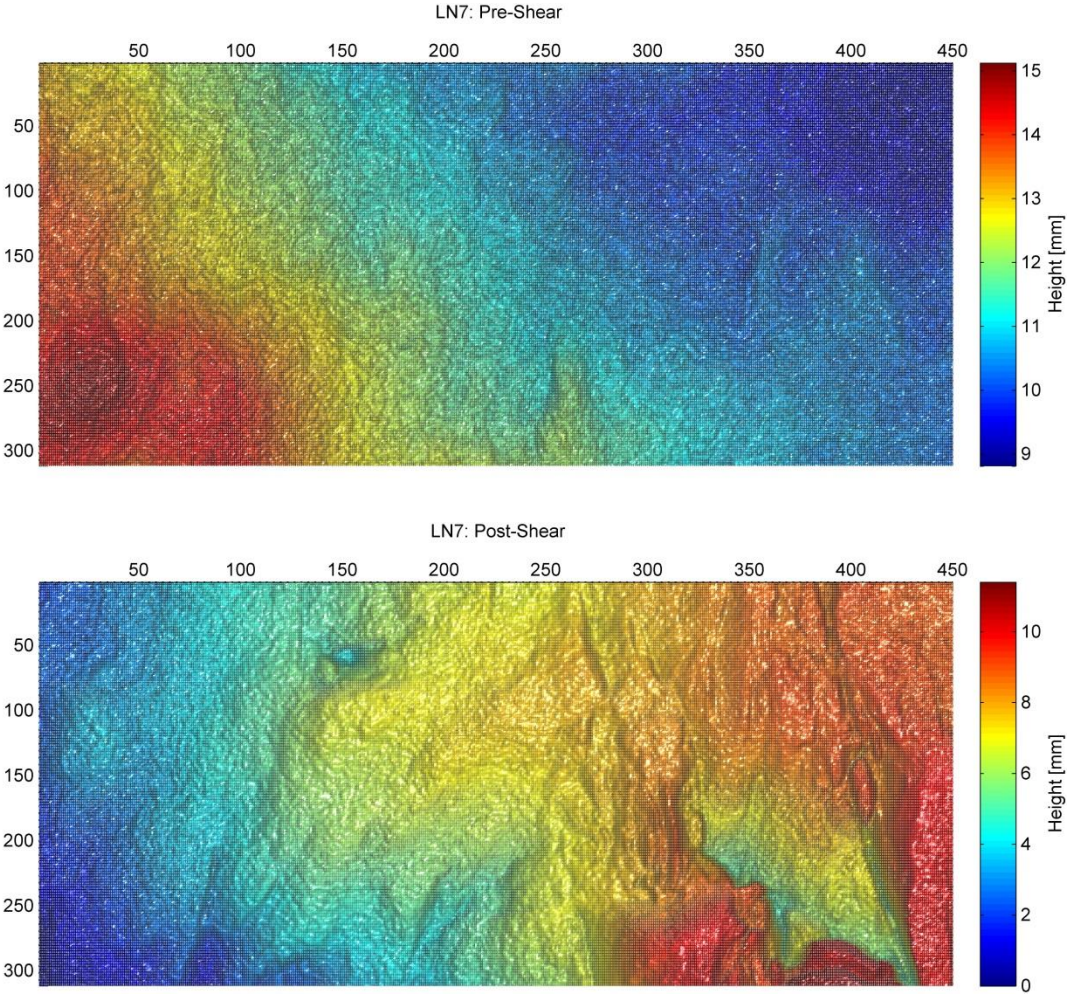


Figure 9.6. Pre (top) and post-shear (bottom) damage zone matrices for sample LN7. The matrices cover an area of 44.9×9.03 mm².

10 Appendix II

The plots in this appendix include additional plots from the analytical model in chapter 0.

10.1 Model Results for Run B ($\sigma_n=7.5$ MPa)

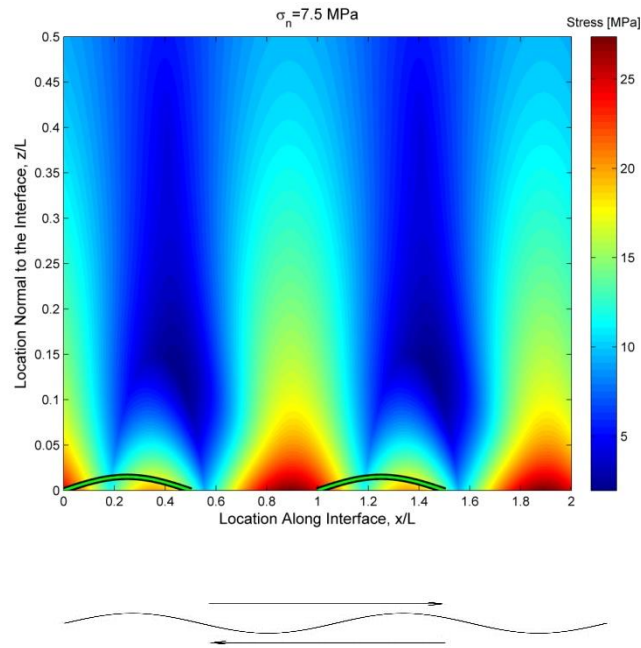


Figure 10.1. Maximum principal stress (σ_1) distribution throughout the upper half-space from run B, sheared under 7.5 MPa with a friction coefficient of 0.905.

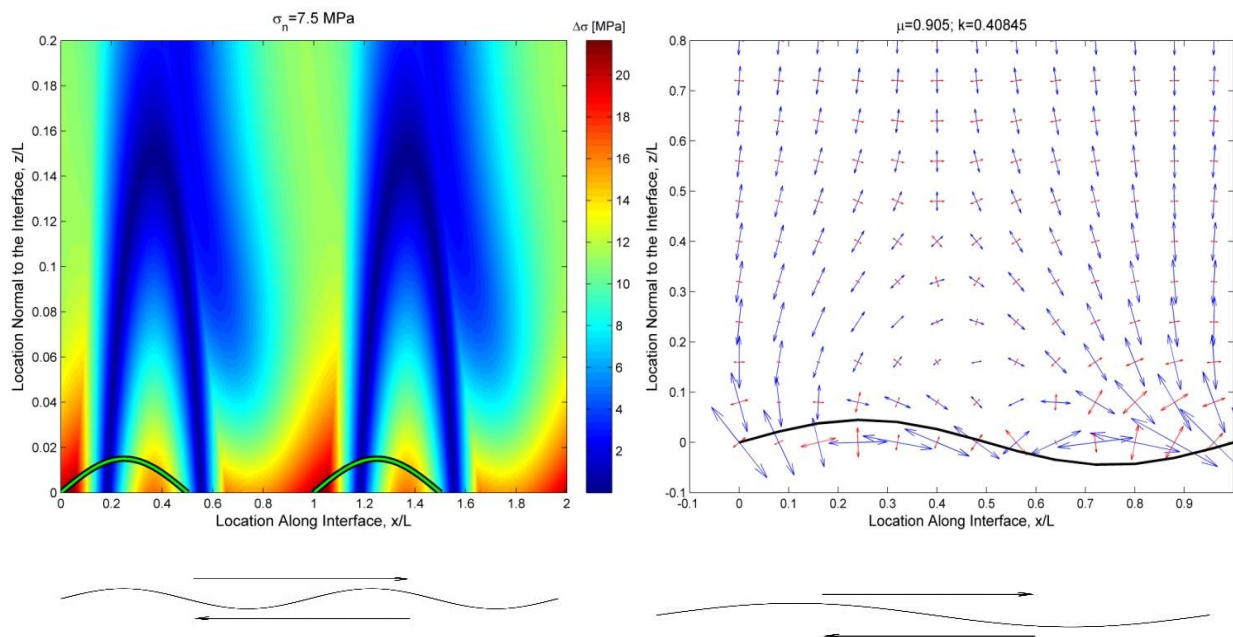


Figure 10.2. Stress distribution maps in the upper half-space for run B, sheared under 7.5 MPa with a friction coefficient of 0.905. Left panel – principal stress difference, the green wavy line in the bottom represents the interface geometry. Right panel – principal stress trajectories, the blue and red arrows represent the maximum and minimum stresses, respectively. The solid black wavy line in the bottom represents the interface.

10.2 Model Results for Run C ($\sigma_n=10$ MPa)

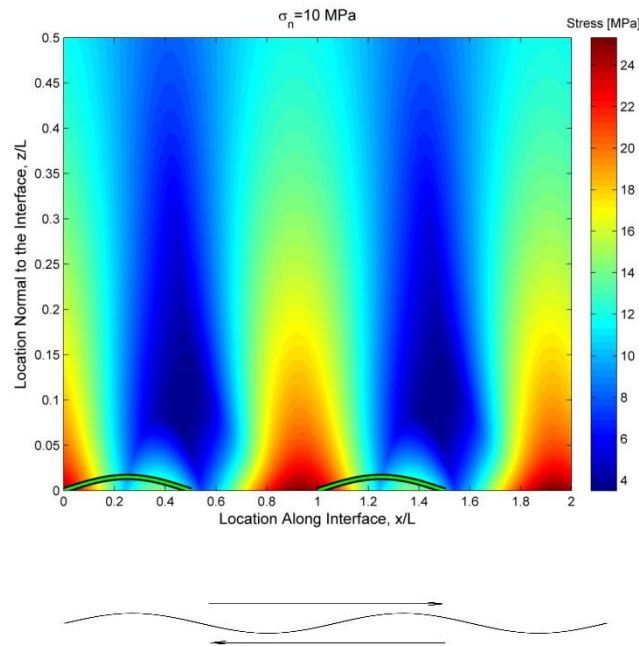


Figure 10.3. Maximum principal stress (σ_1) distribution throughout the upper half-space from run C, sheared under 10 MPa with a friction coefficient of 0.661.

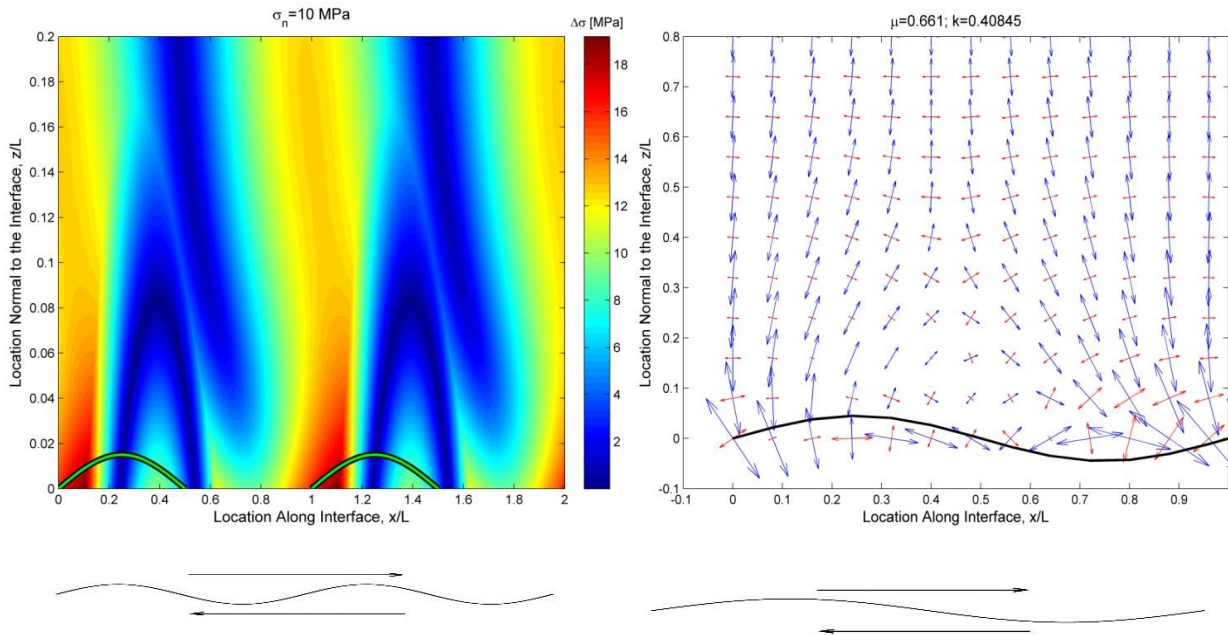


Figure 10.4. Stress distribution maps in the upper half-space for run C, sheared under 10 MPa with a friction coefficient of 0.661. Left panel – principal stress difference, the green wavy line in the bottom represents the interface geometry. Right panel – principal stress trajectories, the blue and red arrows represent the maximum and minimum stresses, respectively. The solid black wavy line in the bottom represents the interface.

10.3 Model Results for Run E ($\sigma_n=15$ MPa)

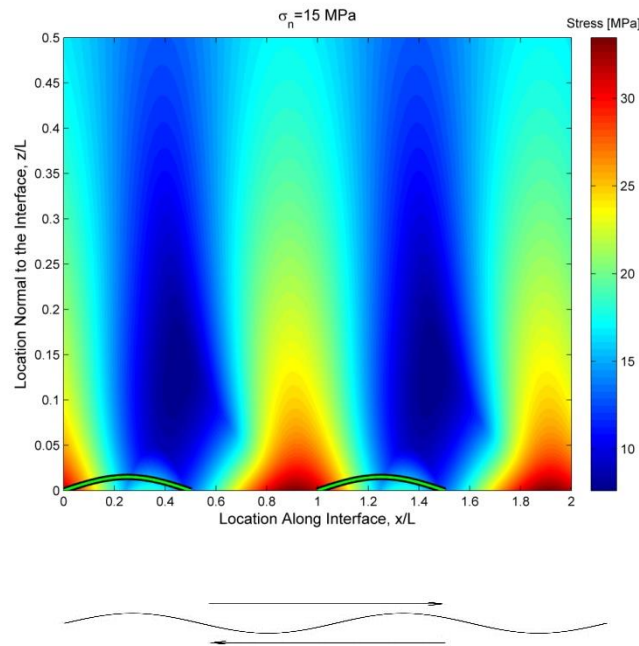


Figure 10.5. Maximum principal stress (σ_1) distribution throughout the upper half-space from run E, sheared under 15 MPa with a friction coefficient of 0.862.

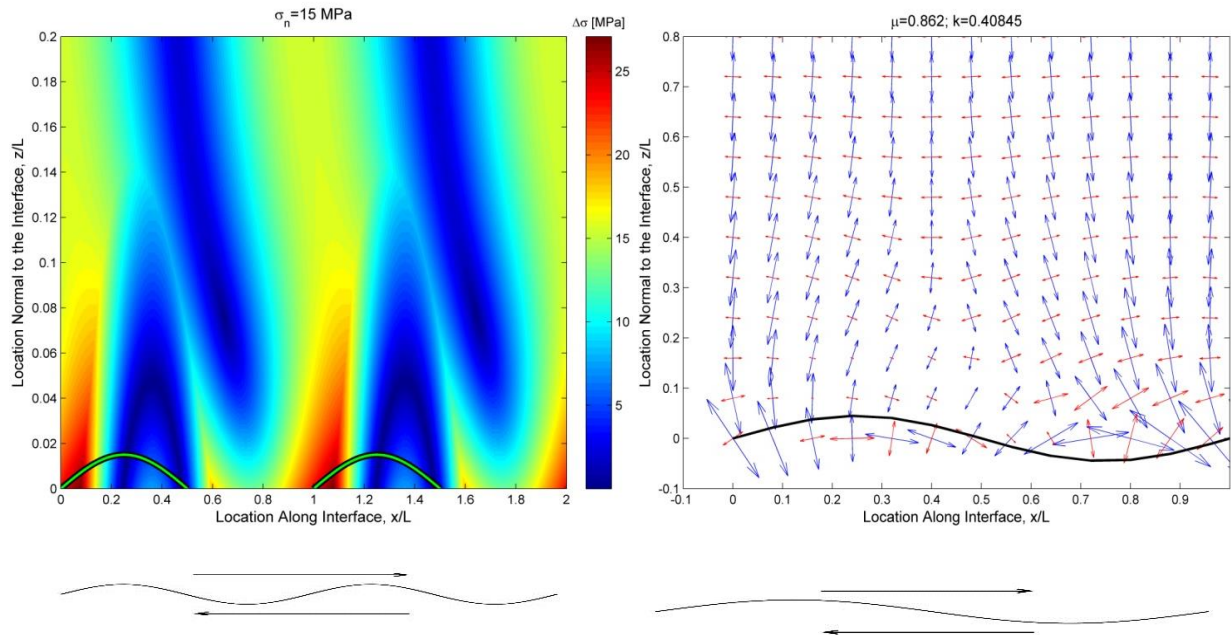


Figure 10.6. Stress distribution maps in the upper half-space for run E, sheared under 15 MPa with a friction coefficient of 0.862. Left panel – principal stress difference, the green wavy line in the bottom represents the interface geometry. Right panel – principal stress trajectories, the blue and red arrows represent the maximum and minimum stresses, respectively. The solid black wavy line in the bottom represents the interface.

10.4 Model Results for Run F ($\sigma_n=15$ MPa)

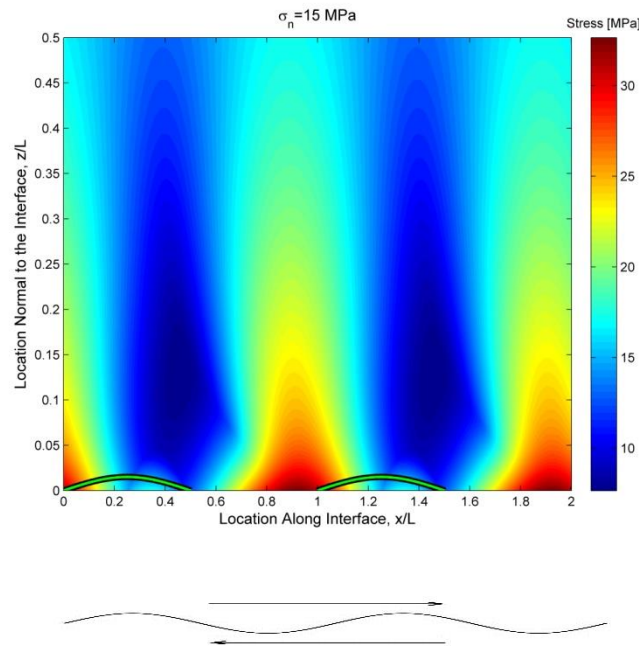


Figure 10.7. Maximum principal stress (σ_1) distribution throughout the upper half-space from run E, sheared under 15 MPa with a friction coefficient of 0.821.

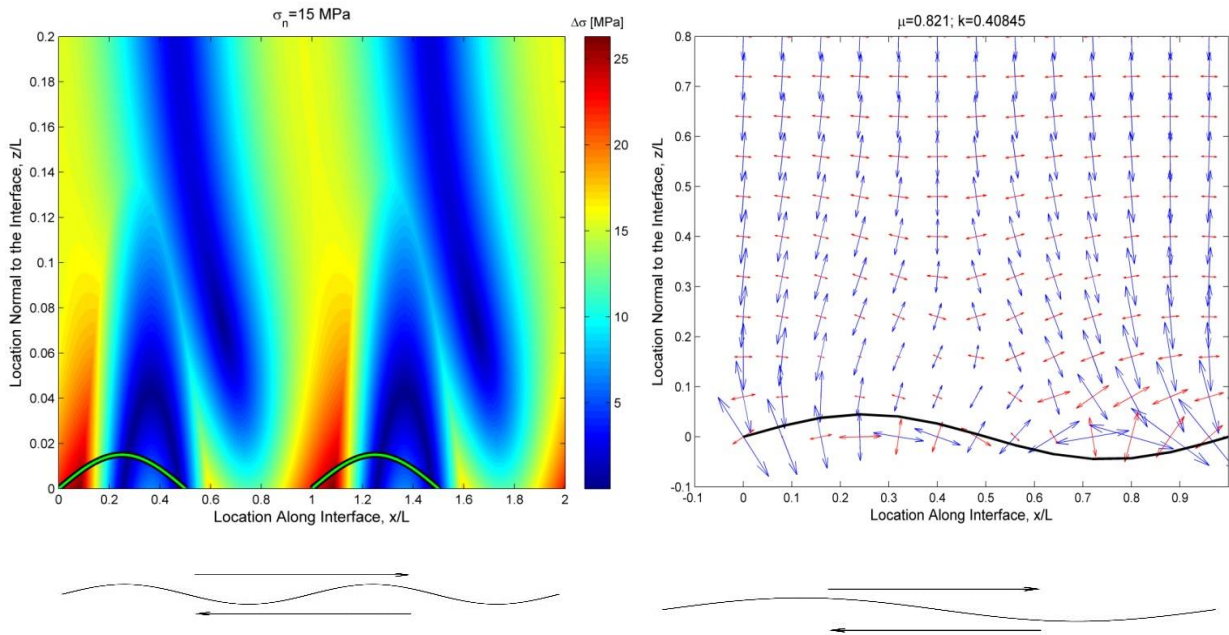


Figure 10.8. Stress distribution maps in the upper half-space for run E, sheared under 15 MPa with a friction coefficient of 0.821. Left panel – principal stress difference, the green wavy line in the bottom represents the interface geometry. Right panel – principal stress trajectories, the blue and red arrows represent the maximum and minimum stresses, respectively. The solid black wavy line in the bottom represents the interface.

10.5 Reference Model

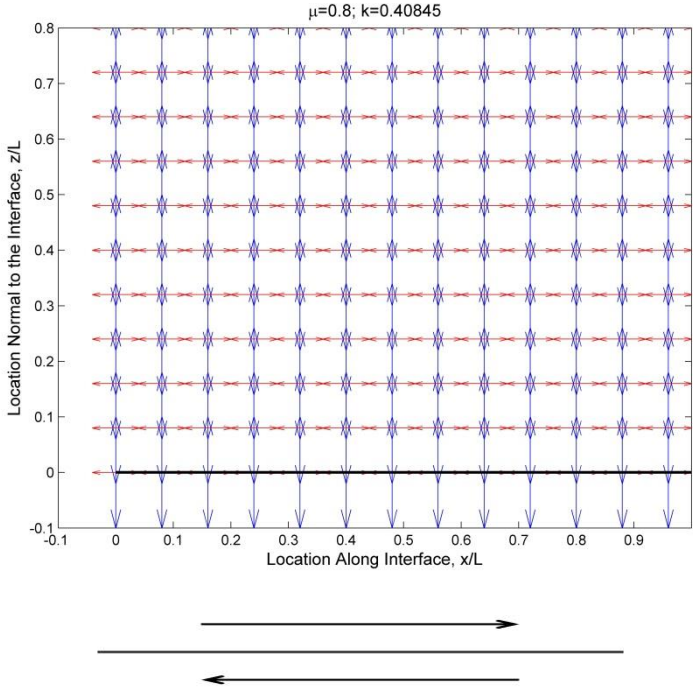


Figure 10.9. Modeled stress trajectory distribution in the upper-half space for a perfectly smooth interface. Maximum and minimum principal stress trajectories are represented by blue and red arrows, respectively. The interface is represented as a solid black line. Note that the stresses (magnitude and direction) is uniform throughout the medium.

הניתוח הגיאומטרי של משטחי הניסויים הראה כי הם אינם בעלי מבנה פרקטלי self-affine. חוסר הפרקטליות יוחס לגודל הגרגרים שבונים את משטחי הגיר. הניתוח מראה כי עקומות ה-PSD כנגד אורך גל סוטות ממבנה של גיאומטריה פרקטלית סביב אורכי גל התואמים לקוטר הגרגר הממוצע. לעומת זאת, משטחי ההעתקה לאחר הגזירה הראו מבנה פרקטלי self-affine עם ערך של אקספוננט Hurst של ~ 0.8 בכיוון הגזירה. שינוי הגיאומטריה יוחס לאבולוציית החספוס שעברו משטחי הניסויים במהלך הגזירה. הנזק שנגרם לסלע המארח במהלך הגזירה השפיע על החספוס בסדרי גודל שונים, כולל בסקלת הגרגרים עצמם. לכן, על ידי שבירת הגבשושיות, גיאומטריית המשטחים השתנתה לפרקטלית במהלך הגזירה.

בדומה להעתקים טבעיים, בכל הניסויים שנחקרו כאן התפתחו אזורי נזק. בנוסף על כך, הן במשטחי הניסויים והן בהעתקים טבעיים, יחס אמפליטודת החספוס לאורך הגל (הטופוגרפיה) הינו גדול או שווה לסדר הגודל של כמות ההחלקה עבור אירוע החלקה בודד. לכן, חקר ההשפעות של מאמץ נורמלי וחספוס במשטחי ניסויים, הינו בר תוקף ובעל חשיבות בסיסית עבור ההבנה של האבולוציה המכנית של העתקים טבעיים. השלכות מחקר זה מצביעות על כך שחספוס הינו בעל חשיבות לא רק במונחי התנגדות לגזירה, אלא גם בפיזור המאמצים על פני משטחי העתקה והתפתחות אזורי הנזק שסביבם.

תקציר

הטופוגרפיה של משטחי העתקה משפיעה בצורה משמעותית על הדינמיקה של רעידות אדמה. פרופיל החספוס של משטחי החלקה קשור בפיזור המאמצים על פני מישורי העתקים, התנגדות ההעתקים לגזירה ומרחק החלקה קריטי.

אבולוציית החספוס של משטחי העתקה נחקרה בעבודה זו באמצעות ניסויי גזירה ישירה במעבדה. משטחים תואמים, שהוכנו על ידי סדקי מתיחה, לפי שיטת כפיפת קורה בארבע נקודות, נגזרו תחת מאמץ נורמלי של 5 עד 15 MPa. בכל ניסוי המאמץ הנורמלי נשאר קבוע, המשטחים נגזרו למרחק של 10 mm, בקצב של 0.05 mm/s. יישום הניסויים נעשה באמצעות מערכת סרוו (servo) הידראולית במעגל סגור. תוצאות הניסויים הראו כי מאמץ הגזירה גדל לאורך מהלך הניסוי, עד אשר המשטחים המחוספסים מגיעים לשיא התנגדות לגזירה. נוסף על כך, בשלבי הגזירה הראשונים קיימת תופעה של תפיחת (dilation) הממשק המחליק, בעוד שבשלבי הגזירה המאוחרים קיימת תופעה של התכווצות (contraction). דפוס התפיחה-התכווצות של הממשקים המחוספסים מצביע על שני מנגנוני אינטראקציה בין גבשושיות, אשר היו דומיננטיים במהלך הגזירה: טיפוס ונעילה. מכניזם הנעילה יוחס לשיא החיכוך, אשר חושב במהלך הניסויים, וכתוצאה מכך לכשל הגבשושיות. שיא החיכוך המחושב בכל ניסוי הראה כי ערך זה לא תאם למאמץ הנורמלי המכסימלי שהופעל. למעשה, ערכי חיכוך השיא והשיורי לא תאמו למאמץ הנורמלי שהופעל בכל ניסוי. נטען כאן כי ההבדל בערכי חיכוך השיא והשיורי שהתקבלו כנגד מאמץ נורמלי נובע מחספוס המשטחים ההתחלתי.

חספוס המשטחים נמדד באמצעות סורק אופטי. כל משטח נסרק לפני ואחרי ניסוי הגזירה. השתנות החספוס נותחה על ידי שיטות $\text{power spectral density (PSD)}$ ו- $\text{root mean square (RMS)}$. תוצאות הניתוח הראו כי עבור מאמץ נורמלי גדול מ-5 MPa, חספוס המשטחים גדל במהלך הגזירה. תוצאות אלו הן בניגוד לתוצאות של Davidesko et al. (2014), אשר ערכו ניסויי גזירה עם אותו סוג של משטחים, אך תחת מאמץ נורמלי של 2 MPa בלבד. הבדל התוצאות בין המחקר הנוכחי למחקר Davidesko et al. (2014), מיוחס לערכי המאמץ הנורמלי הגבוהים שנבדקו במחקר זה. רוב השינוי שנגרם במשטחי העתקה התרכז באזורי נזק (damage zones). מבחינת השינוי ותוצרי השחק הוסק כי הגידול בחספוס נגרם כתוצאה מנזק חודרני לסלע המארח, שכלל שבירה ועקירת גבשושיות.

השתנות החספוס קורלטיבית כאן לירידת המאמץ (stress drop) שנמדדת במהלך הגזירה, כיוון ששניהם מייצגים את שחרור האנרגיה האלסטית המתרחש במעבר ממאמץ גזירה מכסימלי למאמץ גזירה שיווי. ממדי הנזק שנגרם למשטחים גדולים מממדי החספוס עצמו, כך שהגבשושיות שמהוות את החספוס הראשוני נשברות חלקית או במלואן. במחקרים קודמים הוצע כי החספוס משתנה כתוצאה מגדיעה של הגבשושיות. לעומת זאת, מחקר זה מצביע על כך שאנרגיית העיבורים המצטברת בתחילת החלקה מתועלת לשבירת הגבשושיות. תהליך זה מביא ליצירת משטחים חדשים באוריינטציות שונות ממישור החלקה הממוצע. במקביל נעשה ניתוח על ידי מודל אנליטי, לצורך אימות הנזק שנצפה במהלך הניסויים. תוצאות המודל הראו כי חספוס ממשק החלקה משפיע על שדה המאמצים הקיים בקרבת הממשק עצמו. ההשפעה בוטאה ביצירת ריכוזי מאמצים, הגברת הפרש המאמצים הראשיים ושינוי כיווני המאמצים בקרבת הממשק ביחס לכיוונם רחוק מהממשק. יחד עם זאת, נטען כי ההתנגדות לגזירה תלויה משמעותית בשדה המאמצים בקרבת הממשק המחליק. קשר זה בא לידי ביטוי בקורלציה שבין ערך ההתנגדות לגזירה לבין כמות השחק המצטבר.

אוניברסיטת בן-גוריון בנגב
הפקולטה למדעי הטבע
המחלקה למדעי הגיאולוגיה והסביבה

**השפעת מאמץ נורמלי על אבולוציית החספוס של מישורי העתקה ניסויים באמצעות
גזירה**

חיבור זה מהווה חלק מהדרישות לקבלת התואר "מוסמך למדעי הטבע" (M.Sc.)

ניר בדט

בהנחיית פרופ' יוסף חודרה חצור ודר' אמיר שגיא

חתימת הסטודנט: _____ תאריך: _____

חתימת המנחה: _____ תאריך: _____

חתימת המנחה: _____ תאריך: _____

חתימת יו"ר הועדה המחלקתית: _____ תאריך: _____

פברואר 2015

אוניברסיטת בן-גוריון בנגב
הפקולטה למדעי הטבע
המחלקה למדעי הגיאולוגיה והסביבה

**השפעת מאמץ נורמלי על אבולוציית החספוס של מישורי העתקה ניסויים באמצעות
גזירה**

חיבור זה מהווה חלק מהדרישות לקבלת התואר "מוסמך למדעי הטבע" (M.Sc.)

ניר בדט

בהנחיית פרופ' יוסף חודרה חצור ודר' אמיר שגיא

פברואר 2015